Numerical and Experimental Investigation of Tidal Current Energy Extraction

Xiaojing Sun

A thesis submitted for the degree of Doctor of Philosophy
The University of Edinburgh
2008

Declaration of Originality

I hereby declare that this thesis was composed entirely by myself. The work contained in this thesis is my own except where otherwise indicated in the text, and this work has not been submitted for any other degree or professional qualification except as specified.

Xiaojing Sun

To my parent and husband Fu Gang

Acknowledgements

I wish to express my gratitude to the Engineering and Physical Science Research Council (EPSRC) for their support of the SuperGen (marine) consortium, which financed much of this work.

I am extremely grateful to my main supervisor Professor Ian G. Bryden for his invaluable guidance, constructive advice, constant support and endless encouragement throughout my study.

Dr. David Forehand has been an excellent second supervisor during these years. He is always eager to help when I encountered difficulties. Thank you very much for your generous help and fruitful discussions. Your friendship is precious.

Mr. Henry Jeffrey is greatly appreciated for his assistance during all the experimental testing in this research work. Dr. Alan Owen is also acknowledged for generously providing the design of the pitot probe which was adopted for the water measurements.

I would like to thank Dr. Shuisheng He for all the great advice and help during the initial stages of the project.

I also thank Mr. Graeme Budge for his work to construct the experimental test rig for this research and his support at the lab.

Many thanks to Dr. Tom Bruce for proof-reading my thesis draft, his thoughtful commentary and encouragement.

Thanks to all my research colleagues at the Robert Gordon University and the University of Edinburgh for the open, cooperative and friendly atmosphere and their support.

Last but not least, I would like to express my gratitude to my family in China for their life-long love and support.

Abstract

Numerical and experimental investigations of tidal current energy extraction have been conducted in this study.

A laboratory-scale water flume was simulated using commercial computational fluid dynamics (CFD) code FLUENT™. In the numerical model, the tidal current turbine is represented with an actuator disk, which produces a pressure drop associated with energy loss. The free water surface is considered in the model using a volume of fluid method and is allowed to deform freely. Numerical results identified that a localised wake is formed behind the tidal current turbine and there is considerable localised flow acceleration around and most especially, under the energy extraction device. A free water surface drop is visualised in the model results due to the energy extraction and this free surface drop is believed to have an impact on the recovery of turbine wake. The influence of other parameters like water depth, ambient turbulence and flow speed on the tidal current energy extraction are also testified, based on the numerical model. Numerical results demonstrated that, because of the existence of a free water surface, tidal turbine interaction with the flow is a complicated three dimensional problem. Therefore, completely using the theoretical methods of wind turbines for tidal current turbine study would be inappropriate.

Two physical tests were deigned for the experimental investigation of energy extraction from tidal currents and were carried out under different testing conditions: one was in moving water using a natural open channel and the other was in still water using a towing tank. Comparing experimental and numerical results of wake velocity profiles, good qualitative agreement has been obtained, which proves that the proposed numerical model can provide essential insight into the mechanism of wake development behind tidal current turbines. Experimental results also confirmed that, although moving water is the real operational condition of tidal turbines, a towing tank is still an ideal facility for the experimental study of tidal turbines, especially at the early stages of understanding of the detailed physical processes governing the performance of rotors and turbine wake behaviour.

This study is a comprehensive investigation into tidal current energy extraction at laboratory scale. Environmental impact of tidal current energy extraction is further recognized and an appropriate experimental facility for the model testing of tidal energy extraction devices is recommended.

Contents

List of Figures

List of Tables

List of Notation

A	Swept area of a tidal current energy conversion device (m^2)
A_1	Upstream area of the streamtube in the actuator disk theory (m^2)
A_2	Downstream area of the streamtube in the actuator disk theory (m^2)
A_d	Area of actuator disk (m^2)
a	Interference factor
B	Channel width (m)
C_D	Drag force coefficient
C_p	Power coefficient
C_μ	Empirical constant in turbulence models
D	Drag force (N)
D_h	Hydraulic diameter of the open channel (m)
d	Characteristic length of the actuator disk or diameter of the perforated disk (m)
F_r	Froude number
g	Gravitational acceleration ($m\ s^{-2}$)
h	Submerged depth from the centre of the perforated disk to the free water surface (m)
h_c	Critical depth (m)
I	Turbulence intensity
K_0	Constant derived from the mean spring peak
K_1	Constant derived from the ratio between the mean spring peak and the mean neap peak currents
k	Turbulent kinetic energy ($m^2\ s^{-2}$)
L	Characteristic length of mean flow (m)
l	Turbulence length scale (m)
M	Mesh size of turbulence-generating grid (m)
$\dot{m}$	Mass flow rate ($kg\ s^{-1}$)
P_{total}	Total power in the flow ($kg\ m^2\ s^{-3}$)
$P_{extract}$	Power extracted ($kg\ m^2\ s^{-3}$)
p	Pressure (Pa)
p'	Turbulent fluctuations in pressure (Pa)
$\overline{p}$	Time-averaged pressure (Pa)
Q	Volume flow rate ($m^3\ s^{-1}$)
R_e	Reynolds number
t	Times (s)
T_0	Period of the semidiurnal variation (s)
T_1	Period of the spring-neap cycle (s)

U	Local velocity component of tidal current perpendicular to the swept area of tidal current energy conversion device (m s^{-1})
U_w	Wake velocity (m s^{-1})
U_c	Velocity on wake centreline (m s^{-1})
U_∞	Freestream velocity (m s^{-1})
U_d	Velocity at the actuator disk (m s^{-1})
U_2	Far wake velocity in the actuator disk theory (m s^{-1})
u	Instantaneous velocity component in x direction (m s^{-1})
u'	Turbulence fluctuations in velocity component in x direction (m s^{-1})
$\overline{u}$	Time-averaged velocity component in x direction (m s^{-1})
Δu_∞	Velocity defect in the wake at the downstream end of the streamtube (m s^{-1})
Δu_d	Velocity decreased at the actuator disk (m s^{-1})
v	Instantaneous velocity component in y direction (m s^{-1})
v'	Turbulent fluctuations in velocity component in y direction (m s^{-1})
$\overline{v}$	Time-averaged velocity component in y direction (m s^{-1})
w	Instantaneous velocity component in z direction (m s^{-1})
w'	Turbulent fluctuations in velocity component in z direction (m s^{-1})
$\overline{w}$	Time-averaged velocity component in z direction (m s^{-1})
x	Longitudinal coordinate direction (m)
X	Body force component in the x direction (N m^{-3})
y	Lateral coordinate direction (m)
Y	Body force component in the y direction (N m^{-3})
z	Vertical coordinate direction (m)
Z	Body force component in the z direction (N m^{-3})
α	Volume fraction in the VOF model
ε	Dissipation rate of k (m^2 s^{-3})
μ	Dynamic viscosity (kg m^{-1} s^{-1})
μ_t	Dynamic eddy viscosity (kg m^{-1} s^{-1})
ν	Kinematic viscosity (m^2 s^{-1})
ρ	Density (kg m^{-3})
σ_k	Empirical constant in turbulence model
σ_ε	Empirical constant in turbulence model

Chapter 1

INTRODUCTION

Overview

This thesis is intended to add to the increasing understanding and knowledge on the subject of capturing energy from marine resources. The work conducted focuses on the laboratory-scale investigation of tidal current energy extraction using numerical and experimental methods. The motivation for this study is examined in section 1.1 of this chapter. Some background knowledge about tidal energy is introduced in section 1.2 and is divided into separate parts, including the historic utilisation of tidal energy, tidal energy resource, tidal current energy converters and contemporary developments in tidal current energy. Current research on utilization of tidal currents is viewed in section 1.3. The objectives of the study are listed in section 1.4 and the structure of this thesis is presented in section 1.5 at the end of this chapter.

1.1 Motivation for the study

'Climate change' is becoming one of the most common phases appearing in our life. It is not only because we are experiencing warmer and wetter weather than

decades ago, but also because of natural disasters brought to human beings due to the more frequent extreme weather events: European heatwave, America hurricanes and UK's storms. However, humanity is to blame [1]. In the 150 years since the industry revolution, concentrations of carbon dioxide in the atmosphere have risen as much as in the previous 20 000 years [2] and are higher than at any time in the past 500 000 years. Concentrations of atmospheric methane, which is a more potent 'green house gas', have more than doubled since the 1700s. Most of these recent increases help to drive 'global warming' and have resulted from the burning of fossil fuel by human activity [3]. Harsh facts alarm us to take vital actions to prevent further damage to the environment. The Kyoto Protocol, an international agreement on fighting climate change, was signed by 38 individual countries in 1997 with the aim to reduce the amount of carbon dioxide (CO_2) being released. The EU response was to cut by 8% CO_2 emission below 1990 levels by 2010 [4] and a scheme was proposed to achieve this target that included reducing the energy consumption, improving energy efficiency and utilising renewable energy. The UK government committed to 20% reductions in emission of CO_2 with respect to 1990 levels by 2010, with the hope that up to 10% electricity would be supplied from renewable energy [5]. Renewable energy is now widely acknowledged as a sustainable substitute for fossil fuels to meet the growth in demand for energy, thus playing a significant role in reducing greenhouse gas emissions.

Renewable energy covers those energy flows that occur naturally and repeatedly in the environment and can be harnessed for human benefits [6], for example wind and water. Wind energy takes up a big part of the current renewable energy market, simply because it is a relative mature industry with long term technology

development. However, since wind or water comes from natural resources, the diversity of renewables is important for the security of energy supply.

71 percent of the Earth's surface is covered with water. The marine resource has an enormous energy potential. Wave and tidal energy are believed to be able to provide significant fractions of the overall energy supply in the UK, if fully exploited [7]. Tidal energy has advantages in being predictable and reliable. However, compared to other renewables, tidal energy is still in its infancy [8]. Development of scientific understanding for tidal energy utilization is urgently required. Technology needs to be ready before tidal energy is to be commercially viable in the near future.

The motivation for this study is this need to increase the knowledge of tidal energy, focusing on the aspect of tidal current extraction. The processes associated with tidal energy extraction are simulated while considering the entire operating environment of tidal current energy converters. An essential insight into the interaction of a tidal current energy converter with its environment can be gained. Additionally, obtaining experimental data through simulated tidal turbine testing can provide the experimental basis for proper laboratory facility selection for tidal current energy converters.

1.2 Background to the study

1.2.1 Tidal Energy Formation and Historic Applications

Tides are the cyclic raising and falling of Earth’s ocean surface and are caused by the rotation of the earth within the gravitational fields of the moon and sun. Tides

change periodically and there are three basic types of tidal patterns, according to a number of interacting cycles- [7].

- A half-day (semi-diurnal) cycle: the rotation of the earth within the gravitational field of the moon, which results in a period of 12 hours 25 minutes between successive high waters.
- Daily (diurnal) tides: Only one high tide and one low tide in a 24-hour period. This is tide occurring in some regions such as the Gulf of Mexico.
- A 14-day cycle: caused by the superposition of the gravitational fields of the moon and sun. The sun's gravitational field reinforces that of the moon at new moon and full moon and results in maximum tides or spring tides. At quarter phases of the moon, there is partial cancellation, resulting in minimum or neap tides. The range of a spring tide is typically about twice that of a neap tide. This is demonstrated in Figure 1.1.

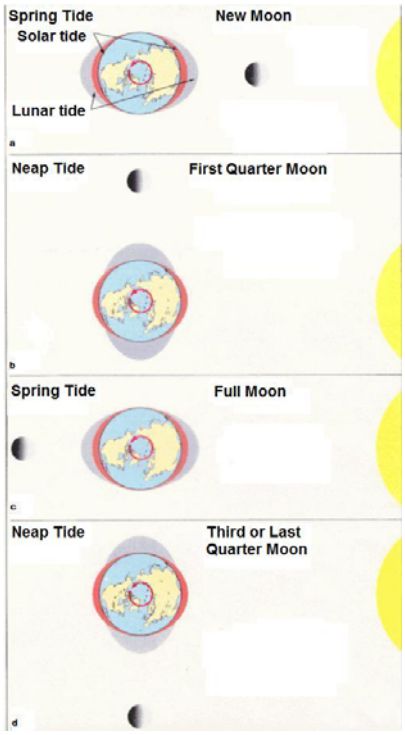

Figure 1.1: Formation of spring tide and neap tide due to the motion of Sun and Moon to the Earth [9]

Because of their unique characteristic, tides can be predicted with great accuracy. Therefore, tidal energy is more predictable, in comparison to other forms of renewable energy, which come from randomly intermittent and variable sources, such as wind and wave. The movement of seawater into and out of bays and estuaries driven by tides can create tidal currents[1], tidal ranges[2] or both. Some regions like headlands and straits can be associated with sizable tidal currents, where the speeds of currents are magnified by local topographical features. Both tidal ranges and tidal currents can be exploited for generating power.

'The utilization of tidal energy is not a new idea' [10]. In medieval times, people started to grind cereals using tidal flows to drive machinery, known as tide mills. These tidal mills have simple shapes and are vulnerable to damage from tidal surges. A famous example of the ancient tide mill is the Eling Tide Mill located in the UK, which has hundreds of years history but is still in operation now. Figure 1.2 shows a picture of the Eling tide mill.

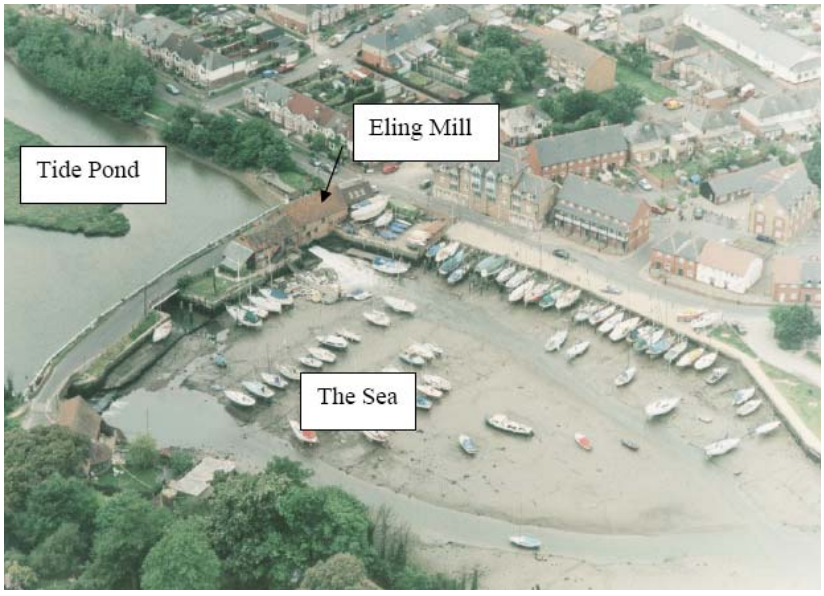

Figure 1.2: Aerial view of the Eling Tide Mill [11]

[1] Tidal current: Tidal currents (a horizontal motion) are a result of the rise and fall of the water level due to tides (a vertical motion).

[2] Tidal range: vertical distance between ebb and flood

Tidal barrages are large and expensive schemes to generate power using tidal ranges, which is constructed across an estuary or bay and equipped with sluices, gates and turbines. Tidal barrages work in the similar way to hydroelectric schemes. Water is trapped at high tide inside the estuary, using sluices. When tides on the other side of the barrage begin to fall to a certain level, a substantial water head is created between two sides of barrage. Water then is released through low head turbines to generate power. The largest tidal barrage in the world until now is that constructed in France, at La Rance in Brittany, which is shown in Figure 1.3. It started to operate in the 1960's and has a capacity of 240 MW [12].

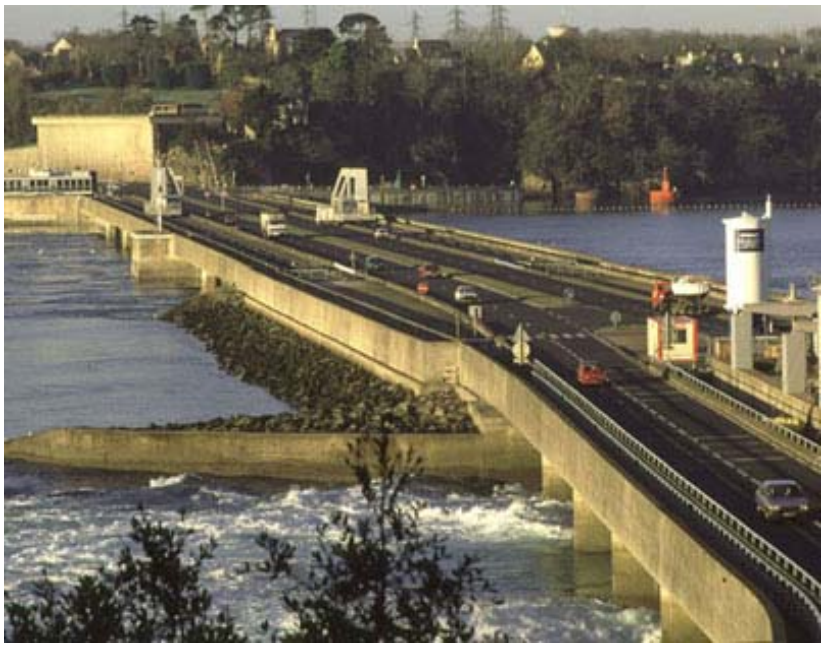

Figure 1.3: The tidal barrage at La Rance, France [13]

Tidal barrages need huge capital investment and have a long construction time. They can cause undesirable environmental and ecological impacts. For instance, the tidal barrage can take away mudflats important to birds and also can act as a barrier to the

passage of migratory fish such as salmon, shad and eels [14]. The development of tidal barrages therefore is limited.

Another technology being developed involves the utilization of tidal current energy. The kinetic energy from moving water is captured using tidal current energy converters as water flows naturally between high and low tides. The principle involved is very akin to harnessing wind energy and thus some tidal current energy converters superficially resemble wind turbines, and are called tidal current turbines. Tidal current technology has advantages over tidal barrage in that it has less environmental impact and it is also superior to other land-based renewables since the tidal current energy converters can be deployed on a grand scale under the sea surface and thus eliminate the constraints due to conflicts over land-use [15]. It is tidal current energy that is studied in this thesis.

1.2.2 Tidal Current Energy

Energy from Moving Water

The kinetic energy flux in a tidal current is determined by the velocity of water flowing through the cross-section of a channel and is expressed by equation (1.1) [10].

$$P(watts) = \frac{1}{2}\rho \int_A U^3 dA \tag{1.1}$$

where the ρ is the density of water (kg m^{-3}), U is the component of local water velocity perpendicular to the cross-sectional area of the channel. $\overline{U}$ is the mean velocity obtained by averaging the value of U and is used for simplifying equation (1.1).

$$P(watts) = \frac{1}{2}\rho A\overline{U_A}^3 \tag{1.2}$$

where $A\overline{U_A}^3 = \int_A (U^3 dA)$. Hence, the kinetic energy available in tidal current is highly sensitive to its velocity. Equation (1.1) can also, and more familiarly, be used to determine the kinetic energy flux passing through the swept area (A) of a conversion device.

The velocity of tidal currents U may be generally predicted using equation (1.3), which is an approximation of a tidal cycle with a double sinusoid [16] in which one is representing the diurnal tidal ebb and flow cycle and the other is representing the fortnightly (neap-spring) cycle.

$$U = \left[K_0 + K_1 \cos\left(\frac{2\pi \times t}{T_1} \right) \right] \cos\left(\frac{2\pi \times t}{T_0} \right) \tag{1.3}$$

where K_0 and K_1 are constants derived from the mean spring peak and the ratio between the mean spring peak and the mean neap peak currents. T_1 is normally 353 hours and is the spring neap period. T_0 is the semi-diurnal tidal period and is 12.4 hours. Other factors, which could cause significant influence on tidal current velocity, like waves on the surface, density changes and variation of water speed as a function of flow depth in an open channel, have to be considered and need to be reflected in the equations for tidal current velocity prediction. In practice, the velocity of tidal currents needs to be physically measured in order to precisely evaluate the local tidal current energy resources. An approach is also emphasised that full tidal statistics are important and need to be considered when estimating the current energy potential of a tide site, since there is a significant spatial variation in peak spring velocity.

Otherwise, the scale of available energy can be dramatically overestimated, if only maximum spring velocity is considered [10].

Site Requirements for Tidal Current Energy Exploitation

Although the global tidal current resources are huge, in most areas there is too low a power density, due to low current speeds, to be economically exploited. The sites, where tidal current speeds exceed 2 m s^{-1}, are believed to have relatively intensive renewable energy fluxes compared with other conventional renewables like wind and solar (see Table 1-1) and thus have the potential for commercial development.

Energy resource	Tidal Currents					Wind	Solar
Velocity (m s^{-1})	1	1.5	2	2.5	3	13	Peak at noon
Velocity (knots)	1.9	2.9	3.9	4.9	5.8	25.3	
Power density (kW m^{-2})	0.52	1.74	4.12	8.05	13.91	1.37	~1.0
Note: 13 m s^{-1} is a typical velocity at which maximum power is achieved for a wind turbine							

Table 1.1: Relative power density of marine currents with wind and solar resources [15]

In addition to the velocity of the tidal current, potential tide sites also need to meet other requirements in order to be effective for tidal current energy utilization. Water depth is crucial for tidal current energy converters installation and directly decides the size of tidal current energy devices [16]. The ideal water depth needs to be a minimum of 15 m at low tide, and at that depth the smallest rotor which can be accommodated is about 10 m diameter. Ideally, the maximum water depth at high tide probably is not more than 40 or 50 m, but the upper limit depends on the type of tidal current energy converters and the installation methods to be applied. A

suggested criterion for rotor diameters for a horizontal axis tidal current turbine, according to various water depths is shown in Table 1-2.

Water depth	Rotor diameter (assuming no shipping exclusion)	Rotor diameter (assuming shipping exclusion
< 20 m		10 m
20-25 m	5 m	120 m
25-40 m	10 m	20 m
> 40 m	20 m	20 m

Table 1.2: Influence of water depth on maximum permitted turbine size [17]

A general rule can be used in practice that the rotor diameter is half of the water depth and the centre of rotor should be at the midwater depth. In addition, a spacious seabed is needed to allow a large enough array of tidal current devices to be installed, which makes the overall project cost effective. A relative flat seabed also has advantageous in reducing ambient turbulence as well as the loss of tidal current velocity near the seabed. Sites should also be close to shore-based grid connections. Other factors associated with tide sites selection have also been discussed [16, 17].

Tidal Current Energy Resources

Comprehensive work has been carried out in the EU and the UK for assessing tidal current resources, and is in advance of other countries in the world. 106 locations have been suggested as being suitable for tidal current energy utilization in European waters by an EU sponsored study [18]. The total installed capacity of tidal current turbines in those selected sites could be over 12 000 MW and 48 TWh of electricity energy could be produced per annum. The UK has a large tidal current resource because of its natural geographic features [19-21]. Places like the Pentland Firth,

which lies between the north coast of the Scottish mainland and Orkney, can experience spring current speeds exceeding 7 m s^{-1} in some locations. Fast tidal currents are associated with intensive kinetic energy flux densities existing in these places and offer intriguing opportunities to be developed [22]. A DTI-funded project [19] identified the eight largest tidal sites in the UK, which may aggregately have 18-000 MW of installed capacity and could generate 62 TWh of electricity per annum if fully exploited. The promising tides sites in the UK are displayed in Figure 1.4. Undoubtly, if successfully developed, tidal currents could make significant contributions to the UK government target for CO_2 emission reduction without compromising the growing energy demand in the future.

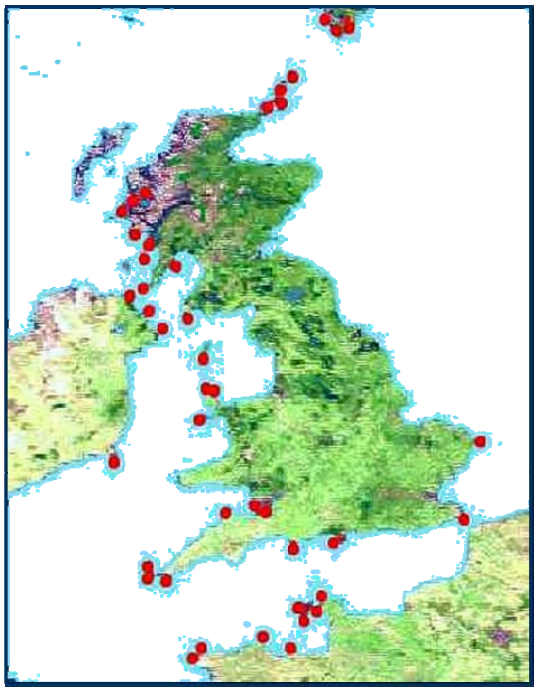

Figure 1.4: Promising tide sites in the UK [23]

1.2.3 Tidal Current Energy Converters

In principle, four fundamental concepts can be used for tidal current energy conversions [10] and all have been applied currently for the design of prototype tidal current energy converters.

- Horizontal axis turbines
- Vertical axis turbines
- Variable foil systems
- Venturi systems

Horizontal Axis Turbines

A horizontal axis tidal current turbine resembles a wind turbine and typically comprises a tall tower, a fan-like rotor for rotation about an axis parallel to the direction of flow, the generator, the controller and other components. The principle of operation for a horizontal axis turbine is that the inflow perpendicular to the rotor causes resultant hydrodynamic force, which has components acting normal to the axis of the rotor blade in the plane of rotation. The resulting torque is transferred by a shaft and gearbox to an electrical generator. Even though there exist many superficial similarities, a horizontal axis tidal current turbine is different from a conventional wind turbine in some ways, as they work in different resources: tidal currents and wind. Most horizontal axis turbines have three rotor blades, but two-blade rotors are simple mechanically and can be more easily handled under marine conditions; hence two-blade rotors are more favourable for commercial horizontal axis tidal current turbines [24]. Since the density of seawater is 800 times denser than air, the energy captured across the same swept area of the rotor blade is also 800 times more in

seawater than in air with same flow speeds. Therefore, a tidal current turbine can have smaller rotor blades and also a lower rotational speed compared to a wind turbine to capture the same amount of kinetic energy. Unlike wind, the direction of which varies, tidal currents are frequently close to being bidirectional. Wind turbines have to be yawed in order to face into the wind. But for tidal current turbines, only turbine blades need to be reversed and pitched through 180° in order to change turbine operating condition on a flood tide to an ebb tide. Turbine blades pitching could also be applied to achieve the optimum blade angle, keeping the most efficient performance of turbines in any given currents [24]. Cut-out speeds designed for a wind turbine to avoid damage in storms are not imperative for a tidal current turbine, given the predictable nature of the flow regime, but shut-down procedures have to be executed in emergency situations (e.g. loads caused by wave action in stormy conditions might be severe enough to trigger shut-down) [8].

The technology of horizontal axis turbines has moved into full-scale development. A representative example is the 'Seaflow' project carried out by Marine Current Turbines Ltd. and its partners in the UK. A 'Seaflow' turbine is demonstrated in Figure 1.5, which shows the turbine operating (left image) as well as being raised above the water for the maintenance (right image). More description of the 'Seaflow' project is available in the report of the UK Department of Trade and Industry [24].

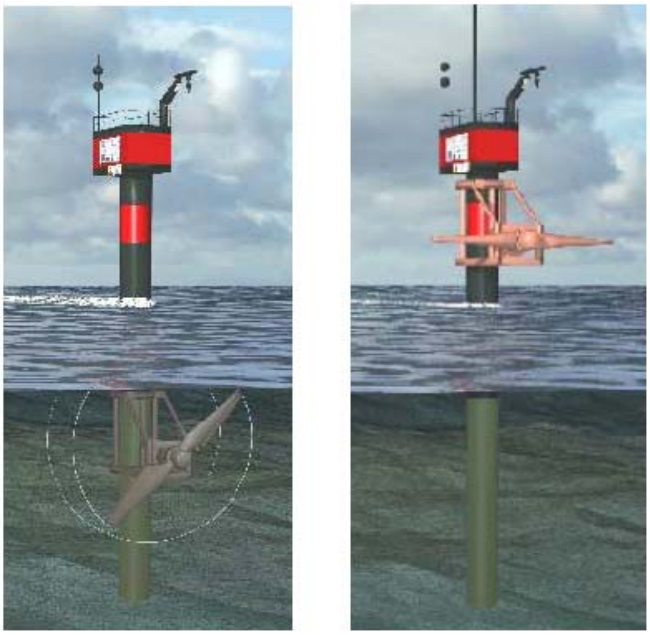

Figure 1.5: 'Seaflow': a horizontal axis tidal current turbine [24]

Vertical Axis Turbines

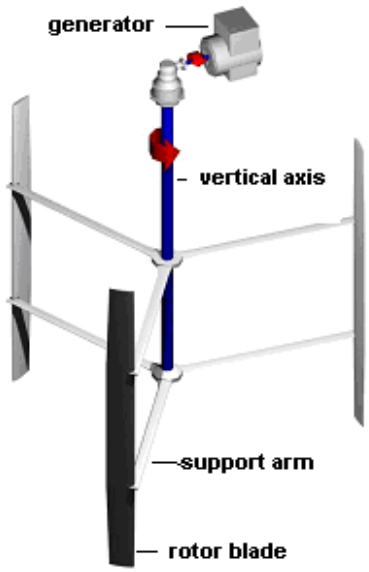

Figure 1.6: The schematic diagram of a Kobold turbine coupled with a generator [25]

The concept of a vertical axis tidal current turbine also is inspired by its wind counterpart, of which the fixed pitch Darrieus type is a common implementation. A schematic diagram of a vertical axis turbine is shown in Figure 1.6. The key feature

of a vertical axis turbine is its cross-flow design, in which the blades and rotor transmission shaft are parallel to one another and are both oriented perpendicular to the incoming current flow [26]. This configuration allows the rotor to always rotate in the same direction and be insensitive to tidal current direction. A vertical axis turbine has rectangular energy capture cross-section and, therefore, is suitable for work in shallower channel, where a horizontal axis turbine could prove difficult in making optimum use of the channel cross sectional area [27]. A conventional fixed pitch vertical axis turbine cannot usually start rotating on its own and only is able to work efficiently at very high tip speed ratios. As a result, a self-start motor will be required. Variable pitch vertical axis turbines have been proposed, which can markedly increase the power extraction efficiency at low tip speed through controlling the rotor blades pitch at all points of their rotation cycle. The Kobold turbine [28], installed in the Strait of Messina at Italy, is one prototype of variable pitch vertical axis turbines and has actually been tested. 'Polo' is another prototype under development currently and it is designed by Salter in the University of Edinburgh. Overall, vertical axis turbines are still in conceptual stages and there no full-scale prototype has been developed up to date. More description of vertical axis tidal current turbines is available in a report of the UK Department of Trade and Industry [27].

Variable Foil Systems

Unlike rotational tidal current turbines, which include horizontal and vertical tidal turbines described previously, another kind of tidal current converters comprises an oscillating hydrofoil and uses the oscillation motion of hydrofoil to extract energy

from tidal currents. One notable example is called ‘Stingray’, designed by Engineering Business Ltd. in the UK and its image is shown in Figure 1.7.

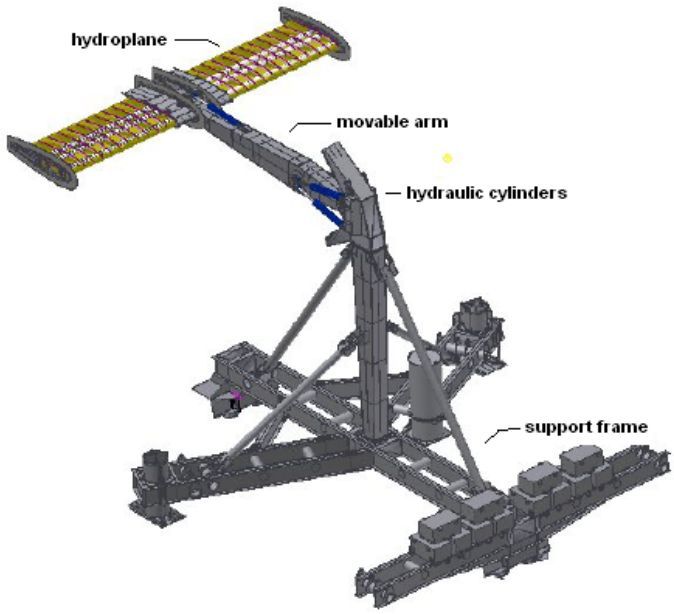

Figure 1.7: ‘Stingray’ produced by Engineering Business Ltd. [30]

The main mechanical components of a ‘Stingray’ include the wing-like hydroplane, movable arm, supporting frame and hydraulic cylinders. The hydroplane is attached to the seabed mounted supporting frame by the movable arm. Hydraulically powered cylinders are set at the arm/frame pivot and are used to alter the hydroplane angle relative to the oncoming current [29]. The operating principle of ‘Stingray’ appears straightforward. When the tidal current passes over the hydroplane, lift and drag forces cause the hydroplane as well as the movable arm to lift. The motion of the movable arm actuates hydraulic cylinders. The high-pressure oil developed by the cylinders turns a hydraulic motor that, in turn, drives an electric generator [30]. Another cycle will start again at the upper limit of hydroplane and arm, as the hydroplane angle is reversed and thus the arm is driven down. A full-scale ‘Stingray’ demonstrator was constructed by the Engineering Business Ltd. Its

hydroplane was 15 m wide and the whole structure was 24 m high. This demonstrator has also been tested by immersing it off the Shetland Islands in Yell Sound, UK in 2002. More description of the 'Stingray' project is available in the report of the UK Department of Trade and Industry [31].

Venturi Systems

Rochester venturi (RV) and GENTEC venturi are two tidal current energy converter concepts based on venturi systems. Rochester venturi developed by Hydroventuri Ltd. is a pressure amplifier using Bernoulli's principle. The device is placed in the core of tidal current. As the primary flow (tidal current) passes through the device, its speed is accelerated and thus generates a reduction in pressure at the point where that flow is most constricted [32]. This reduction in pressure can then suck more flow from another location into the primary flow. It is this secondary flow that is used to drive the on-shore turbine and generate the electricity. Rochester venturi has no moving mechanical and electrical parts below water, thus saving the considerable maintenance and operational costs. Figure 1.8 shows the 60kW primary circuit model being installed.

GENTEC venturi is developed by Greenheat Systems Limited. It uses a duct system and consists of an axis flow rotor with fix-pitch blades, which is mounted in the cylinder duct or venturi shroud [33]. Each unit is designed to be set on a buoyant carrier platform and can be deployed in any depth of water.

Figure 1.8: Primary circuit demonstrator of Rochester venturi being installed [32]

1.2.4 Contemporary Developments of Tidal Current Energy

Tidal current energy comes from a natural source with many benefits, but it is a young technology relative to either wind energy or wave energy. The main reason is that tidal current was beyond the scope of human accessibility a few decades ago. Technical challenges caused the cost of capture to be prohibitively high for tidal current, in the region of 17-39 p/kWh for the two most promising sites in the UK [21]. This conclusion from the 'UK tidal stream energy review' in 1993 appeared to deem tidal current energy commercially unattractive and official support for the development of this technology in the UK was suspended. However, it was not the end of interest in tidal current energy and some independent organizations continued their research programmes.

A 3.5 m diameter horizontal axis tidal current turbine was first tested at Loch Linnhe, Scotland in 1994 as part of a "Proof of Concept" experimental tidal current

system supported by IT power, Scottish Nuclear and the National Engineering Laboratory (NEL). This project proved the viability of producing power via a tidal current turbine and is regarded as the starting point for the present activity of tidal current turbine development [34]. An assessment of tidal current energy resources in Europe was conducted by the support of the Directorate General XII (DGXII) of the European Union (EU), which was completed in 1996. A massive tidal energy resource in the European water was recognized in this study. Those factors critical to the electricity cost from tidal current turbines were identified through examining the relevant technology in the areas of wind, hydropower, maritime and offshore. 'It estimated electricity unit costs for "First Generation systems" deployed on a small scale at around 0.05 ECU/kWh (3.5p/kWh) for a 3 m s^{-1} rated current under favourable circumstance (i.e. with a high load factors[3])' [35].

The Regional and Urban Energy Programme, DGXVII of the EU financed a feasibility study on supplying Orkney and Shetland, Scotland with electricity generated from tidal current turbines [23]. An initial market for the electricity from tidal currents is most likely to be remote and island communities, which usually have higher than normal conventional energy costs. The study showed that a cluster of 8 turbines of 20 m diameter provided a predicted electricity cost of approximately 6 p/kWh. The large-scale installation of tidal turbines would further reduce the costs. Those judgements on the possibility of commercialisation were recognized by the conclusion of a DTI report published in 2001. It estimated that the unit cost of energy for a scheme containing 30 baseline 1MW units could be 4.56 p/kWh, with a discount rate of 8% over 29 years [36]. This report shed new light on the commercial viability of tidal current energy and renewed the government interest in this

[3.] High load factor: Load factors are used to relay the percentage of the year that generator operate at full capacity

technology. The ‘Seaflow’ project is one of the most significant developments of tidal current technology in recent years. A first full-scale tidal current turbine rated at 300kW, was installed off Lynmouth, Devon in 2003, by Marine Current Turbines Ltd. and has been operating successfully until now. The subsequent phases of the project are named ‘SeaGen’ and its ultimate aim is ‘to install the first “farm” of tidal current turbines involving up to 10 units and give an aggregate power for thesystem of around 10 MW’ [37]. Figure 1.9 demonstrates an artist’s impression of a future tidal current turbine ‘farm’. Other remarkable progress also includes the successful installation and test of a 150 kW tidal stream generator: ‘Stingray’ in Yell Sound off the Shetland Islands in 2002 as well as the installation of the world’s first grid-connected tidal current turbine by Hammerfest Strøm, Norway in 2003. Tidal energy research programmes are also emerging in other countries like United States and Canada, but all lag behind UK.

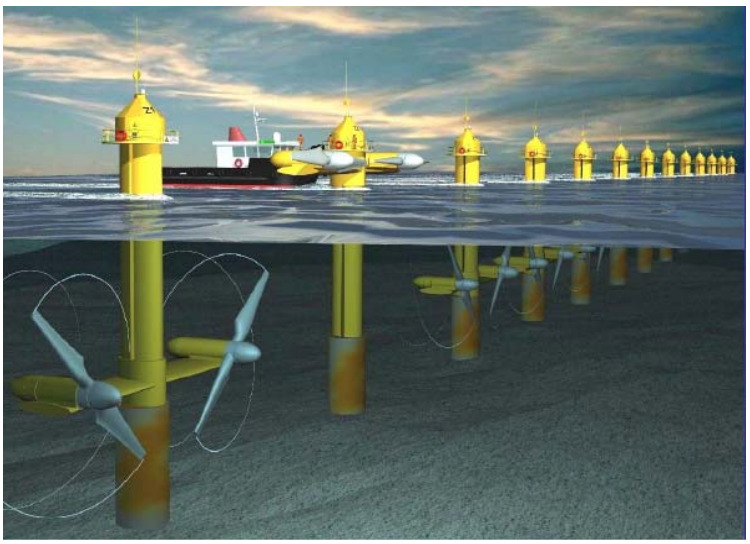

Figure 1.9: Arist’s impression of a future farm of two-rotor tidal current turbines [37]

1.3 Current Research on Utilization of Tidal Currents

The accumulation of knowledge related to tidal current resources, the physical process involved in tidal current energy extraction and its consequence, are essential if this natural resource is to be successfully exploited. Further cost reduction, which makes the electricity from tidal currents 'market competitive' with other renewables, even with conventional fossil fuels, substantially depend on promoting the technology. However, the development of scientific understanding in tidal current energy is just at an embryonic stage and lags far behind many of its competitors, such as wind and wave. At present, both experimental investigation and numerical modelling of the tidal flow regime is rudimentary. A paucity of information regarding various issues associated with tidal current energy is a feature in this new area of research [38].

1.3.1 Numerical Modelling

At the beginning stage of utilization of tidal currents, two topics, which are of most interest for researchers, are assessing tidal current resource and validating the concept of tidal current device. Tidal current resource assessment is essential to explore the economic feasibility of tidal energy utilization and identify promising tidal sites for exploitation. Different from wind, it is expensive and difficult to measure tidal current speed in the field. Therefore, a variety of numerical techniques has been studied and applied to model tidal flow, in order to allow a greater understanding of the nature and magnitude of tidal current energy resources [39- 43].

Numerical methods are widely used during tidal current device design. Some theoretical methods which are used for wind turbines have also been applied for horizontal axis tidal current turbine, with considering the difference between air and water. By simulating tidal current device operation, the characteristics of the device can be predicted and its design can be validated and optimized. Therefore, time and expenses can be saved by effectively reduce the number of experiments to be performed [44-47].

As mentioned in section 1.2.3, full-scale prototype of tidal current devices have been successfully installed and tested in the open sea. The utilization of tidal current energy is expected to be commercialized in next few years. As individual device is unlikely to exceed rated capacities of 2MW, tidal current devices will need to operate together at a tidal site, forming a 'farm' in order to maximize the energy extraction and reduce the generation costs. However, the impacts of large-scale energy extraction from tidal currents on the local flow regime have not been completely studied. Preliminary numerical assessments of the amount of extractable energy from tidal current are mainly concentrated on the energy potential in a channel based on theoretical energy flux calculations across the channel cross section. But 'the estimation of the exploitable resources should take into account environmental, economic and social constraints' [17]. It has been understood that energy extraction from tidal currents could cause significant changes in the hydraulic nature of the channel [48], because the tidal current energy comes from a heavily constrained flow [49]. In the exploitation of wind energy, devices simply skim kinetic energy from the bottom of atmosphere, which represents a tiny proportion of the total kinetic flux from the earth's surface upwards. In contrast, the tidal devices will typically extract

an appreciable proportion of the kinetic flux and will be placed relatively close to the upper boundary of flow environment – the free surface between the water and the air [50]. Therefore, the response of the fluid environment to the tidal current energy extraction could be a more complex three dimensional problem. Directly applying the methodologies used for studying wind energy extraction to the tidal current energy extraction can lead to serious misunderstanding. It is the local consequence of energy extraction from tidal currents that has been studied in this research, of which little has been done before. Computational fluid dynamics (CFD) method was employed to simulate the energy extraction from tidal currents, and a novel approach was taken to track the variation of free surface by using Volume of Fluid (VOF) method instead of simplifying the free surface as a 'rigid-lid'. In addition, the influence of some important parameters, like freestream turbulence, submerged water depth and freestream velocity, were also examined using the established numerical model.

1.3.2 Experimental Testing

Current research on experimental study of tidal current energy devices concentrates on laboratory testing and measuring the performance of tidal current devices at different scales, in order to validate the concept and optimize the device design. This proof-to-concept study is imperative, before the device may appeal to potential investors and a full scale prototype will be constructed. Power output and loading on the device and support structure over a range of flow conditions are main characteristics being measured in these experimental tests [51-55]. Therefore, the region where interaction between tidal current device and fluid flow happens is the

most common interest for researchers at this stage. However, as large tidal farms will be deployed in the near future, understanding the flow characteristics downstream of tidal current devices is important not only for the optimal layout of devices but also for forecasting of an energy output of a tidal 'farm'. Thus, experimentally study of the flow features of the wake behind a tidal current device is becoming a scientific topic of interest to researchers [56].

The laboratory testing of scale model tidal current devices is still an embryonic activity. As a result, experimental facility specifically designed to study the physical properties of tidal current devices, as well as the related physical processes involved in the energy extraction from moving water, is presently under development. It is known to be difficult to accurately achieve flow stability in large moving water channels under laboratory conditions, especially considering the technical problems associated with moving large volumes of water around. For instance, a relatively high capacity pump is necessarily required to supply a recirculating, fast-moving, stream of water. Therefore, the existing water flumes in the laboratory can not be employed for the performance testing of tidal current devices at different scales, because of their relatively small dimensions. Instead, a towing tank has been used [52, 55]. As the real operating environment for a tidal current device is in moving water, verifying the suitability and identifying the limitations of using the towing tank for laboratory testing of tidal current devices are valuable in the research and development of tidal current energy technology.

1.4 Aim of the Study

The work reported in this thesis represents an attempt to add pieces of knowledge into these new research topics arisen from the current development of tidal current energy utilization, which has rarely been touched before. Therefore, the objectives of this study can be stated as follows:

1. to use the computational fluid dynamics (CFD) approach to simulate the flow region around tidal current energy converters with consideration of the free water surface;
2. to investigate the influence of environmental parameters on tidal current energy extraction by using an established 3D numerical model;
3. to carry out experimental investigation of energy extraction from tidal currents in a natural open channel;
4. to carry out experimental investigation of energy extraction from tidal currents in a towing water tank;
5. to validate the numerical model using the experimental data and assess the discrepancies between the experimental results obtained under different measurement conditions.

1.5 Layout of Thesis

Research work completed in the past three years has been divided into chapters and is presented sequentially in this thesis. A brief word in front of each chapter as to its content may be useful to the reader. Separate chapters have been used to describe

distinct area of work conducted. There has also been some interaction and cross referencing.

In this chapter, the motivation and study objectives have been elaborated. In addition, background knowledge associated with diverse aspects of tidal current energy has been highlighted.

Chapter 2 focuses primarily on the development of 2D and 3D numerical models for simulating the energy extracted from tidal currents, but also describes some background knowledge about CFD. The parameters of the numerical model described in this chapter were intentionally set to the relatively large values, and thereby the results obtained from numerical simulation only aimed to provided an essential insight into the influence of massive tidal current energy extraction on the flow regime in an open channel. The numerical model has been modified afterwards, in order to match the experimental conditions implied for the validation of numerical predictions.

The influence of prime parameters on the energy extraction is identified based on the numerical model established in Chapter 2 and is discussed in Chapter 3.

In order to validate numerical results, two experimental measurement approaches were carried out respectively in moving water and still water. Perforated disks were used to represent a horizontal-axis tidal turbine and were tested in the experiments. Drag force coefficient of the disk and the velocity field in the wake of the disk were measured. The experimental set-up and results have been reported separately in Chapter 4 and Chapter 5.

In Chapter 6, the proposed numerical model was modified to simulate the experimental test. The actuator disk in the numerical model was defined according to

the characteristics of the perforated disk tested in the experiment, so that the comparisons of numerical and experiment results for the velocity profiles in the wake of perforated disk can be conducted. In addition, measurements results of the wake velocity profiles under two different experimental conditions are also compared against each other and the discrepancies have been explained.

The primary conclusions, as well as author's recommendations for the following work, are presented in chapter 7.

Chapter 2

NUMERICAL MODELLING OF ENERGY EXTRACTION FROM TIDAL CURRENTS

Overview

This chapter describes the numerical models that have been developed for modelling the energy extraction from tidal currents, using the commercial computational fluid dynamics code, FLUENT^{TM}. Background knowledge of computational fluid dynamics is necessary and is described in section 2.1. The process of problem solving in FLUENT^{TM} is outlined in section 2.2. The setup of a two-dimensional (2D) model of energy extraction is described in detail in section 2.3. The numerical model is further extended to three-dimensions (3D) and is described in section 2.4. Conclusions based on numerical model results are stated in section 2.5.

2.1 Introduction of Computation Fluid Dynamics

2.1.1 Computational Fluid Dynamics (CFD)

The physical aspects of any fluid flow are governed by three fundamental principles: (1) mass is conserved; (2) Newton's second laws (force = rate of change of momentum); (3) energy is conserved. All of these principles can be expressed using basic mathematical equations, which are generally in the form of integral equations or partial differential equations, and for those equations, analytical solutions are unavailable. Computational fluid dynamics is the art of replacing the integrals or the partial derivatives in these equations with discretized algebraic forms, which in turn are solved to obtain numbers for the flow field values at discrete points in time and/or space [57]. In short, computational fluid dynamics is a numerical technique to solve and analyze the fluid flow problem with the aid of computers. Therefore, development of CFD is closely linked with the evolution of modern computers. That the accuracy of CFD solution can be achieved and the details of fluid flow can be modelled is very much dependent on advances in computer hardware, particular related to CPU speed and storage capacity. CFD methods can provide an insight into the sophisticated fluid flow phenomena in the area, where the experimental instruments have difficulty in reaching, for example the blood flow in human arteries. CFD methods can also be used to give predictions before physical experiments in order to save costs and improve efficiency. Because of those advantages, nowadays CFD is widely applied in nearly all disciplines where fluid flow is important and has been viewed as a 'third-approach' to the study of fluid

dynamics, complementing the other two conventional methods: pure theory or pure experiment.

There are three main stages enclosed in every CFD simulation process: preprocessing, solver and post process [58].

Preprocessing

The first step for CFD simulation is used to define the geometry of flow model to be solved and build the computational grid. A numerical grid is a discrete representation of the geometric domain on which the problem is to be solved and divides the solution domain into a finite number of cells [59]. Computer-Aided Design (CAD) package can be used for generating computational grids and some CFD software packages own their preprocessing tools like GAMBIT which is used in FLUENT. There are generally structured or unstructured girds that can be generated according to the geometry of flow domain defined. In structured girds, the grid cells lies in regular rows and columns. Cell shapes are dominated by quadrilaterals in two-dimensional solution domains or hexahedrons in three-dimensional solution domain. In unstructured grids, cells are constructed in an irregular pattern. Triangular cells (2D) and tetrahedral cells, wedge cells or pyramid cells (3D) are employed in unstructured grids. The accuracy of a CFD solution is highly dependent upon the number of cells in its computational grid. In the preprocessing stage, the fluid properties and the conditions along the boundary of solution domain also need to be appropriately set.

Solver

The CFD solver conducts the flow calculations and obtains the numerical results by solving the governing equations. Discretization of the governing equations is a crucial process in the solver and the flow equations need to be expressed in a discrete form at each point in the computational grid. There are three methods for discretizing the governing equations: finite difference, finite volume and finite element. The finite volume method (FVM) has been employed in many commercial CFD softwares, including FLUENT and is described in detail in the book of Versteeg and Malalasekera (1996), which is summarized here. To use the finite volume method, firstly the solution domain needs to be subdivided into a finite number of contiguous control volumes (CVs), which are small volumes surrounding each node point in the computational grid. The node point is the centroid of one CV. Then the differential form of the governing equations is integrated over each CV and the values of flow variables calculated are stored in the centroid of CV. The values of flow variables at the surface of one CV are expressed in terms of the centroid values of all its neighbouring cells that share the same cell face by using suitable interpolation schemes. In this manner, the discretization equations for one CV include the unknown variables at its centroid as well as the unknown variables at the centroids of its neighbouring cells. Thus, those are a set of algebraic equations for each CV that can be solved iteratively. The finite volume method is a conservative method because it defines that fluxes such as mass, momentum, energy and species entering a given CV is identical to the fluxes leaving the adjacent CV. Therefore, the finite volume methods can be utilized for any type of grids, especially complex geometries. The terms that need to be interpolated using the finite volume method have physical

meanings, thus the finite volume method is readily understood by engineers and can be readily programmed. However, since two levels of approximation: interpolation and integration are needed, it is difficult to use any scheme higher than second-order in the finite volume method in order to achieve more accurate numerical solutions in 3-dimensions. Except finite volume method, finite element method (FEM) is also extensively used in science and engineering. According to Saxena and Sahay [60], mesh generation is a preprocessing step to FEM, involving discretization of a solid model into a set of points called nodes on which the numerical solution is to be based. Finite elements are then formed by combining the nodes in a predetermined topology (linear, triangular, quadrilateral, tetrahedral or hexahedral). Discretization is an essential step to help the finite element method solve the governing differential equations by approximating the solution within each finite element. The accuracy of an FEM solution depends on the fineness of discretization in that for a finer mesh, the solution accuracy will be better. FEM can be powerfully adapted to problems of great complexity and unusual geometry. In the finite difference method (FDM), the computational domain including the boundary of the physical problem is covered by a grid or mesh. At each of the interior grid point, the original differential equations are replaced by equivalent finite difference approximation. In making this replacement, an error which is proportional to the size of the grid is introduced. This error can be reduced by making the grid size smaller to get an accurate solution within some specified tolerance.

Postprocessing

This is the final step in the CFD simulation. The numerical results produced from the solver are presented and analyzed using different postprocessing tools. Many

CFD softwares have versatile data visualization functions to generate high-resolution CFD images and animations, which are helpful to interpret the numerical results and understand the complex flow phenomena easily.

2.1.2 The Governing Equations of Fluid Flow

The mathematical equations must be solved to generate numerical solutions for any fluid flow problems. There are many textbooks available on fluid dynamics to explain the governing equations in details [61, 62]. Only a brief description about the governing equations is given in this section.

Continuity Equation

The continuity equation is a mathematical representation of the law of conservation of mass and is described as 'in a given volume of fluid, the rate of increase of mass inside that volume must be equal to the net rate of flow of mass into that volume across its face' [58].

Rate of increase of mass in a control volume	=	Net rate of flow of mass into a control volume

The continuity equation can be expressed as equation 2.1 in a Cartesian coordinate system.

$$\frac{\partial \rho}{\partial t} + \frac{\partial (\rho u)}{\partial x} + \frac{\partial (\rho v)}{\partial y} + \frac{\partial (\rho w)}{\partial z} = 0 \qquad (2.1)$$

For an incompressible fluid, the density ρ is constant and equation 2.1 becomes

$$\frac{\partial u}{\partial x}+\frac{\partial v}{\partial y}+\frac{\partial w}{\partial z}=0 \tag{2.2}$$

In tensor notation, x_i ($i=1, 2, 3$) represents the x, y, z coordinates respectively, correspondingly u_i ($i=1, 2, 3$) are the velocity components as u, v, w in the $i^{'}$th direction. Therefore, the continuity equation (2.2) can be written shortly as

$$\frac{\partial u_i}{\partial x_i}=0 \tag{2.3}$$

where a repeat suffix indicates summation.

Navier-Stokes equations

The Navier-Stokes equations are named after Claude-Louis Navier and George Gabriel Stokes who were two 19th century scientists who first derived the equations independently. Navier-Stokes equations are a set of mathematical expressions of the motion of fluid based on Newton's second law and it is stated that 'the rate of change of momentum of a fluid particle equals the sum of the forces on the particle' [58].

Rate of increase of momentum = Sum of forces on fluid particle of fluid particle

For three-dimensional, unsteady, Newtonian and incompressible fluids, the Navier-Stokes equations are written as equation (2.4a-c) in Cartesian coordinates.

The x-component of the Navier-Stokes equations:

$$\rho\left[\frac{\partial u}{\partial t}+u\frac{\partial u}{\partial x}+v\frac{\partial u}{\partial y}+w\frac{\partial u}{\partial z}\right]=\mu\left[\frac{\partial^2 u}{\partial x^2}+\frac{\partial^2 u}{\partial y^2}+\frac{\partial^2 u}{\partial z^2}\right]-\frac{\partial p}{\partial x}+X \tag{2.4a}$$

The y-component of the Navier-Stokes equations:

$$\rho\left[\frac{\partial v}{\partial t}+u\frac{\partial v}{\partial x}+v\frac{\partial v}{\partial y}+w\frac{\partial v}{\partial z}\right]=\mu\left[\frac{\partial^2 v}{\partial x^2}+\frac{\partial^2 v}{\partial y^2}+\frac{\partial^2 v}{\partial z^2}\right]-\frac{\partial p}{\partial y}+Y \tag{2.4b}$$

The z-component of the Navier-Stokes equations:

$$\rho\left[\frac{\partial w}{\partial t}+u\frac{\partial w}{\partial x}+v\frac{\partial w}{\partial y}+w\frac{\partial w}{\partial z}\right]=\mu\left[\frac{\partial^2 w}{\partial x^2}+\frac{\partial^2 w}{\partial y^2}+\frac{\partial^2 w}{\partial z^2}\right]-\frac{\partial p}{\partial z}+Z \tag{2.4c}$$

where ρ is the fluid density, μ is the fluid dynamic viscosity. u, v, and w are the velocity components in the x, y, and z directions. X, Y, and Z are the body forces (e.g. gravity force) components per unit volume in three directions. p is the pressure.

On the left side of equations, there are the total accelerations in three directions. On the right side of equations, there are the resultant force acting on the fluid particle, which consists of body forces and surface forces. In most cases, the body force of interest is the weight of the fluid particle. Surface forces are represented in terms of normal stresses and shear stresses which act on the surface of the fluid particle and are induced by pressure and fluid viscosity.

In tensor notation, Navier-Stokes equations are often written in the short form below

$$\rho\frac{\partial u_i}{\partial t}+\rho u_j\frac{\partial u_i}{\partial x_j}=\mu\frac{\partial^2 u_i}{\partial x_j\partial x_j}-\frac{\partial p}{\partial x_i}+X_i \tag{2.5}$$

where X_i is a body force per unit volume in the $i^{'}$th direction.

2.1.3 Turbulence Modelling

Turbulent Flow

Turbulent flow is the most common type of flow encountered in engineering practice, but it is still a little understood physical phenomenon in nature. Osborne Reynolds first demonstrated the difference in laminar flow and turbulent flow in his experiments in the late 19th century and he proposed an important dimensionless number from those experiments used to identify laminar flow and turbulent flow. This number, which is named after him, is called 'Reynolds number'. The Reynolds number is defined as the ratio of inertial forces to viscous forces in the given flow and is calculated using equation (2.6).

$$R_e = \frac{\rho U_\infty L}{\mu} \tag{2.6}$$

where ρ is the fluid density, U_∞ is the free stream fluid velocity, L is the characteristic length scale of the flow and μ the fluid dynamic viscosity. At low Reynolds number (R_e < 2100 for pipe flow), the fluid is laminar, which moves smoothly in parallel layers without disruption between layers. Therefore, the diffusive transport of momentum, heat and mass in the laminar flow occurs slowly at molecular scale and the flow variables such as velocity and pressure are independent from time. Laminar flows can be solved directly using the governing equations. At high Reynolds number (R_e > 4000 for pipe flow), the fluid behaves randomly and chaotically. The fluid becomes intrinsically unstable and the flow variables change rapidly in both space and time, which is called the turbulent flow. Laminar and turbulent flow demonstrated in Osborne Reynolds' experiment is shown in Figure 2.1.

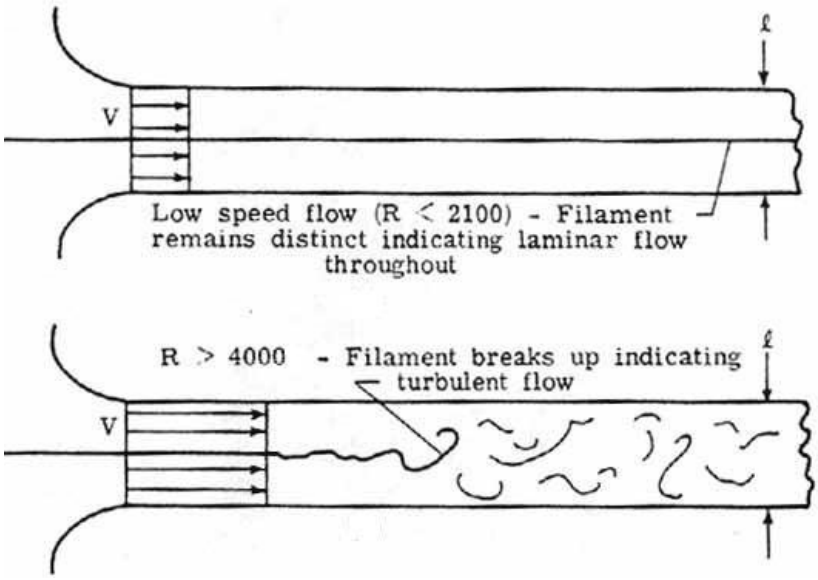

Figure 2.1: Laminar and turbulent flow [63]

Thus, the turbulent flow is described as follows [64]:

'Turbulent fluid motion is an irregular condition of flow in which various quantities show a random variation with time and space co-ordinates so that statistically distinct averages can be discussed.'

Turbulent flows can be produced either when the fluid flows past a solid surface or when neighbouring parallel streams of the same fluid flow one over another [65]. Therefore, the turbulent flows can be generally classified two types: wall turbulent shear flows and free turbulent shear flows. Air flows over the wing of aeroplane and developing or developed flows in a straight pipe, which is shown in Figure 2.2, are examples of wall turbulent shear flows. The turbulent flows which are not confined by the solid walls, like a turbulent wake formed behind a bluff body or a turbulent jet discharged from a nozzle, which is displayed in Figure 2.3, are free turbulent shear flows.

Figure 2.2: Wall turbulent shear flow: flow in a pipe [66]

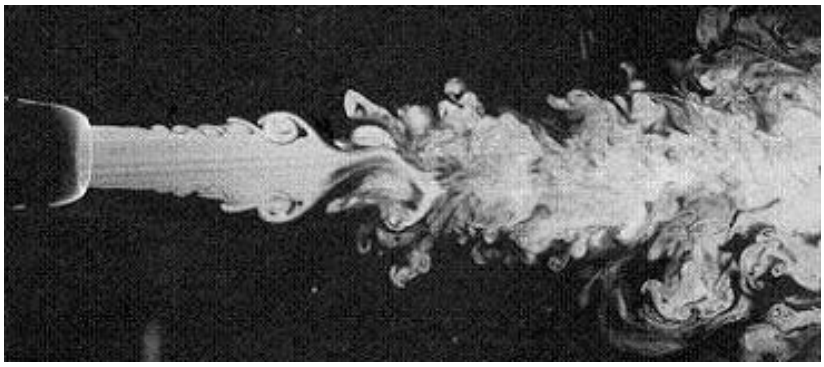

Figure 2.3: Free turbulent shear flow: a jet [67]

In the turbulent flow, swirling eddies with various sizes are contained, which extract the energy from the mean flow through the process of vortex stretching to maintain their motions and eventually dissipated their energy as heat. As a consequence, turbulent flow is associated with a high mechanical energy loss. Those eddies move randomly around and interact each other and make the mixing of mass, momentum and energy in the turbulent flow very effective. At any point in the turbulent flow, those eddies past that point, with a wide range of length and time scales, cause fluctuations of the flow variables with different frequencies and amplitudes, as shown in Figure 2.4.

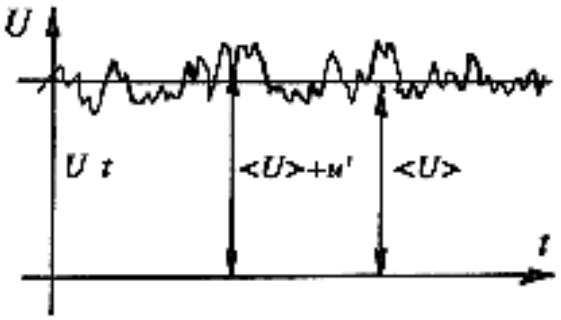

Figure 2.4: Velocity at a point in the turbulent flow as a function of time [68]

Therefore, the mathematical description of instantaneous velocity component (u, v, w) and pressure p in the turbulent flow needs to be decomposed into a time-average value $(\bar{u}, \bar{v}, \bar{w}, \bar{p})$ with a fluctuating value (u', v', w', p') superimposed on it, as follows:

$$u = \bar{u} + u'$$

$$v = \bar{v} + v'$$

$$w = \bar{w} + w'$$

$$p = \bar{p} + p'$$

Use the above substitutions into the governing equations (2.2) and (2.4a-c) to get equations for describing the turbulent flows.

Continuity equation:

$$\frac{\partial(\bar{u} + u')}{\partial x} + \frac{\partial(\bar{v} + v')}{\partial y} + \frac{\partial(\bar{w} + w')}{\partial z} = 0 \tag{2.7}$$

Also

$$\overline{\frac{\partial(\bar{u} + u')}{\partial x}} + \overline{\frac{\partial(\bar{v} + v')}{\partial y}} + \overline{\frac{\partial(\bar{w} + w')}{\partial z}} = \frac{\partial \bar{u}}{\partial x} + \frac{\partial \bar{v}}{\partial y} + \frac{\partial \bar{w}}{\partial z} = 0 \tag{2.8}$$

Equation (2.8) is the continuity equation for the time-average velocity components $\bar{u}$, $\bar{v}$ and $\bar{w}$ in the turbulent flow and can be written in tensor notation

$$\frac{\partial \overline{u_i}}{\partial x_i} = 0 \tag{2.9}$$

Reynolds-Averaged Navier-Stokes (RANS) equations:

Similar processes can be applied for three momentum equations (2.4a-c) and get the final equations (2.10a-c), which are commonly known as the 'Reynolds equations of motion' for a turbulent fluid.

$$\rho\left(\frac{\partial \bar{u}}{\partial t} + \bar{u}\frac{\partial \bar{u}}{\partial x} + \bar{v}\frac{\partial \bar{u}}{\partial y} + \bar{w}\frac{\partial \bar{u}}{\partial z}\right) = X - \frac{\partial \bar{p}}{\partial x} + \mu\left(\frac{\partial^2 \bar{u}}{\partial x^2} + \frac{\partial^2 \bar{u}}{\partial y^2} + \frac{\partial^2 \bar{u}}{\partial z^2}\right) - \left(\frac{\partial \rho \overline{u'^2}}{\partial x} + \frac{\partial \rho \overline{u'v'}}{\partial y} + \frac{\partial \rho \overline{u'w'}}{\partial z}\right) \tag{2.10a}$$

$$\rho\left(\frac{\partial \bar{v}}{\partial t} + \bar{u}\frac{\partial \bar{v}}{\partial x} + \bar{v}\frac{\partial \bar{v}}{\partial y} + \bar{w}\frac{\partial \bar{v}}{\partial z}\right) = Y - \frac{\partial \bar{p}}{\partial y} + \mu\left(\frac{\partial^2 \bar{v}}{\partial x^2} + \frac{\partial^2 \bar{v}}{\partial y^2} + \frac{\partial^2 \bar{v}}{\partial z^2}\right) - \left(\frac{\partial \rho \overline{u'v'}}{\partial x} + \frac{\partial \rho \overline{v'^2}}{\partial y} + \frac{\partial \rho \overline{v'w'}}{\partial z}\right) \tag{2.10b}$$

$$\rho\left(\frac{\partial \bar{w}}{\partial t} + \bar{u}\frac{\partial \bar{w}}{\partial x} + \bar{v}\frac{\partial \bar{w}}{\partial y} + \bar{w}\frac{\partial \bar{w}}{\partial z}\right) = Z - \frac{\partial \bar{p}}{\partial z} + \mu\left(\frac{\partial^2 \bar{w}}{\partial x^2} + \frac{\partial^2 \bar{w}}{\partial y^2} + \frac{\partial^2 \bar{w}}{\partial z^2}\right) - \left(\frac{\partial \rho \overline{u'w'}}{\partial x} + \frac{\partial \rho \overline{v'w'}}{\partial y} + \frac{\partial \rho \overline{w'^2}}{\partial z}\right) \tag{2.10c}$$

In tensor notation, a shorthand expression for the equations (2.10a-c) is

$$\rho\left(\frac{\partial \overline{u_i}}{\partial t} + \overline{u_j}\frac{\partial \overline{u_i}}{\partial x_j}\right) = X_i - \frac{\partial \bar{p}}{\partial x_i} + \mu\frac{\partial^2 \overline{u_i}}{\partial x_j \partial x_j} - \frac{\partial\left(\rho \overline{u_i' u_j'}\right)}{\partial x_j} \tag{2.11}$$

The principal part of equations (2.10a-c) look identical to the Navier-Stokes equations (2.4a-c) except that the velocity and pressure terms used in the equations (2.10a-c) are time-average rather than instantaneous values. The new terms appear in the last parenthesis on the right side of equation (2.10a-c) including only the fluctuating velocities. Those terms named as the 'Reynolds stresses' are 'the mean

forces (per unit area) imposed on the mean flow by the turbulent fluctuations'. The Reynolds stresses are additional unknowns and mean the governing equations for the turbulent flows are not closed. Thus some extra assumptions about the Reynolds stresses are needed.

Turbulence Models

'A turbulence model is a computational procedure to close the system of mean flow equations, so that a more or less wide variety of flow problems can be calculated.' [58].

For most engineering purposes, the details of turbulent fluctuations are not usually sought and only the effects of turbulence on the mean flow are of most interest. In particular, the Reynolds stresses in equations (2.10a-c) need to be modelled so that the time-average values for the turbulent flow can be obtained by solving the governing equations. A large variety of turbulence models with different degrees of complication and completeness have been proposed to deal with different kind of turbulent flows. They are normally 'semi-empirical' and are based on the assumption about turbulent processes. Generally, there are two groups of turbulence models: the classical models and large eddy simulation.

The classical models use the Reynolds averaged Navier-Stokes equations (RANS) to get the mean flow pattern with the whole range of turbulence scales being modelled. Those models considerably reduce the computational cost as well as the required computer memory, thus they have been widely adopted in many commercial CFD software packages, for instance, FLUENT and CFX. Zero-equation mixing length model [69], two-equation $k-\varepsilon$ [70], $k-\omega$ [71] and Reynolds stress models are the most common RANS-based turbulent models. Alternatively, large eddy

simulation (LES) is another approach for high Reynolds number turbulence modelling, in which the mean flow and largest eddies are computed by the time-dependent flow equations with the small scale eddies being modelled. Since the largest eddies in the turbulent have strong interactions with the mean flow and contain most of the energy, LES holds the merit of resolving the main effects of turbulence. However, LES is extremely time consuming and computationally expensive. Since the two-equation $k-\varepsilon$ model is a relatively accurate and economic turbulence model for most practical engineering flow calculations and has been widely validated, a detailed description of the $k-\varepsilon$ turbulence model is given here.

It is argued that the effects of Reynolds stresses on the mean turbulent flow are analogous to those of viscous stresses. Based on this presumption, Boussinesq in 1877 introduced an expression that related the Reynolds stresses with the mean velocity gradients. The corresponding equation in tensor notation is

$$\tau_{ij} = -\rho\overline{u_i' u_j'} = \mu_t\left(\frac{\partial\overline{u_i}}{\partial x_j} + \frac{\partial\overline{u_j}}{\partial x_i}\right) \tag{2.12}$$

where τ_{ij} $(=-\rho\overline{u_i' u_j'})$ is the Reynolds shear stress, $\overline{u_i}$, $\overline{u_j}$ are the time averaged velocity components in x_i , x_j ($i=1$, 2, 3; $j=1$, 2, 3) directions and μ_t is the dynamic eddy viscosity that is assumed to be an isotropic scalar quantity. Two-equation $k-\varepsilon$ turbulence models use the Boussinesq hypothesis and the eddy viscosity μ_t is computed as a function of the turbulent kinetic energy k ($k=\frac{1}{2}\left(\overline{u'^2}+\overline{v'^2}+\overline{w'^2}\right)$) and the turbulence dissipation rate (ε). k and ε are solved separately by two additional transport equations. The standard $k-\varepsilon$ turbulence model is given below [70]:

$$\mu_t = \rho C_\mu \frac{k^2}{\varepsilon} \tag{2.13}$$

$$\frac{\partial(k\rho)}{\partial t} + \frac{\partial\left(\overline{u_i} k\rho\right)}{\partial x_i} = \frac{\partial}{\partial x_i}\left(\frac{\mu_t}{\sigma_k}\frac{\partial k}{\partial x_i}\right) + \underbrace{\mu_t\left(\frac{\partial \overline{u_i}}{\partial x_j} + \frac{\partial \overline{u_j}}{\partial x_i}\right)\frac{\partial \overline{u_i}}{\partial x_j}}_{P} - \rho\varepsilon \tag{2.14}$$

$$\underbrace{\frac{\partial(\varepsilon\rho)}{\partial t}}_{\text{rate of change}} + \underbrace{\frac{\partial\left(\overline{u_i}\varepsilon\rho\right)}{\partial x_i}}_{\text{convection}} = \underbrace{\frac{\partial}{\partial x_i}\left(\frac{\mu_t}{\sigma_\varepsilon}\frac{\partial \varepsilon}{\partial x_i}\right)}_{\text{diffusion}} + \underbrace{C_{1\varepsilon}\frac{\varepsilon}{k}P - C_{2\varepsilon}\rho\frac{\varepsilon^2}{k}}_{\text{generation}-\text{destruction}} \tag{2.15}$$

where C_μ, σ_k, σ_ε, $C_{1\varepsilon}$ and $C_{2\varepsilon}$ are empirical constants and are given values in Table 2.1.

C_μ	$C_{1\varepsilon}$	$C_{2\varepsilon}$	σ_k	σ_ε
0.09	1.45	1.92	1.00	1.30

Table 2.1: Values of the constants in the $k-\varepsilon$ turbulence model [70]

2.1.4 Free Surface Modelling

The free surface is the interface between two immiscible fluids: water and air and it is one of most important topics in open channel flow. The free surface is not fixed and it may vary both spatially and temporally. Thus free surface flow is difficult to deal with for CFD modelling.

In some cases, a 'rigid lid' (solid boundary) approximation is used and free surface is treated as an imaginary frictionless horizontal plane on which the velocity perpendicular to the plane is zero and the velocity tangential to the plane is non-zero. This approach can save computational efforts but is only valid under the hypothesis

that there are no significant variations in water free surface. Therefore, whenever a detailed description of the free surface is important, a numerical model of free surface is best utilized. The numerical methods for free surface modelling can be classified into two categories: moving-grid methods and fix-grid methods [72]. In moving-grid methods, the free surface is designated as the boundary of a surface fitted grid and the computational grid is permitted to move with the free surface. The advantage of this method is that it can precisely compute free surfaces, but it can be very difficult and time-consuming to be employed for dealing with the complex 3D free surface geometry. Instead, the fix-grid methods use the fixed stationary computational grid that covers both gas and liquid regions, and it can be further segregated into two groups: surface-capturing method and surface-tracking method.

In the surface-tracking method, the position of the free surface is explicitly distinguished and tracked by the pre-defined markers that can be a scalar function like the volume fraction function in the Volume of Fluid (VOF) approach. The surface-tracking method allows the governing equations only in the liquid and the free surface grid cells to be solved [73]. Many approaches have been developed based on the surface-tracking method such as the front-tracking-method [74], the marker-and-cell (MAC) method [75] and the volume of fluid (VOF) method [76]. Surface-capturing methods, on the other hand, avoid the need for the complicated free surface tracking process by regarding the free surface as a discontinuity in the density field and being captured automatically in the computation of gas-liquid flow. In surface-capturing method, the governing equations are solved simultaneously for both gas and liquid regions. The artificial compressibility approach [77] is one variant of the surface-capturing methods. There are also numerous other methods and

Floryan and Rasmussen have given an overview on the numerical techniques for free surface modelling in their paper [78].

The Volume of fluid (VOF) method is robust and powerful. Thus, it has gained extensive engineering applications. VOF is adopted in the modelling of free surfaces in this study and a detailed description of the method used in the commercial CFD code FLUENT is given here [79].

The VOF method considers two or more fluids (or phases) that are not interpenetrating. Each phase is represented by its own volume fraction in every grid cell (control volume) and the volume fractions of all phases in one control volume sum to unity. The position of the interface can be identified according to the volume fraction in each cell. For simplicity, the case of only two phases (water and air) is considered in the following description, which is the real situation for open-channel flow simulation. In VOF, 'Air' is defined as the primary phase and its volume fraction can be denoted as α_1. Correspondingly, 'Water' is defined as the secondary phase and its volume fraction can be denoted as α_2. In each control volume, there exist three possible conditions for water volume fraction α_2:

$\alpha_2 = 0$: the cell is empty (of water but full of air)

$\alpha_2 = 1$: the cell is full (of water but empty of air)

$0 < \alpha_2 < 1$ the cell contains the interface between air and water

A continuity equation (2.16) is provided to calculate the volume fraction α_2

$$\frac{\partial \alpha_2}{\partial t} + u_j \frac{\partial \alpha_2}{\partial x_j} = 0 \tag{2.16}$$

The volume fraction of air α_1 then can be obtained from equation (2.17)

$$\alpha_1 = 1 - \alpha_2 \tag{2.17}$$

Therefore, the interface can be tracked in each control volume according to the volume fraction of air and water.

In VOF, fluid properties like density ρ and dynamic viscosity μ in the governing equations are determined by α_1 and α_2 in each control volume and calculated by equation (2.18) and (2.19) respectively.

$$\rho = \alpha_1 \rho_1 + \alpha_2 \rho_2 \tag{2.18}$$

$$\mu = \alpha_1 \mu_1 + \alpha_2 \mu_2 \tag{2.19}$$

where μ_1 and ρ_1 are the dynamic viscosity and density of air. μ_2 and ρ_2 are the dynamic viscosity and density of water.

A single momentum equation (2.20) is solved in the VOF method and the resulting velocity field is shared among the phases. The equation (2.20) is dependent on the volume fractions of all phases through ρ and μ.

$$\rho \frac{\partial u_i}{\partial t} + \rho \frac{\partial \left(u_i u_j \right)}{\partial x_j} = -\frac{\partial p}{\partial x_i} + \frac{\partial}{\partial x_j} \mu \left(\frac{\partial u_i}{\partial x_j} + \frac{\partial u_j}{\partial x_i} \right) + \rho g_i + F_i \tag{2.20}$$

where ρg_i and F_i are the gravitational body force and external body force respectively. F_i also contains other model-dependent source terms, such as porous medium and user-defined sources in FLUENT. Similarly, if the $k - \varepsilon$ equation is used for turbulent flow modelling, a single set of transportation equations is solved and the variables k and ε are shared by both of the water and air phases throughout the field.

2.1.5 The Actuator Disk Theory for Turbine Simulation

The actuator disk theory was formulated by Froude [80] and is the fundamental theoretical basis for screw, propeller and wind turbine study. The actuator disk has been widely used for wind turbine simulation [81-84] and currently-used advanced numerical methods have been developed also based on this theory, like Blade Element Momentum (BEM) by Glauert [85].

In the actuator disk theory, a streamtube enclosing a turbine rotor is considered (see Figure 2.5). The rotor is simulated as a semi-permeable disc with the same diameter and is placed perpendicular to the direction of flow. The load on the real rotor is represented by a uniform pressure jump created by flow passing though this semi-permeable disc. The inflow and outflow boundaries of the streamtube are taken far from the actuator disk, where the pressure has recovered to the undisturbed atmospheric pressure p_∞, and the flow velocity is regarded as uniform at each cross section of tube. The mathematical expressions of an actuator disk theory applied to wind turbines are stated as follows.

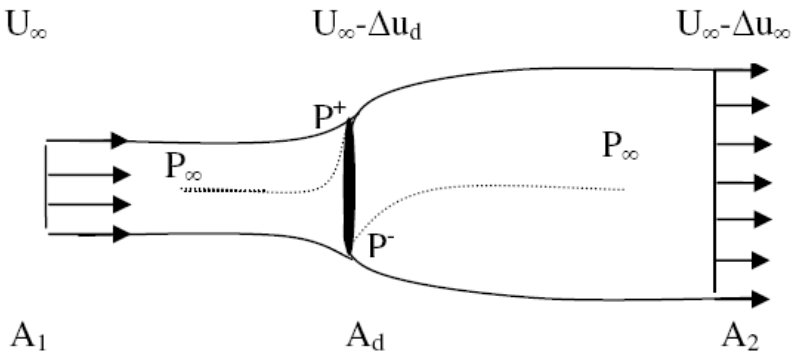

Figure 2.5: The streamtube enclosing a turbine rotor in the actuator disk theory [86]

The mass conservation over the streamtube can be expressed as:

$$\dot{m} = \rho A_1 U_\infty = \rho A_2 U_2 = \rho A_d U_d \tag{2.21}$$

where A_1 and A_2 are the areas of upstream and downstream cross sections of the streamtube. A_d is the area of the actuator disk. U_∞ is the free stream velocity at the inflow boundary and U_2 is the far wake velocity at the outflow boundary. U_d is the flow velocity at the actuator disk.

Using the momentum conservation, the drag force D on the rotor disk can be written as:

$$D = \dot{m}U_\infty - \dot{m}U_2 = \rho A_1 U_\infty^2 - \rho A_2 U_2^2 \tag{2.22}$$

By applying Bernoulli's equation on both upstream and downstream disk, the pressure difference $\left(p^+ - p^-\right)$ across the disk can be expressed in equation (2.23).

$$p^+ - p^- = \frac{1}{2}\rho\left(U_\infty^2 - U_2^2\right) \tag{2.23}$$

Therefore, the drag force D can become

$$D = \frac{1}{2}\rho A_d \left(U_\infty^2 - U_2^2\right) = \rho A_d \left(U_\infty - \frac{\Delta u_\infty}{2}\right) \cdot \Delta u_\infty \tag{2.24}$$

where $U_2 = U_\infty - \Delta u_\infty$ and Δu_∞ is the velocity deficit in the turbine wake at the outflow boundary of the streamtube.

Also, the equation (2.22) for the drag force D can become

$$D = \dot{m}\left(U_\infty\right) - \dot{m}\left(U_\infty - \Delta u_\infty\right) = \rho A_d \left(U_\infty - \Delta u_d\right) \cdot \Delta u_\infty \tag{2.25}$$

where Δu_d represents the decrease of velocity in the plane of the rotor because of energy extraction. Comparing equation (2.24) and (2.25) given

$$\Delta u_d = \frac{\Delta u_\infty}{2} = \frac{\left(U_\infty - U_2\right)}{2} \tag{2.26}$$

or

$$U_d = \frac{(U_\infty + U_2)}{2} \tag{2.27}$$

Equation (2.27) is widely known as Froude's theorem that the velocity at the actuator disk is the mean value of freestream and far wake velocities.

The total power available in the flow can be written as

$$P_{total} = \frac{1}{2}\rho U_\infty^3 A \tag{2.28}$$

The power extracted by the turbine rotor can be written as

$$P_{extract} = D \times U_d = \frac{1}{2}\rho A_d U_d \left(U_\infty^2 - U_2^2\right) \tag{2.29}$$

After several transformations by using the equations, the equation (2.29) can be rewritten as equation (2.30)

$$P_{extract} = \rho A_d \left(U_\infty - \Delta u_d\right)^2 \cdot 2\Delta u_d \tag{2.30}$$

Thus the maximum extractable energy by the turbine rotor can be found by equation (2.31).

$$\frac{\partial P_{extract}}{\partial(\Delta u_d)} = 0 \longrightarrow \Delta u_d = \frac{U_\infty}{3} \tag{2.31}$$

The maximum power coefficient (Betz limit) can be decided as

$$\frac{P_{e\max}}{P_{total}} = \frac{\frac{8}{27}\rho A_d U_\infty^3}{\frac{1}{2}\rho A_d U_\infty^3} = \frac{16}{27} \approx 0.593 \tag{2.32}$$

The non-dimensional power coefficient C_P defined by equation (2.33) and drag coefficient C_D defined by equation (2.34) are introduced to represent the efficiency of power output and the drag force for the sake of convenience.

$$C_P = \frac{P_{extract}}{P_{total}} \tag{2.33}$$

$$C_D = \frac{D}{\frac{1}{2}\rho A_d U_\infty^2} \tag{2.34}$$

An interference factor a is also introduced to measure the energy extracted from the flow and is decided by equation (2.35)

$$a = \frac{\Delta u_d}{U_\infty} \tag{2.35}$$

The power coefficient and drag coefficient can, therefore, be represented by a as

$$C_P = 4a(1-a)^2 \tag{2.36}$$

$$C_D = 4a(1-a) \tag{2.37}$$

However, the rotor geometry, which may play a crucial role in turbine performance, is not considered in the actuator disk theory.

Although this concept gets by far the widest application in understanding of wind turbine aerodynamics, it is valid for any fluid and has been adopted for marine propeller and tidal current turbine simulation [87, 88], subject to the conditions relating to boundaries.

2.1.6 Numerical Methods

Discretization Methods

After establishing a set of mathematical equations to describe the physical problem, a discretization method needs to be chosen to seek the numerical solutions. Discretization is 'a method of approximating the differential equations by a system of algebraic equations for the variables at some set of discrete locations in space and

time' [89]. There are three common discretization approaches: finite difference (FD), finite volume (FV) and finite element (FE). A description about FV method has been given in section 2.1.1 of this chapter. It is argued that if the computational grid is very fine, there is no difference for the final solutions using whatever discretization method.

Numerical Interpolation Schemes

In the finite volume method (FV), the values of flow variables at the surface of one control volume need to be obtained in terms of the centroid values of all its neighbouring cells that share the same cell face by using suitable interpolation scheme. There are several schemes available which are designed for the purpose of improving solution accuracy in different problems. The second-order upwind scheme is chosen for the discretization of all the flow variables except the pressure in the present study in order to achieve accurate computational results and this scheme is explained in details in Appendix A.

The Pressure Staggering Option (PRESTO) is one of pressure interpolation schemes and it is identical in spirit to the staggered-grid schemes described by Patankar (1980) [90]. The PRESTO approach is recommended for the simulation of flow fields in which the steep pressure gradients are expected [79]. Hence, the PRESTO approach has been used for pressure interpolation in this research.

Properties of Numerical Solution Methods

The numerical method must have certain properties based on which the numerical solutions can be judged as being reasonable. Some most important properties have

been given a brief introduction below, which are taken from the summaries of Ferziger and Peric (1996) [89].

(a) Consistency

The discretization should become exact as the grid spacing tends to zero. The difference between the discretized equation and the exact one is called the truncation error. For a method to be consistent, the truncation error must become zero when the grid spacing $\Delta x_i \to 0$ and/or time step $\Delta t \to 0$. Truncation error is usually proportional to a power of the grid spacing Δx_i and/or the time step Δt. If the most important term is proportional to $(\Delta x)^n$ or $(\Delta t)^n$, we call the method an n th-order approximation; $n > 0$ is required for consistency.

(b) Stability

A numerical solution method is said to be stable if it does not magnify the errors that appear in the course of numerical solution process. For temporal problems, stability guarantees that the method produces a bounded solution whenever the solution of the exact equation is bounded. For iterative methods, a stable method is one that does not diverge.

(c) Convergence

A numerical method is said to be convergent if the solution of the discretized equations tend to the exact solution of the differential equation as the grid spacing tends to zero. A consistent scheme is useless unless the solution method converges. For non-linear problems, the stability and convergence of a method are difficult to demonstrate. Therefore convergence is usually checked using numerical experiments, i.e. repeating the calculation on a series of successively refined grids. If the method is stable and if all approximations used in the discretization process are consistent, we

usually find that the solution does converge to a grid-independent solution. For sufficiently small grid sizes, the rate of convergence is governed by the order of principal truncation error component.

(d) Conservation

Since the equations to be solved are conservation laws, the numerical scheme should also – on both a local and a global basis – respect these laws. This means that, at steady state and in the absence of sources, the amount of a conserved quantity leaving a closed volume is equal to the amount entering that volume. If the strong conservation form of equations and a finite volume method are used, this is guaranteed for each individual control volume and for the solution domain as a whole. Conservative schemes are preferred since it imposes a constraint on the solution error.

(e) Boundedness

Numerical solutions should lie within proper bounds. Physically non-negative quantities (like density, kinetic energy of turbulence) must always be positive; other quantities, such as concentration, must lie between 0% and 100%. In the absence of sources, some equations (e.g. the heat equation for the temperature when no heat sources are present) require that the minimum and maximum values of the variable be found on the boundaries of the domain. These conditions should be inherited by the numerical approximation.

2.2 Problem-Solving Steps in FLUENT

FLUENT is a state of the art computer software for CFD analysis based on the finite volume method and its applications have been over almost the entire fluid

dynamics spectrum. FLUENT has been used for tidal energy extraction simulation in this study.

The basic procedural steps for establishing a simulation case in FLUENT are briefly introduced in order to aid the reader in understanding the following simulations that are to be discussed.

1. Create the computational domain and build the grid in GAMBIT, the preprocessor from FLUENT.
2. Import the 2D or 3D grid into FLUENT.
3. Check the grid.
4. Select the type of solver formulations.
5. Choose the set of equations to be solved according to the physical phenomena to be simulated, i.e. viscous or inviscous.
6. Define the material properties.
7. Set up phases.
8. Define the boundary conditions for the computational domain.
9. Adjust the solution control parameters (discretisation schemes for the flow variables)
10. Initialize the flow field and patch the initial value for a flow variable in the domain.
11. Start calculation until convergence solutions are achieved.
12. Visualize and plot the results.
13. Adapt the grid and check the grid-independence of the results.

2.3 2D Modelling of Energy Extraction from Tidal Currents

In order to easily make comparisons with the experimental validations, a laboratory scale water flume is simulated in FLUENT. The tidal extraction device is modelled as an actuator disk by using a porous media model, which can produce the desirable pressure drop due to the kinetic energy change of water across the disk. Although it is expected various devices may have the differing impacts on local flows because of their superficial differences, it is reasonable to believe there are generic impacts resulting from energy extraction from the water column and the resulting flow distortion, which are those to be identified in this simulation. In a previous study [88], the free surface was simplified as a 'rigid-lid' based on the assumptions that free surface has no variation and thus it has no effects on the flow field, which are not true in the real situation especially in consideration of the effects of a tidal 'farm'. In this research, a more realistic simulation is established in which the free surface is allowed to deform freely via the VOF method.

2.3.1 2D Numerical Model

The relevant procedures of a 2D numerical model for simulating energy extraction from tidal currents are described step by step as follows:

1. Geometry of computational domain and grid setup

   A 10 000 mm long and 1000 mm deep rectangular domain was defined as the water zone ($x = \text{longitude}$, $y = \text{latitude}$), the latter dimension allowing another 1000 mm deep of air space above the free surface. The water inlet was set at

$x = -5000$ mm and outlet was set at $x = 5000$ mm. The computational domain was meshed in GAMBIT using a structured grid with total 40 000 quadrilateral cells. A region of height 500 mm and thickness 5 mm was separated from the water zone and its centre was located at $y = -500$ mm, so that it occupied the half of water depth which had a similar ratio to that of expected full scale tidal current turbines [17, 91]. This region was defined as an actuator disk in the later step of defining boundary conditions. The grid was refined around the separated zone, where a steep pressure gradient was anticipated. The computational domain is illustrated in Figure 2.6 and the structured grid is demonstrated in Figure 2.7.

2. Unit

   S.I. units were selected.

3. Physical model selection

   The standard $k - \varepsilon$ turbulence model was selected to predict the turbulent wake behind the actuator disk. The unsteady implicit, one kind of the VOF schemes, was chosen to capture the variation of free surface shape. This method doesn't require a distinct inflow boundary for each fluid phase, which offers the convenience in setting up the model. An open channel flow option was enabled in conjunction with the VOF scheme and this option allowed using the open channel boundary condition for open channel flow simulation.

4. Setting the physical constants

The flow was assumed to be incompressible. The water density was 998.2 kgm^{-3} and air density of 1.225 kg m^{-3}. The corresponding dynamic viscosities were 1.003×10^{-3} kg m^{-1} s^{-1} and 1.7894 $\times 10^{-5}$ kg m^{-1} s^{-1} for water and air respectively.

5. Defining phases

Air is selected as the primary phase and water was selected as the secondary phase. In general, there are no requirements for specifying which fluid as the secondary phase. But in a later step, an initial volume fraction of 1 for water will be patched in the lower half portion of the computational domain. Therefore, water was set as the secondary phase in this simulation with the consideration of the ease of problem setup [79].

6. Defining the boundary conditions

(1)Wall boundary conditions

The bottom of water flume was treated as a 'no-slip' wall, on which all the velocity components (u and v) were set to zero.

(2) Inlet boundary condition

The mass flow inlet condition was selected in accordance with the requirements for the open channel simulation in FLUENT. The free surface level was set at $y = 0$ and the channel bottom level was set at $y = -1000$ mm. The mass flow rate $\dot{m}$ was specified as 1270 kg s^{-1} for the water phase, which was corresponding to a uniform freestream velocity $U_\infty = 1.27$ m s^{-1}. Consequently, the flow is subcritical with Froude number of 0.4. A small value of the mass flow rate was specified for the air phase, which assumed that there was little moving air entering the domain. A low turbulence intensity I =1%

was used for the inlet condition, in order to exclude the effect of turbulence, which was to be particularly examined later.

(3) Outlet boundary condition

The gauge pressure at the outlet boundary was specified by using the user-defined function (UDF) provided in FLUENT and was attached as Appendix B behind the thesis. The channel bottom level was set at $y = -1000$ mm and the turbulence intensity was 1%.

(4) Symmetry boundary condition (top boundary)

The top plane of the computational domain was defined as a symmetry plane that could be used to simulate a slip wall and there were a zero flux of all quantities across a symmetry plane. This option was decided according to the recommendation from FLUENT and avoided the risk of getting divergent solutions.

(5) The porous zone

A small number of interior cells, which were separated from the whole grid and located in the water phase, were defined as a semi-permeable actuator disk approximated by the means of the porous media model in FLUENT. The porous media model is an added momentum sink in the governing momentum equations and is detailed in Appendix C. The parameters for the porous zone used in the 2D model are given below.

Direction vector 1: X(1), Y(0) (Flow direction)

Direction vector 2: X(0), Y(1)

Viscous resistance ($1/\alpha_{ij}$):	Inertial resistance ($C_{2i,j}$):
Direction 1 (1 m^{-2}): 100000	Direction 1 (1 m^{-1}): 2667
Direction 2 (1 m^{-2}): 100000	Direction 2 (1 m^{-1}): 100000

7. Setting the body forces

Gravitational effects were accounted by setting a body force per unit mass of $g = -9.8067$ m s^{-2} in the y-direction.

For VOF calculations, the density of air needed to be specified as the operating density in this step, which excluded the buildup of hydrostatic pressure within the lightest phase and was essential for the smooth and rapid convergence.

8. Solving the problem

(1) Adjusting the solution control parameters

The second-order scheme was selected for the discretization of all flow variables except for the pressure and volume fraction, with the aim to improve the accuracy of final solutions. The PRESTO scheme was adopted for pressure discretization because it is a suitable method for the problem in which the porous media is involved. The Quadratic Upwind Interpolation for Convective Kinematics (QUICK) discretization scheme was used for the volume fraction equations and it can improve the sharpness of the interface between phases [79]. Under-relaxation factors in FLUENT are used to control the update of computed variables at each iteration. Although the default of under-relaxation factors were near optimal for most of cases, smaller under-relaxation factors for pressure, momentum, k and ε were utilized in the present model, which were 0.3, 0.5,

0.5 and 0.5 respectively, in order to avoid the unstable and diverge behaviour during the iteration calculations.

The Semi-Implicit Method for Pressure-Linked Equations (SIMPLE) algorithm was chosen for pressure-velocity coupling, which was used to derive an equation for the pressure from the discretized continuity and momentum equations.

(2) Enabling the residual monitoring during iteration

A FLUENT calculation is performed, when all of the discretized transport equations are balanced at each cell in the computation domain. The imbalances for every flow variable at each cell are termed residuals. On an infinite precision computer, the residuals for all variables should go to zero as the solution convergence. On an actual computer, when the residuals decay to some small values and stop changing, the solutions are assumed to be converged.

During the calculation in the present simulation, which used an iterative process, the convergence was monitored by plotting the scaled residuals for velocity components, pressure, turbulence kinetic energy and its dissipation rate. In addition, the mass flow rate at the outlet boundary and the value of static pressure at a point set up $1\,d$ (d is 500 mm, the characteristic length of actuator disk defined in 2D model) behind the actuator disk were also monitored, in order to judge properly the overall convergence of the model.

(3) Initializing the solution

The entire flow field was initialized firstly by using the values set for the inlet boundary condition. The initial water distribution was then determined by patching the water volume fraction of 1.0 and the water velocity 1.27 m s^{-1} in

the lower half of the rectangular computational domain. That is, the lower half of the computational domain was defined to be filled with water and the water speed was 1.27 m s^{-1}. The initial water distribution is showed in Figure 2.8.

(4) Starting calculation

The iteration calculations continued taking a time step of 0.001 s until the convergent solutions were attained.

(5) Saving the case and data files

The results were recorded and were analyzed using the graphic capability of FLUENT.

(6) Checking the grid independence of results

The grid was refined around the region of the actuator disk and the total cells reached 46 000. The calculations were resumed until the solutions reached convergence again. The results were examined and compared with the preliminary results. No significant changes were yielded. Thus, the results were deemed grid independent.

2.3.2 2D Results and Discussion

The variation in the free surface is observed by multi-phase plot in FLUENT and is showed in Figure 2.9. A significant surface drop behind the actuator disk appeared, which is in agreement with the theoretical predictions that the artificial energy extraction from tidal currents can result in substantial head drops across the energy extraction zone [48, 49]. However, the actuator disk is assumed across the entire cross-section of water flume and thus causes a relatively high blockage ratio in 2D

model. The variation of free surface is magnified in 2D results because of the presence of the actuator disk.

The streamwise velocity contour is displayed in Figure 2.10. The water flow downstream of actuator disk suffers a loss in momentum and thus results in a de-energized wake region, in which the water speed is greatly reduced. At the same time, there are notable velocity accelerations above and under the actuator disk. The normalized mean velocity deficit along the centreline of actuator disk defined by the equation $\frac{(U_\infty - U_c)}{U_\infty}$, in which U_∞ is the freestream velocity and U_c is the velocity on wake centreline, is shown in Figure 2.11. It is noticed that the upstream incoming velocity is significantly decreased by 21%, which is associated with the upstream water level being raised up because of the blockage effect. But the downstream mean velocity deficit is rapidly recovered over a short distance under the influence of appreciable free surface change.

In a real circumstance, the area of energy extraction could only be a small fraction of channel section. Therefore, the 3D simulation is important.

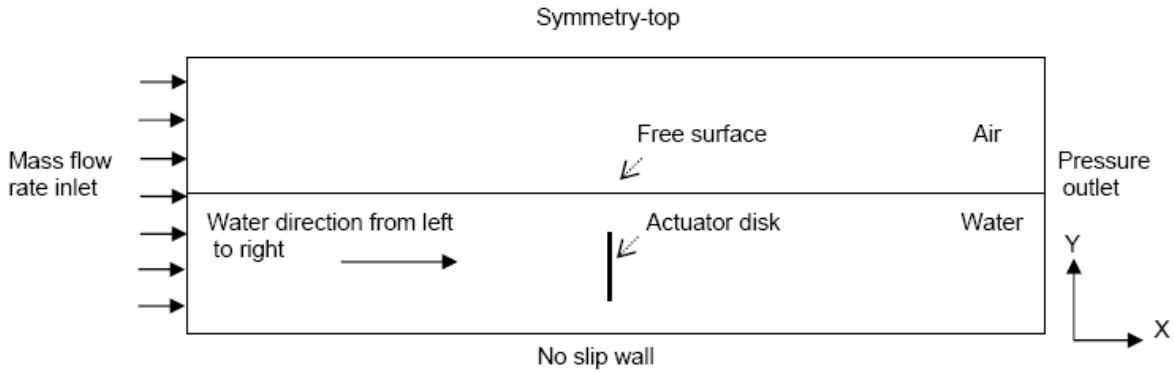

Figure 2.6: The computational domain and boundary conditions in 2D model

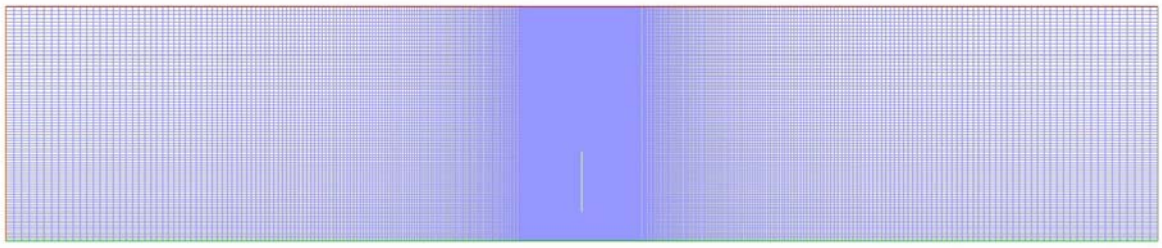

Figure 2.7: Structured grid in 2D model

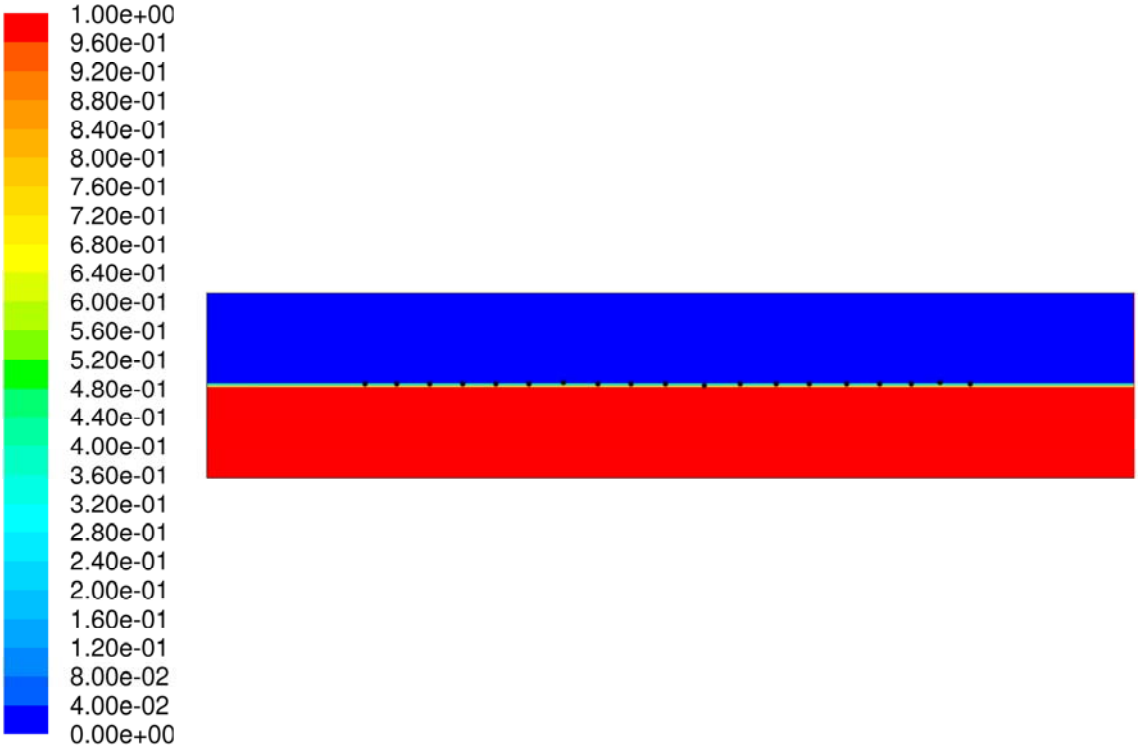

Figure 2.8: Initial water level
(····· highlight the air/water interface)

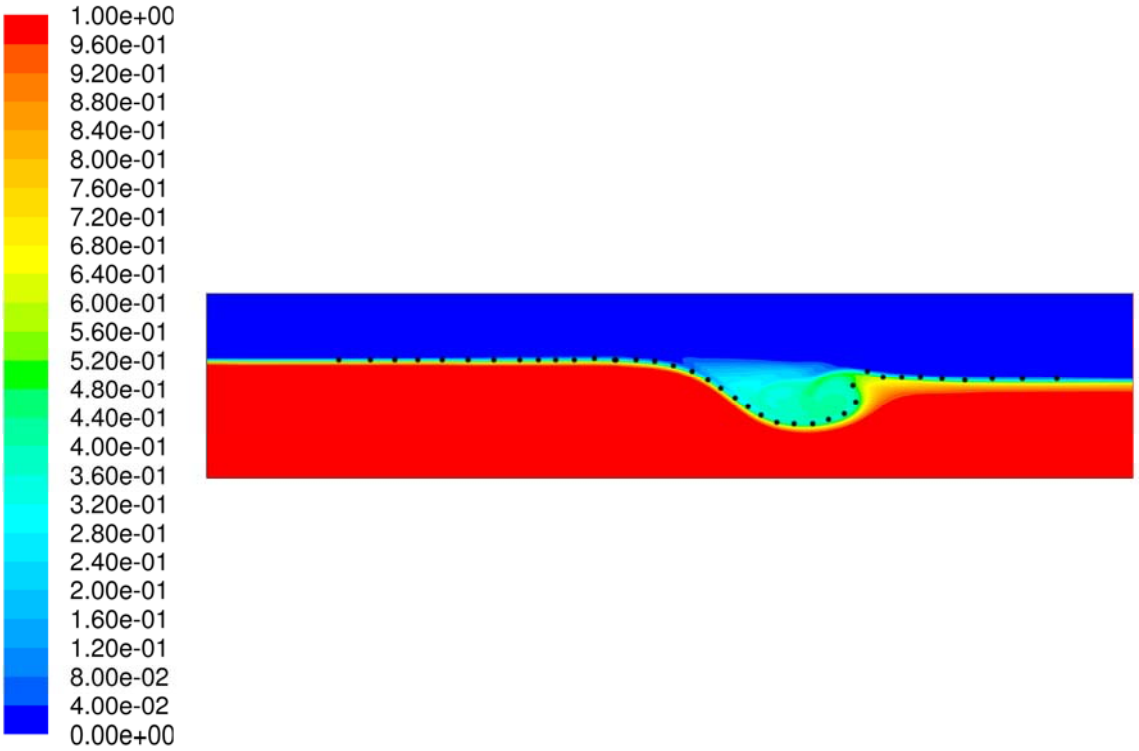

Figure 2.9: Free surface elevation in 2D model
(····· hightlight air/water interface)

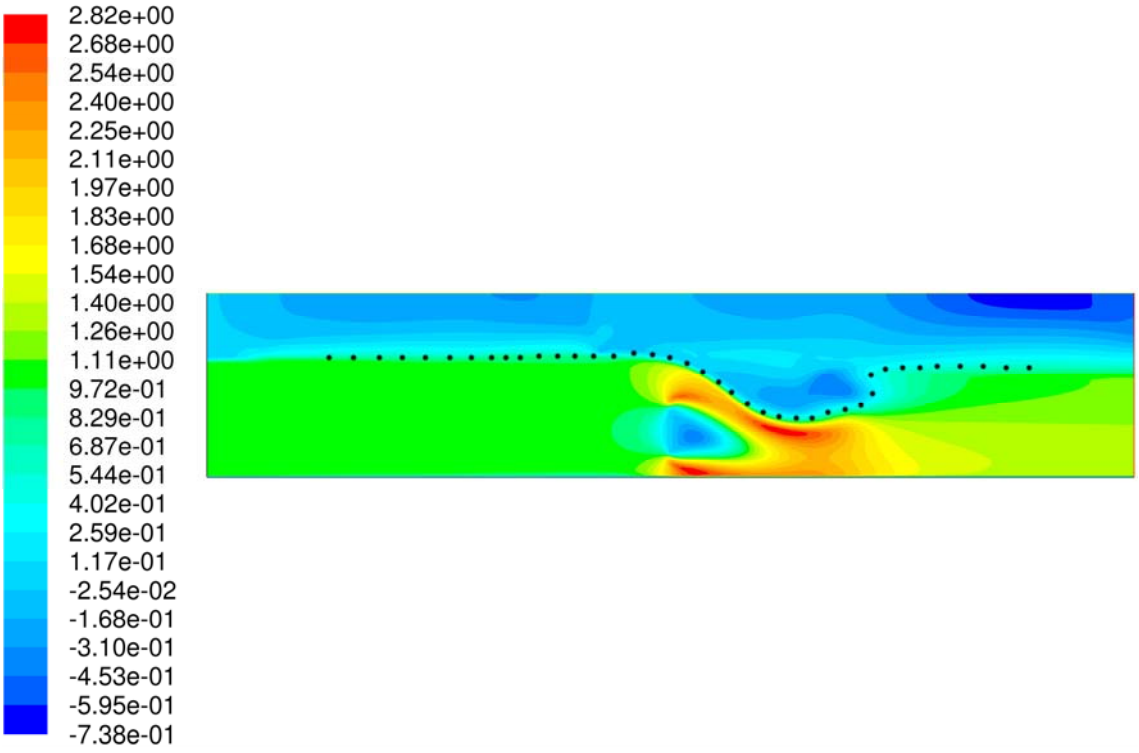

Figure 2.10: Contours of streamwise velocity, showing the de-energized wake behind the actuator disk (····· highlight air/water interface)

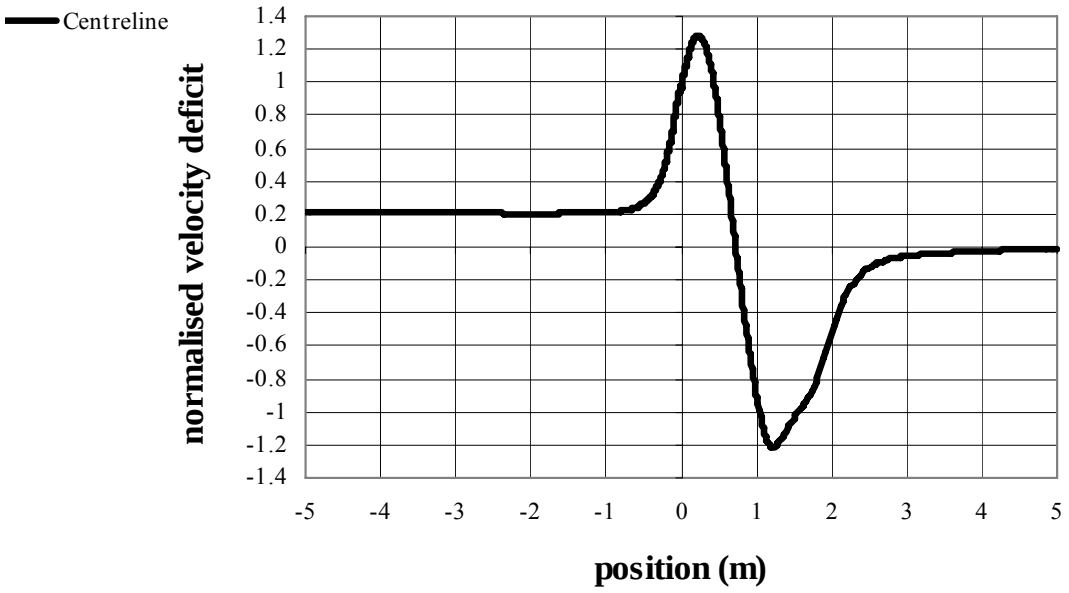

Figure 2.11: Normalized mean velocity deficit along the centreline of the actuator disk in 2D model

2.4 3D Modelling of Energy Extraction from Tidal Currents

2.4.1 3D Numerical Model

The 2D model was extended to three dimensions. A laboratory-scale water flume was constructed in GAMBIT and had overall dimensions 10 000 mm long by 1500 mm wide by 1500 mm high. The water was up to 1000 mm deep and there was another 500 mm air space above the free surface. The geometry of the water flume designed was a good compromise between the requirement of the total number of cells and the available computational resources. The water flume was meshed in GAMBIT using a structured grid which consisted of 96 000 hexahedral cells. A 500 mm × 500 mm rectangular region with thickness 5 mm was separated and was defined as an actuator disk which was modelled using the porous media in FLUENT. The blockage ratio (percentage of flow cross section occupied by the separated region) of the actuator disk in the water flume was about 17%. The grid was refined in the vicinity of free surface and the actuator disk, in order to improve the resolution. The actuator disk was set 3000 mm from the water inlet and thus the downstream wake behind it was allowed to be fully developed. Additionally, the distance from centre of disk to the free surface was 500 mm, which was half of the water depth. Scaling analysis of an open channel flow was described in Ref. [56] and scaling effects were considered in 3D model. The present 3D model is equivalent to a 20 m deep tidal channel with a current speed of 5.7 m s^{-1}. The main simulation conditions applied in the 3D model are tabulated in Table 2.2.

The computational domain for 3D models is illustrated in Figure 2.12 and the structured grid is showed in Figure 2.13. Other input parameters were all kept the

same as for the 2D model. But a larger time step 0.01 s was utilized in order to save the computation time. At the end of calculations, the scaled residuals for all the flow variables were below 1×10^{-4} and the solutions converged at each time step. Also, the values of other variables being monitored stopped changing with the iterations. Thus, the solutions reached convergence.

Characteristic length of the actuator disk d (mm)	Inertial resistance coefficient of the actuator disk $C_{2i,j}$ (1 m^{-1})	Free stream velocity U_{∞} (m s^{-1})	Free stream turbulence intensity I (%)	Submerged water depth h (mm)
500	2667	1.27	1	500

Table 2.2: Simulation conditions of 3D model

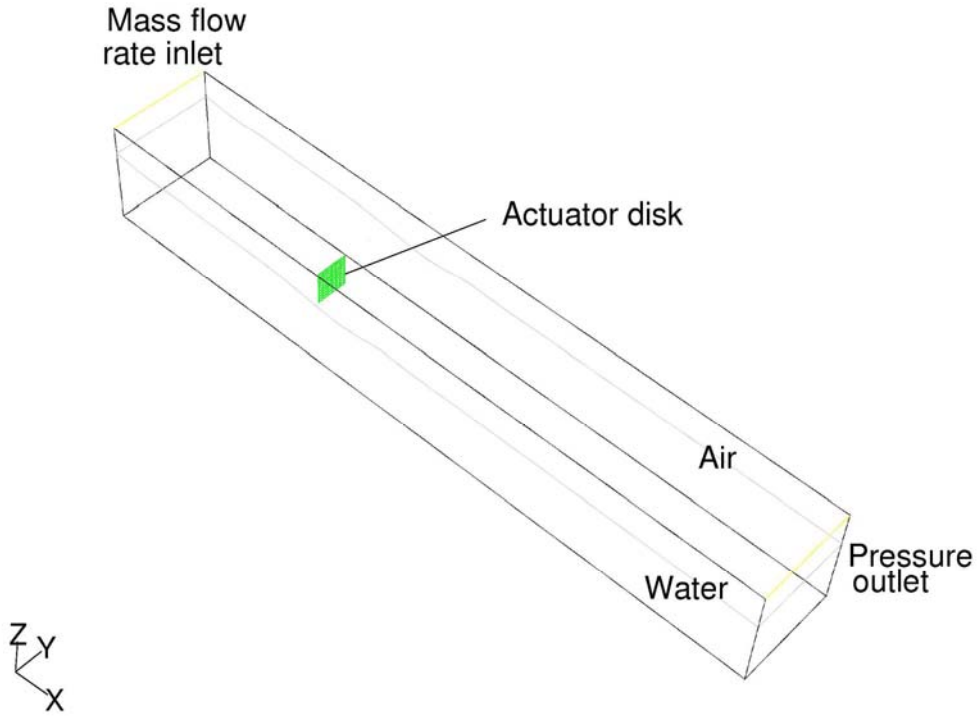

Figure 2.12: The computation domain and boundary conditions in 3D model

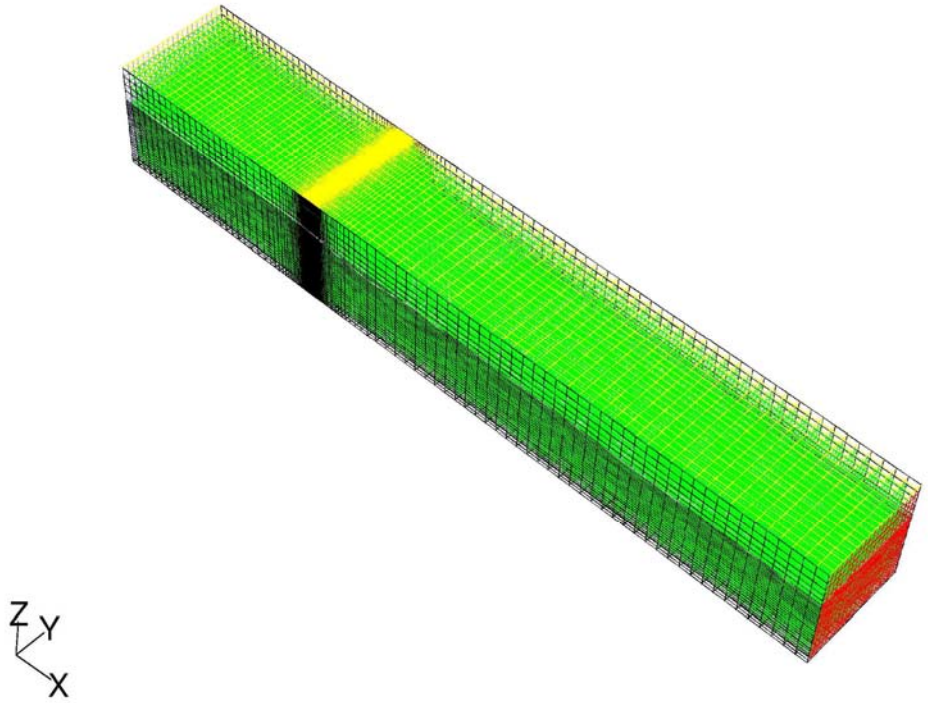

Figure 2.13: Structured grid in 3D model

2.4.2 3D Results and Discussion

The free surface is visualized as a three-dimensional surface elevation plot and the result is showed in Figure 2.14. A decrease in surface elevation immediately behind the actuator disk is further confirmed in the 3D model. The longitudinal free surface profile at the channel centreline is plotted in Figure 2.15 which is superficially similar to the experimental measurements conducted by Myers (2006) [92, 93]. In his experiment, both of the tank geometry and water speed are close to the model parameters in this study, except that an actual horizontal axis tidal turbine had been used in his test. The increase in the free surface elevation between downstream $3d$ and $4d$ (d is 500 mm, the characteristic length of actuator disk) is explained to be effected by the vertical wake expanding to reach the surface [92] based on an assumption that the vertical and lateral wake expansions are at the same rate.

The evolution of wake field behind the actuator disk can be clearly observed by the contours of streamwise velocity on the vertical and horizontal planes across the centre of the actuator disk, which is shown in Figure 2.16 (a-b) and Figure 2.17 (a-b) respectively. There is a clear velocity reduction due to energy losses in the wake. However, in the immediate neighbourhood of the disk, the water speed is rapidly accelerated due to the blockage effect caused by the presence of actuator disk. Moreover, the wake blockage effect can be significant in an open channel. Since the mean velocity in the wake is lower than the free stream velocity, the velocity outside the wake in a closed channel must be higher than the free stream in order to maintain continuity of volume flow rate. Therefore, the acceleration of water speed can remain along the downstream wake.

Profiles of the normalised streamwise velocity in the wake at various downstream locations are plotted on the vertical plane in Figure 2.18 and on the horizontal plane in Figure 2.19. In comparison with the horizontal velocity profiles, the vertical velocity profiles have less symmetric shapes. This may be attributed to the vertical expansion of the wake being strongly constrained by the presence of the free surface and the bottom wall. It has been observed that the bottom wall can interact with the wake and thus alter its re-energization process [94, 95]. It could become more complicated for a tidal current device, because not only the seabed but also the free water surface could influence its downstream wake. The velocity is slowly recovered to its initial value with the downstream location being further away from the energy extraction site. According to the study of wind turbine wakes, it is because in the far wake region, convection and turbulent diffusion determine the flow conditions. As a result, the wake velocity deficit will vanish because of turbulent diffusion of the wake far downstream [84].

The normalised mean velocity deficit along the centreline of the actuator disk is plotted in Figure 2.20. It shows the velocity ‘jump’ across the disk and the slow return to the freestream value with downstream distance. The upstream velocity is also slightly reduced by 5% because of the low blockage ratio in the 3D model.

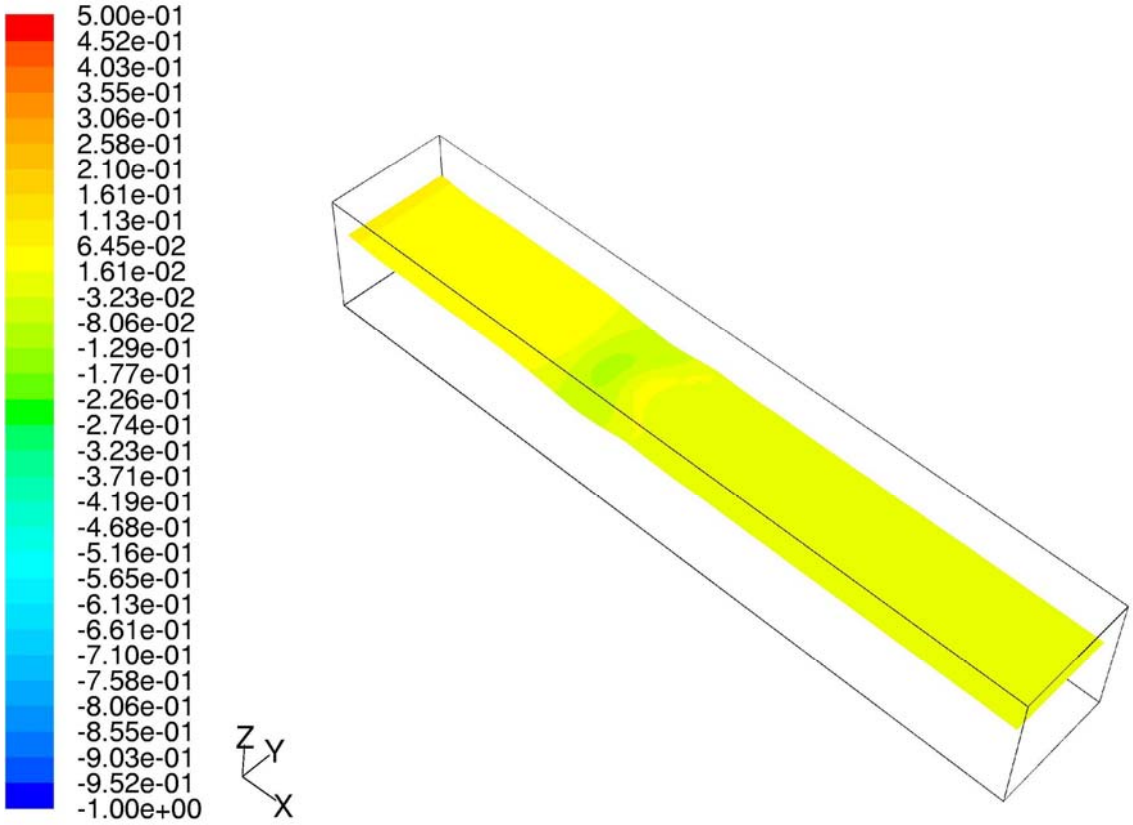

Figure 2.14: Contours of free surface elevation in 3D model

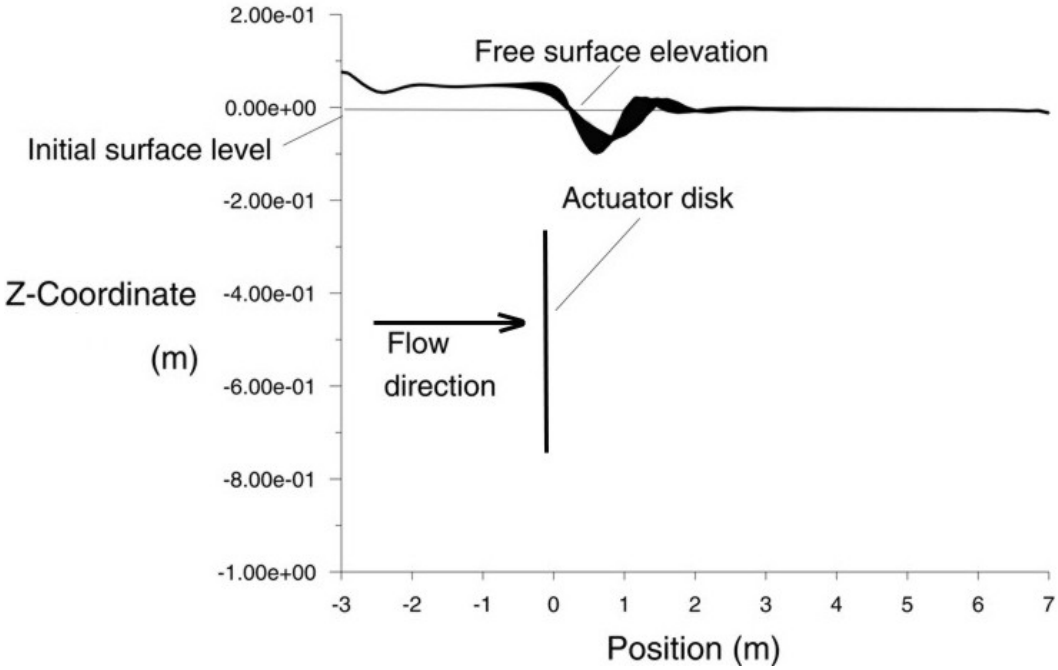

Figure 2.15: CFD longitudinal free surface profile at the channel centreline (plotted on the x - z central vertical plane)

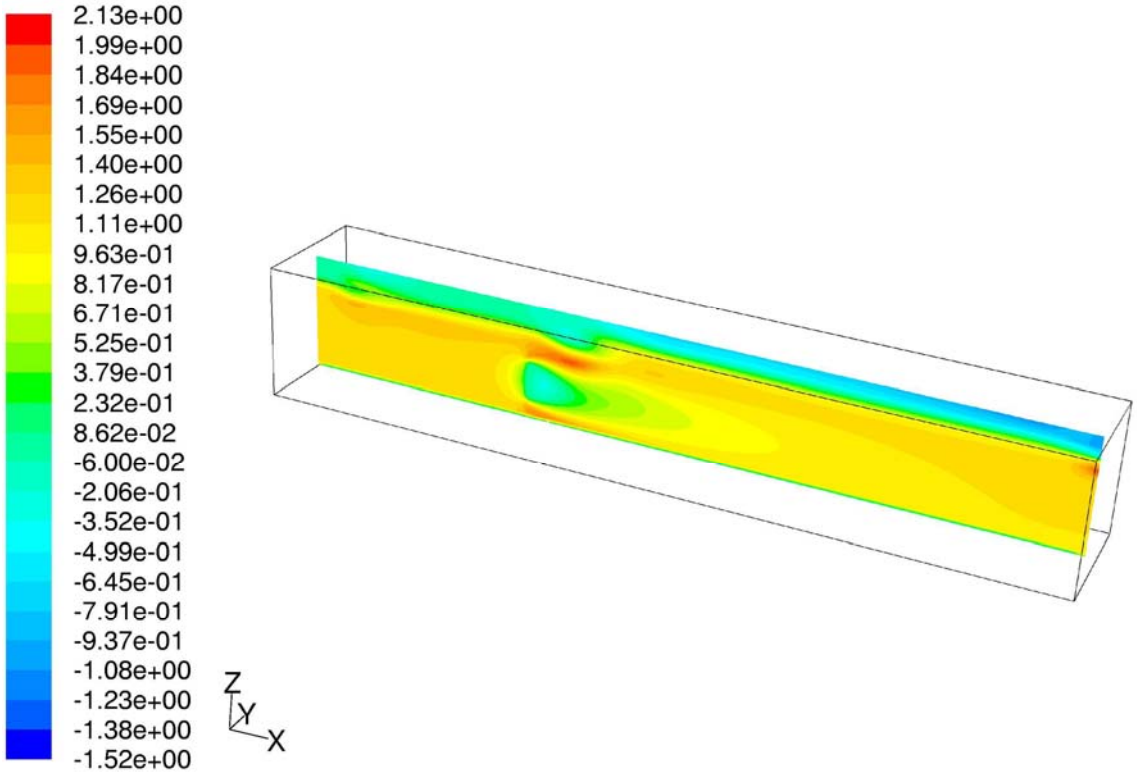

(a)

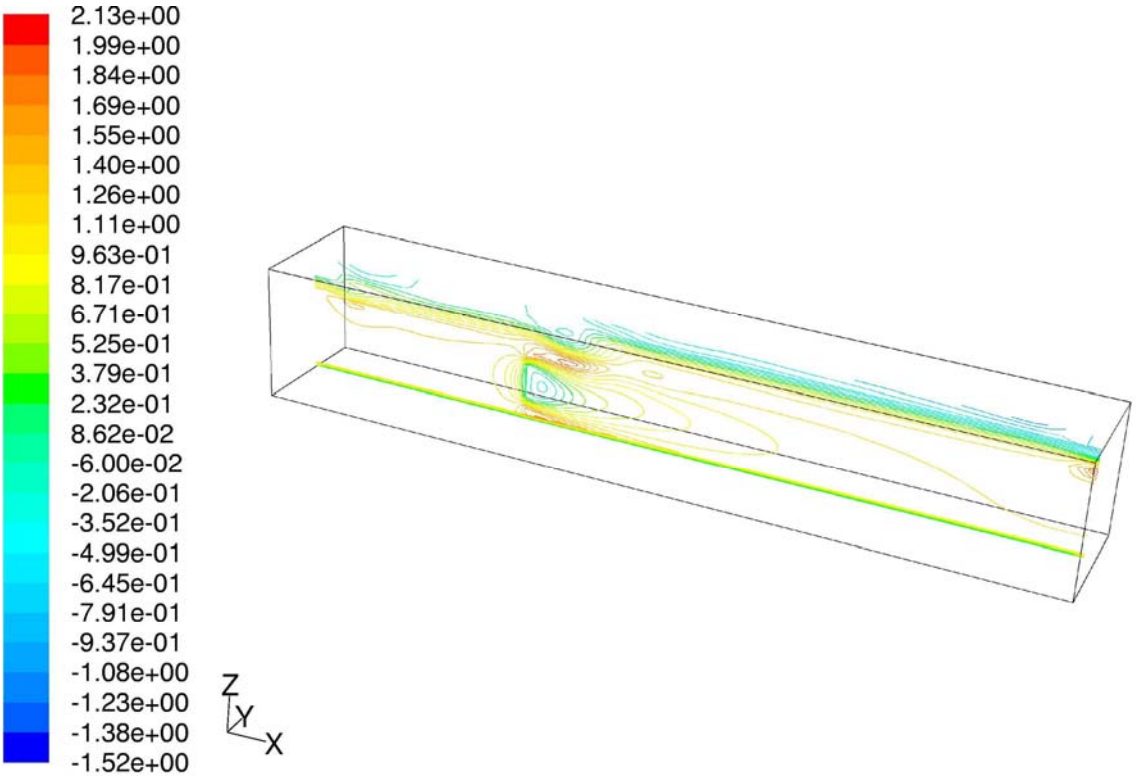

(b)

Figure 2.16: Contours of streamwise velocity on the x - z vertical plane -centre of actuator disk (y = 0 mm)

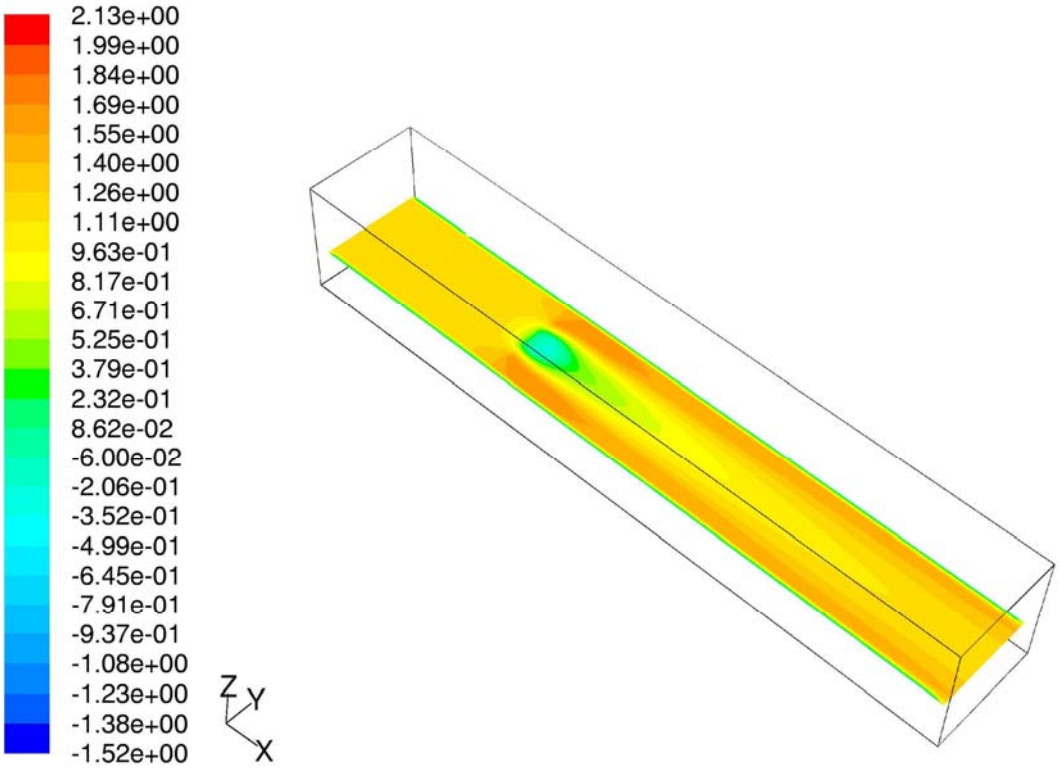

(a)

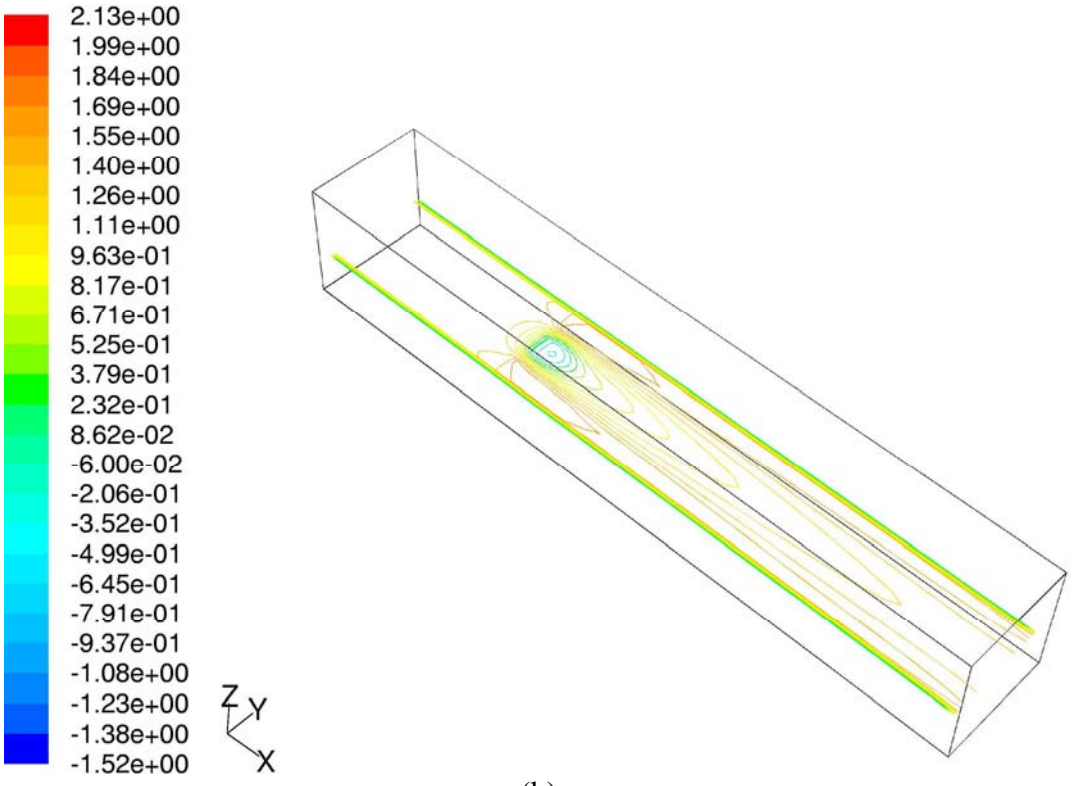

(b)

Figure 2.17: Contours of streamwise velocity on the x - y horizontal plane -centre of actuator disk (z = -500 mm)

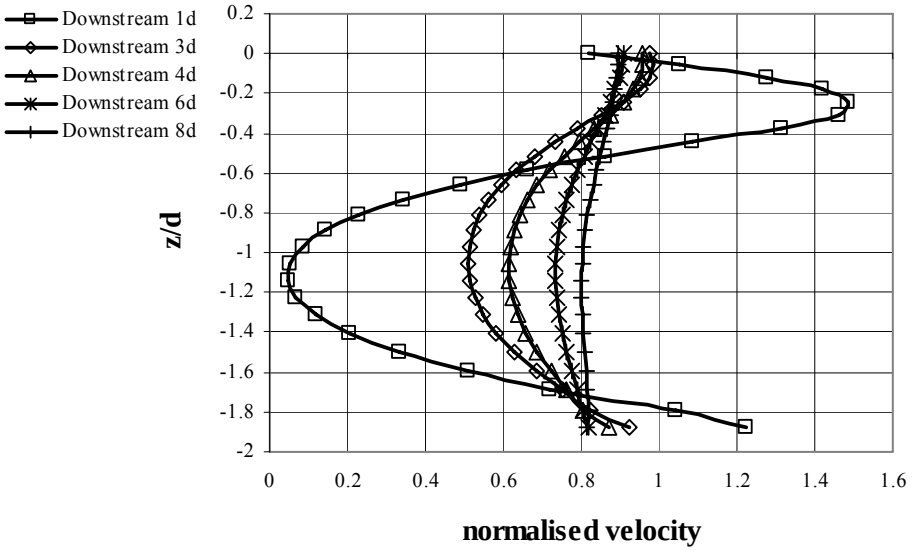

Figure 2.18: Profiles of normalised mean velocity at various downstream locations on the x - z central vertical plane

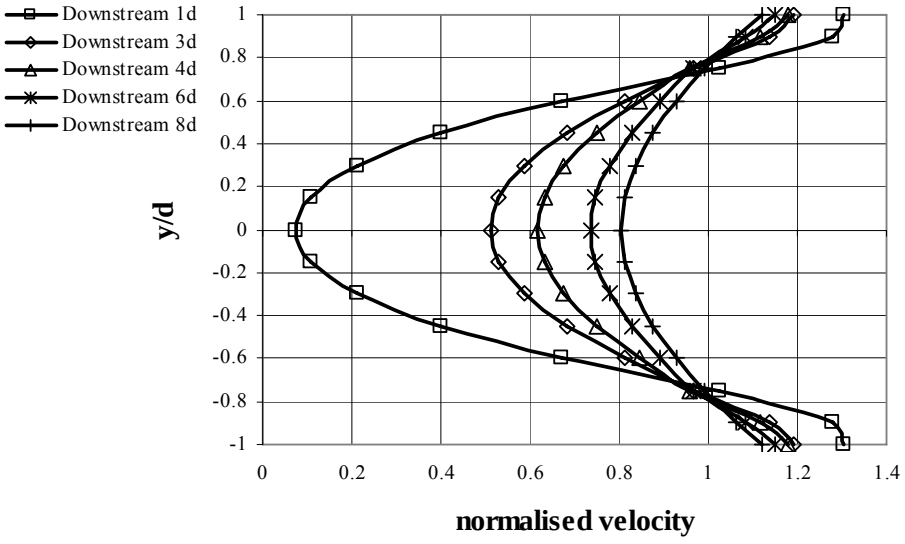

Figure 2.19: Profiles of normalised mean velocity at various downstream locations on the x - y central horizontal plane

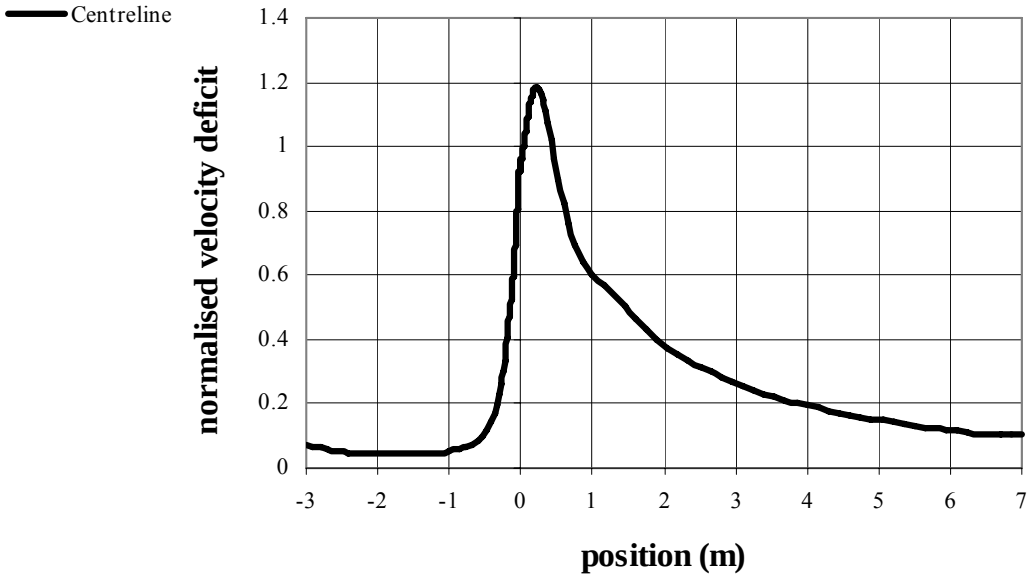

Figure 2.20: Normalised mean velocity deficit along the centreline of actuator disk in 3D model

2.5 Conclusions

Numerical simulation of energy extraction from moving water has been conducted by means of the CFD software FLUENT and is described in this chapter. The parameters, including the characteristic length and the inertial resistance coefficient of the actuator disk, were intentionally set to the relatively large values in the numerical model established in this chapter, with the aim to clearly demonstrate the effects of large-scale extraction of tidal current energy on the surrounding environment.

The most important findings of this chapter and also their implications in relation to tidal current energy extraction have yielded some general conclusions and are listed as follows:

1. A significant free surface drop can arise due to energy extraction from moving water. The development of numerical methods for explicitly predicting the effects of energy extraction from tidal currents needs to take into account the existence of a free surface as well as the influence of its deformation. That is, regarding the free surface as a solid boundary in the simulation of tidal current energy extraction is not appropriate.
2. The energy loss in the wake can be replenished over a certain downstream distance, which makes it viable to allow tidal energy extraction devices operating in clusters and being arranged in rows.
3. The blockage ratio is a crucial factor in the consideration of the impacts of a tidal farm. A large scale tidal farm may tend to obstruct the channel and cause

a high blockage ratio. Therefore, the velocity of the incoming flow can be reduced, as shown in 2D numerical results, and consequentially the estimated available energy can be decreased since the tidal kinetic energy flux is proportional to the cube of tidal current velocity. However, the acceleration of flow velocity around the energy extraction device due to the blockage effect, which has been identified in 2D and 3D numerical simulations, could increase the energy to be captured for the downstream devices and possibly reduce the distance between the rows of tidal devices in a farm. Accordingly, the feasible number of units to be installed as well as the turbine spacing in lateral and longitudinal directions in a tidal farm needs to be carefully designed.

4. Tidal energy extraction can critically change the underlying characteristics of a flow field since tidal current energy exists in a highly restricted region which is between sea surface and seabed. As a result, the energy available from tidal current is not infinite because of the environmental constraint. The upper limit on the extractable energy needs to be determined in response to the specific features of a tidal energy site to be exploited.

Chapter 3

COMPUTATIONAL FLUID DYNAMICS (CFD) SENSITIVITY STUDY FOR ENERGY EXTRACTION FROM TIDAL CURRENTS

Overview

This chapter aims to assess the effects of variations of input parameters on the energy extraction from tidal currents, based on the modified 3D computational fluid dynamics (CFD) model described in section 3.1. The influence of freestream turbulence level is examined in section 3.2. The influence of submerged water depth is investigated in section 3.3, and the influence of different water inlet velocities is analyzed in section 3.4. Finally, the conclusions are given in section 3.5.

3.1 3D CFD Model for Sensitivity Study

A sensitivity analysis was undertaken to assess the influence of input parameters in the 3D CFD model for simulating energy extraction from tidal currents. The sensitivity study focused on changing one parameter value at a time and comparing the consequential numerical results. Thus an enormous number of cases have been

investigated. The original 3D grid set up in chapter 2 was used firstly, but it took nearly 4 or 5 days to get convergent results for each case being tested in FLUENT. In order to reduce the computation time required, a shorter water flume was constructed that was 7000 m long, 1500 mm wide, and 1200 m deep with a water depth of 1000 mm and consisted of approximately 11 900 hexahedral cells. It can be regarded as another grid independence check for the previous 3D model and further verify the issues addressed in chapter 2. A smaller actuator disk with the characteristic length of 250 mm was set at 2000 mm downstream from the inlet boundary of the computational domain and was employed in all the cases examined in the sensitivity study, primarily in order to facilitate adjusting the submerged depth of the actuator disk in the water and minimize the blockage effects in those cases. Other parameters were kept the same as the previous 3D model, except that the parameters like freestream turbulence intensity, the submerged water depth of actuator disk, and the water velocity were varied to study how these parameters impacted the energy extraction from water. The simulation conditions applied for the sensitivity study and the cases which have been examined were summarized in Table 3.1.

The normalised mean velocity deficit along the centreline of the actuator disk was plotted for each case in the sensitivity study, which was used to present the recovery of wake along the downstream distance [96] and was essentially the decimal percentage of initial free stream velocity. So, when the downstream flow velocity is equal to the freestream velocity, the velocity deficit is zero. This is a factor of particular importance in determining the optimal spacing of the devices arranged in rows, in order to increase the energy available to devices. These may operate in the wake of upstream devices within a tidal farm.

In-depth research on tidal energy extraction has only recently been prioritised. Therefore, the available literature relevant to this research both experimentally and theoretically, is limited at present. Since the physical mechanisms underlying the energy extraction from flow (air or water) are similar, it is reasonable to believe that there are similarities between wind turbine wakes and tidal turbine wakes. Hence, numerous publications on wind energy have been consulted while developing understanding of the wake formed by energy extraction from water in the results of this sensitivity study.

Parameter examined	Characteristic length of the actuator disk d (mm)	Inertial resistance coefficient $C_{2i,j}$ (1 m^{-1})	Free stream velocity U_∞ (m s^{-1})	Free stream turbulence intensity I (%)	Submerged water depth h (mm)
Free stream turbulence I	250	2667	0.76	1 5 12	250
Submerged water depth h	250	2667	0.76	1	250 375 500
Inlet water velocity U_∞	250	2667	0.5 0.76 1.5	1	250

Table 3.1: A summary of simulation conditions for the sensitivity study

3.2 The Influence of Freestream Turbulence

3.2.1 Varying the Freestream Turbulence Level

According to FLUENT [79], a flow having a inlet turbulence intensity of $\leq 1\%$ is a low turbulence flow and with a inlet turbulence intensity of $\geq 10\%$ is a high turbulence flow. Therefore, three cases have been tested in FLUENT with the inlet turbulence intensity I = 1% (low turbulence) in case 1, 5% (moderate turbulence) in case 2 and 12% (high turbulence) in case 3 separately. The standard two-equation k - ε model was applied for the turbulent flow calculations. k and ε were approximated by using the equations in FLUENT given below and were utilized for initializing the entire flow field before iterations started [70].

$$k = \frac{3}{2}(U_\infty I)^2 \tag{3.1}$$

where U_∞ is the freestream mean velocity and is set as 0.76 m s^{-1}.

$$\varepsilon = C_\mu^{3/4}\left(\frac{k^{3/2}}{l}\right) \tag{3.2}$$

where C_μ is an empirical constant specified in the turbulence model and is 0.09. l is the turbulence length scale, a physical quantity related to the size of large eddies that contains the energy in turbulent flows and is determined by equation (3.3).

$$l = 0.07 D_h \tag{3.3}$$

where D_h is the hydraulic diameter for a channel having a non-circular cross-section.

The I , k and ε employed in three cases being examined in FLUENT are listed in Table 3.2. Other parameters were kept the same as the previous 3D model.

Case examined	I (%)	k ($m^2 s^{-2}$)	ε ($m^2 s^{-3}$)
Case-1	1	$\approx 8.664\times10^{-5}$	$\approx 1.104\times10^{-6}$
Case-2	5	$\approx 2.166\times10^{-3}$	$\approx 1.380\times10^{-4}$
Case-3	12	$\approx 1.248\times10^{-2}$	$\approx 1.909\times10^{-3}$

Table 3.2: The various input values of I , k and ε specified for the freestream turbulence

3.2.2 Numerical Results and Discussion

The wake velocity deficit and its decay rate (i.e., change in velocity deficit with respect to downstream distance) is mainly determined by the drag force on the rotor and the ambient turbulence level [94]. The drag force is also referred to as 'thrust force' in wind energy terminology and acts upon the rotor in the direction of undisturbed freestream velocity. It can be represented by the momentum-flux deficit in the wake and thus is an important factor to determine the nature of the wake flow, which is generated due to energy loss [95, 97-98]. The drag force is produced by the pressure difference across the rotor. Since the pressure difference is pre-defined by the inputs for the porous medium model in FLUENT, it assumes that the drag forces exerted on the actuator disk in three cases being studied were the same due to the identical inputs applied. This assumption is reasonable because the freestream turbulence has barely any effect on the drag force has already been identified in the wind turbine experiments [99, 100]. The similar drag force implies the momentum deficit of the wake in those three cases should be approximately same, thus the

recovery of downstream wake is governed by the transport of momentum from freestream into the wake.

The normalised centreline mean velocity deficit for varying levels of freestream turbulence intensity in the vertical x - z plane is presented in Figure 3.1. It can be seen that the increased levels of freestream turbulence result in a faster recovery of downstream flow to its initial velocity. This is indicated by the slope of the velocity deficit line behind the actuator disk that is located at the origin of x coordinate. This tendency shows agreement with the reported results in the literature [88] and has been extensively acknowledged in the study of wind turbine wakes [99, 101-103]. It has been recognized that external turbulence in the ambient flow plays an important role in the re-energization process of downstream far wakes because of its effect on the mixing and entrainment rate in the wake. The higher ambient turbulence tends to transport the momentum from freestream into wake more effectively and thus the decay of downstream wake is sped up.

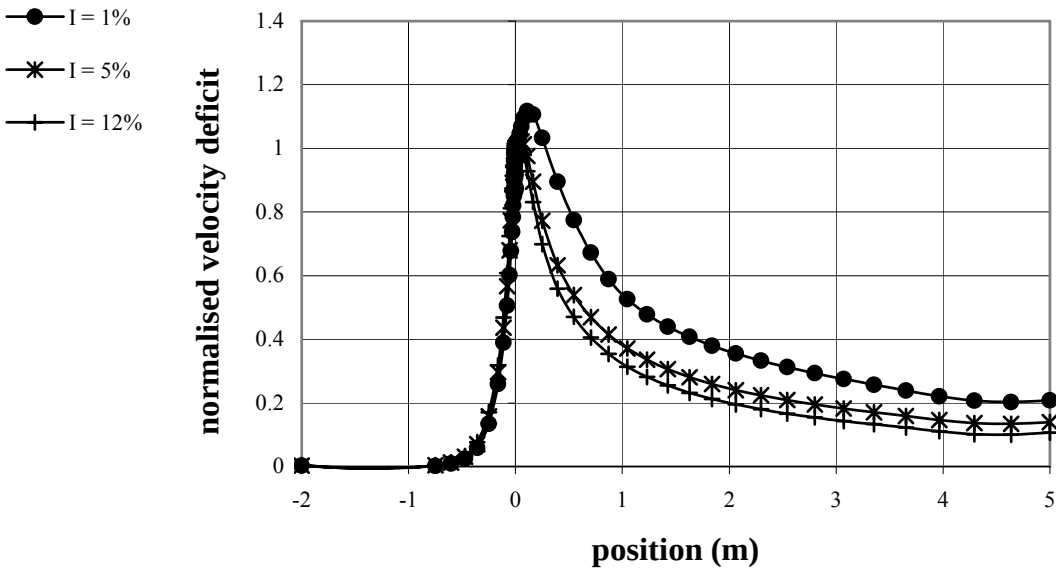

Figure 3.1: Normalised centreline mean velocity deficit for various freestream turbulence intensities

3.3 The Influence of Submerged Water Depth

3.3.1 Varying the Submerged Water Depth

The determination of submerged depth for a tidal energy extraction device is vital and largely depends on the installation techniques to be applied. For example, the method of positioning a rotor underneath a floating vessel makes it feasible to pre-define the depth under surface for the rotor, compared to the method of installing it on a structure fixed to the seabed. In general, the device is believed to operate more efficiently when mounted close to the free water surface where the kinetic energy of the water is largest. A sufficient distance from the tidal device to the free surface is imperative to avoid the devastating loading acting upon the device due to surface waves and to reduce the risk of interactions with shipping. The influence of submerged water depth is investigated here by adjusting the distance from the actuator disk to the surface. The aim is to identify what effects, if any, the free surface had, on the downstream wake. Three cases were tested in the 3D CFD model, in which the distance h from centre of actuator disk to the free surface boundary were set to be 250 mm ($1\,d$) in case 1, 375 mm ($1.5\,d$) in case 2 and 500 mm ($2\,d$) in case 3 respectively. d was the characteristic length of actuator disk in the model, which was 250 mm. Only the tranquil surface condition was considered in those cases. The uniform velocity of the incoming water was 0.76 m s^{-1} and thus the same amount of energy is expected to be extracted in three cases. Other parameters were kept unchanged like the previous 3D model.

3.3.2 Numerical Results and Discussion

The normalised centreline mean velocity deficit, for varying actuator disk submergence, is plotted in Figure 3.2 and the streamwise velocity contour showing downstream wake is presented in Figure 3.3 (a-c) for varying depths of the actuator disk in the water. It is found that, when the actuator disk is placed closer to the free surface, the downstream wake can reach the free surface faster and the decay of centreline velocity deficit in the wake is increased. This result is thought to be the cause of the interaction between the free surface and the wake because the influence of the free surface on the free shear flows, like a submerged jet, has been well-studied and identified [104, 105]. Another factor, which may also contribute to this result, is that the deformation of the free surface, arising from the energy extraction, more readily occurs when the actuator disk is placed in proximity to the free surface. The free surface drop may enhance the mixing of the wake flow with the ambient flow, so that the decay of the wake is accelerated. This result indicates that, in order to get a more precise prediction, the wake modelling should include the free-surface effect, especially when the tidal current devices might need to be installed relatively close to the free surface, like in a shallow tidal channel.

In order to identify possible influence of free surface on the wake recovery, the incoming flow is assumed to have a uniform velocity profile in this sensitivity study. Contrarily, the velocity along the water column is not uniform, which is always greatest close to water surface and deceases rapidly close to sea bed, particular in a shallow open channel. In such circumstances, more energy can be captured by a tidal current device in proximity to water surface. Thus, a slower wake recovery can be expected to happen compared to a device situated closed to the seabed.

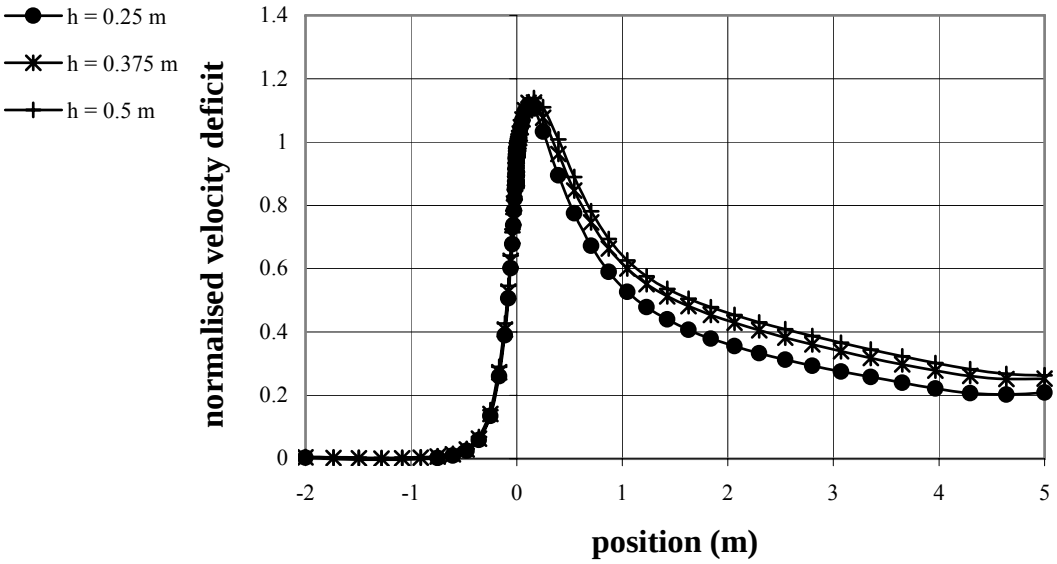

Figure 3.2: Normalised centreline mean velocity deficit for various submerged depths of actuator disk

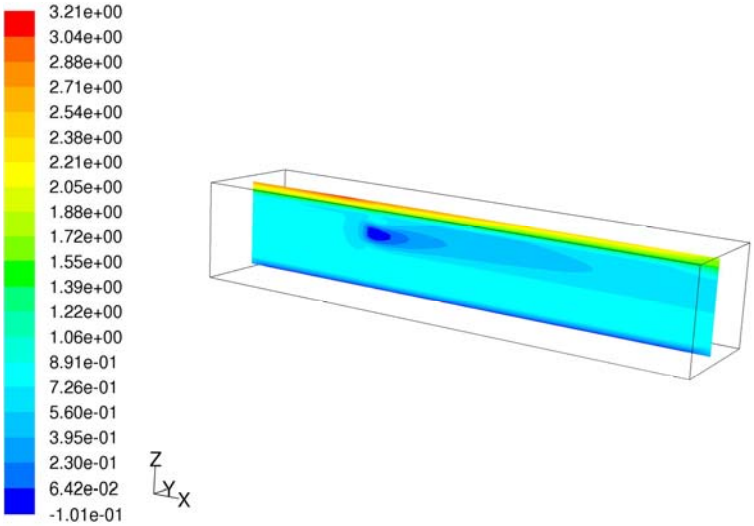

(a) $h = 250$ mm

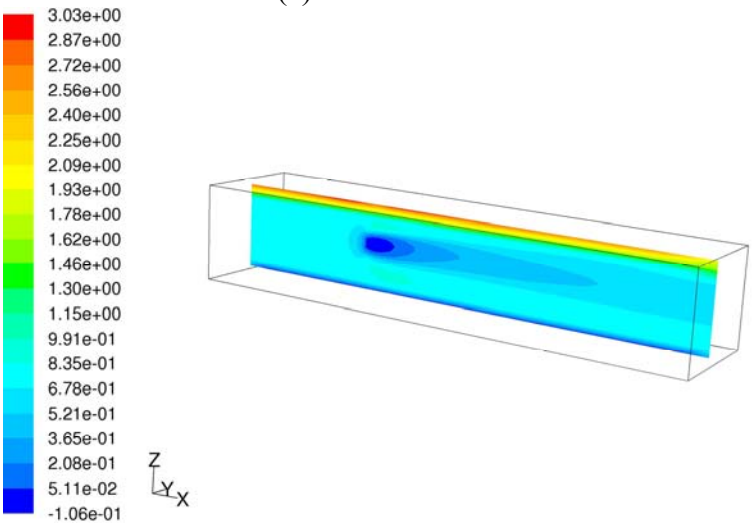

(b) $h = 375$ mm

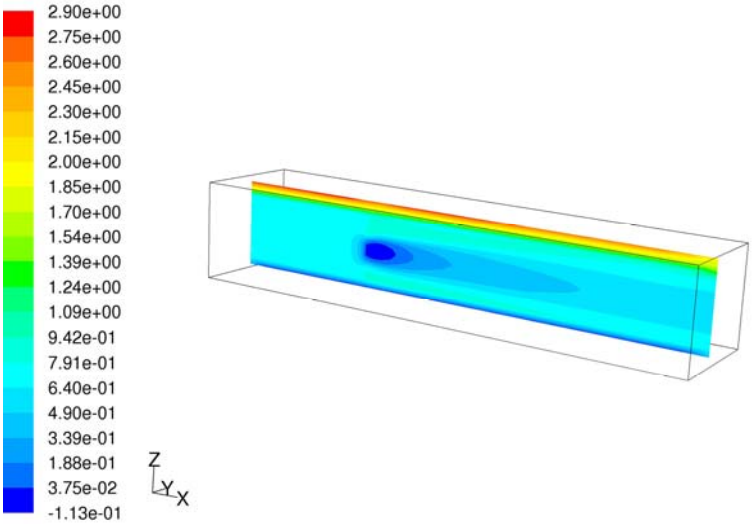

(c) $h = 500$ mm

Figure 3.3: Contours of streamwise velocity on the x - z central vertical plane for various submerged depths of actuator disk

3.4 The Influence of Water Velocity

3.4.1 Varying the Inlet Water Velocity

Tidal current energy extraction is sensitive to the flow velocity. More energy can be expected to be captured from faster flows for a tidal energy device operating at a constant speed. A free surface drop associated with energy extraction from water is identified in 2D and 3D numerical models in chapter 2, in which the deformation of the free surface could be augmented because of the effect of a high blockage ratio. A small actuator disk with a considerable low blockage ratio of approximately 4% was applied in the study of the relationship between energy loss and free surface elevation. This was tested by varying the values of inlet water velocity U_∞ in the 3D numerical model. Three different inlet water velocities: 0.5 m s^{-1} in case 1, 0.76 m s^{-1} in case 2 and 1.5 m s^{-1} in case 3 were examined and their corresponding flow Froude number were 0.16, 0.24 and 0.48 respectively. It was recognized that the present numerical model with 1.5 m s^{-1} uniform flow will be equivalent to an 8 m s^{-1} flow in a 30 m deep channel, which is quite unlikely for a real tidal site where tidal current devices could be installed. However, as it was only aimed at clearly demonstrating the influence of incoming flow velocity on the energy extraction from tidal currents and on the development of the downstream wake in this sensitivity study. Therefore, the inlet velocity of 1.5 m s^{-1} was still tested in the numerical model. Other input parameters were remained the same as the previous 3D model.

3.4.2 Numerical Results and Discussion

The normalised centreline mean velocity deficit is shown in Figure 3.4. The centreline velocity deficit increases as water velocity increases, which is associated with more energy loss when water passes through the actuator disk. For the water velocity of 1.5 m s^{-1}, the downstream recovery rate of velocity deficit is accelerated rapidly over a short distance downstream between 0 and 1000 mm, where the large deformation of free surface occurred. The free surface elevation is illustrated in Figure 3.5 (a-c) for three different water velocities. It is observed that the deformation of the free surface can be aggravated by more energy being extracted. It is argued that an extreme situation caused by the free surface drop could happen when the subcritical flow ($F_r < 1$) downstream of an energy extraction device passes through the critical depth h_c [4] of an open channel ($F_r = 1$) and becomes supercritical flow ($F_r > 1$). Thus, the flow condition can become dramatically unstable [92]. This extreme situation is a rare encounter in the real world but it can easily happen under the laboratory conditions if the water depth is shallow and the water velocity is high. Thus, the device will be tested in the flow with a high Froude F_r number and work close to the critical depth of channel. This issue need be considered in the experimental design for a tidal current energy extraction device.

Simulation result also was compared with the experimental results, which have been obtained under conditions similar to the numerical model [56, 93]. Difference was noticed that the influence of incoming flow velocity on the downstream wake

4. $$h_c = \left(\frac{Q^2}{gB^2} \right)^{1/3}$$
where Q is the volume flow rate, B is the width of the channel and g is the acceleration of gravity.

decay was not so obvious in the measurement result reported in Ref. 56 as the result shown in the numerical model. One reason for this difference might be that the velocities applied in Ref. 56 were relatively close, which were 0.248 m s^{-1}, 0.294 m s^{-1} and 0.331 m s^{-1} respectively [56]. Therefore, an apparent trend could be difficult to be identified. Nevertheless, the numerical result agreed well with another experimental measurements reported in Ref. 93 [93], in which the experimental conditions were found more similar to the present numerical model. Both numerical and experimental results showed that the faster the flow, the more energy can be extracted from it and thus cause a slower wake recovery, as shown in Figure 3.4.

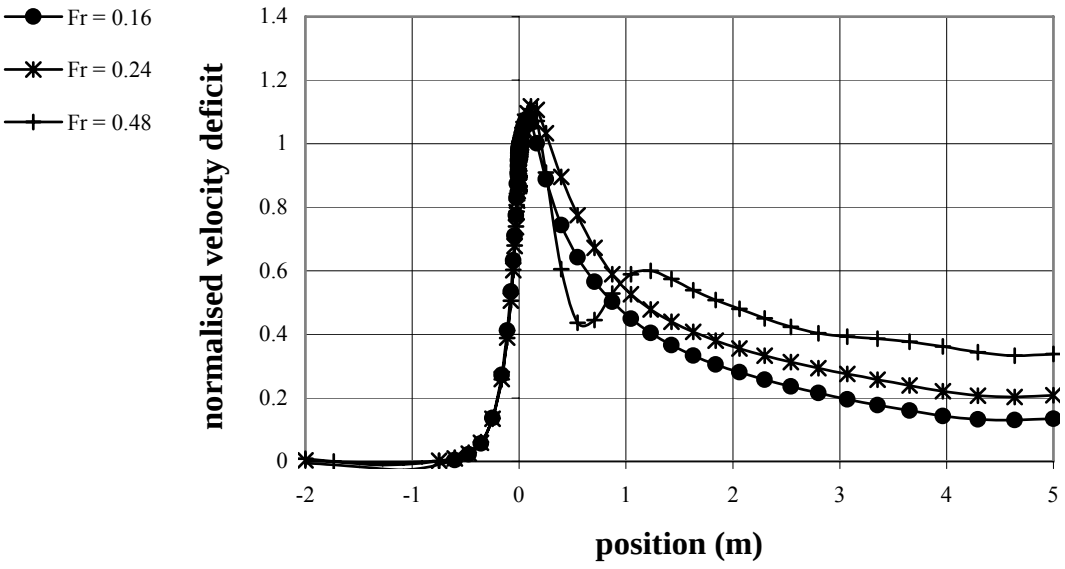

Figure 3.4: Normalised centreline mean velocity deficit for various inlet water velocities

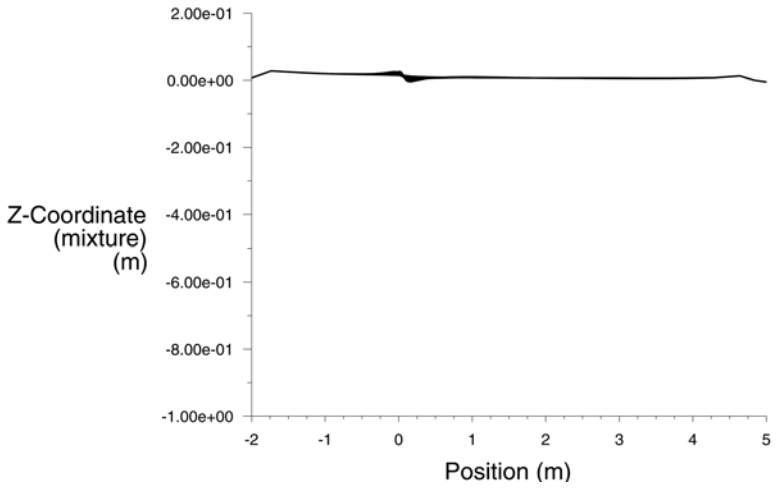

(a) $U_\infty = 0.5$ m s^{-1}

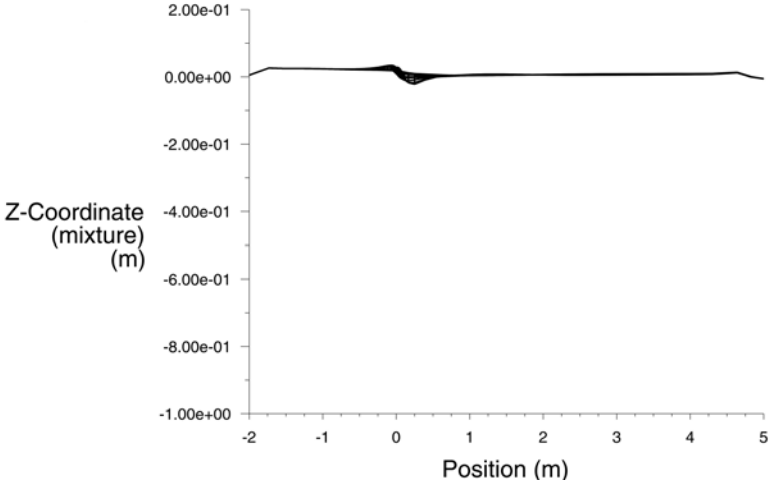

(b) $U_\infty = 0.76$ m s^{-1}

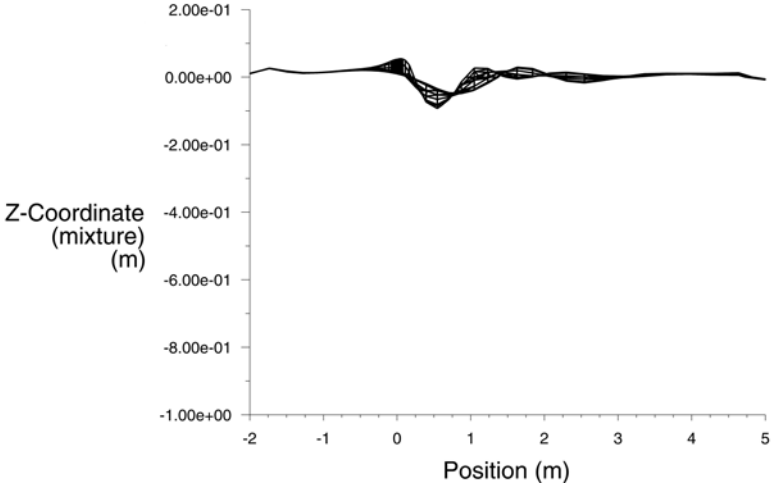

(c) $U_\infty = 1.5$ m s^{-1}

Figure 3.5: Free surface elevation for various inlet water velocities

3.5 Conclusions

The main conclusions in this chapter can be stated as follows:

1. The velocity recovery in the wake is accelerated by increasing the freestream turbulence level.
2. The velocity recovery in the wake is accelerated when the actuator disk is positioned in close proximity to the free surface, assuming a uniform incoming flow.
3. More energy loss gives rise to a longer downstream distance required for the wake recovery.
4. The wake velocity recovery can be accelerated within a short downstream distance under the influence of the free surface deformation.
5. The free surface drop is aggravated by more energy being extracted.

Chapter 4

EXPERIMENTAL STUDY OF ENERGY EXTRACTION FROM TIDAL CURRENTS IN A WATER CHANNEL

Overview

Based on those findings related to the consequences of energy extraction from tidal currents on the surrounding flow, physical experiments were designed to validate the numerical results. The first experiment was carried out in moving water at a field site, chosen to replicate the actual operating condition for tidal energy extraction converters. In this chapter, the experimental process for the first testing programme is documented and the experimental results are presented. The experimental instrumentation used is introduced in section 4.1. The experimental concept and the testing environment are described in section 4.2. The experimental steps are expressed in section 4.3. The experimental results and discussion are displayed in section 4.4. Conclusions are given in section 4.5.

4.1 Experimental Instrumentation

4.1.1 Tidal Current Turbine Simulator

Precise prediction of the wake development is vital when a large number of tidal current turbines are working together in a 'farm'. An experimental approach is the most straightforward and inexpensive method that can provide detailed information of turbine wake characteristics. Comprehensive experimental studies of wind turbine wakes are conventionally conducted through testing various small-scale wind turbine models in wind tunnels under controlled upstream conditions. It has been found that a turbine will start to perform as a disk at high tip speed ratios [99, 106] and the rotor wake flow is quite similar to that behind a stationary disk-like body [95, 107-109]. Additionally, the thrust force on the turbine is the major factor in the wake development, which must be adequately modelled in the experiments. An appropriate range of thrust forces on a real turbine can also be simulated by perforated disks with various porosities. Therefore, perforated disks can provide appropriate physical knowledge to help understand turbines and has been widely used in a turbine simulation in wind turbine experiments [95, 110-113]. The rotation of a wake due to rotating turbine blades is neglected when simulated by a stationary disk. But it is believed that the wake rotation is not one of more important features in the wake re-energization process [95]. Generally, the measurements need to be conducted a certain distance behind the disk, so that the flow characteristics particular to either the turbine or the disk can be negligible [95].

Several perforated disks were constructed and used as tidal current turbine simulators in the experiments for studying energy extraction from water. The energy is lost when the water passes through the disk and is converted to small-scale

turbulence. The perforated disks were fabricated from a 5 mm thick aluminium plate and the diameter was 250 mm for all the disks. Circular holes were drilled to allow the water through and were distributed as uniformly as possible in the disks. Various porosities (the ratio of the total area of holes to the disk area) were designed ranged from 14% to 50% in order to generate different thrust forces on the disks. The edge of each disk was phased at an angle of 45° so that the edge was sharp and the flat side of the disk was facing the flow in the experiments. Two disks, one with 14% porosity and a 20 mm hole diameter and the other with 50% porosity and a 25 mm hole diameter, are shown in Figure 4.1 and Figure 4.2 respectively.

4.1.2 The Test Support Frame

All the measurement instrumentation used was mounted on a support frame, which was designed and constructed specifically for the experimental programme. The frame size was 2500 mm long, 1500 mm wide and 1000 mm high. It consisted of a number of aluminium hollow bars that have a square cross section of 25 mm with a wall thickness of 3 mm. Three triangular aluminium plates were used at each corner of the frame to bolt the aluminium bars, two for the top plane of frame, and one leg together. Also, the frame legs were connected by bottom bars. Two extra cross bars were also used on the top plane of frame in order to improve the rigidity and stability of the whole frame. Two long bars were placed on the middle of the top frame and the interval between them was 20 mm. A series of holes with a regular interval of 250 mm (one diameter of the test perforated disk) were drilled in those two bars for the purpose of firmly positioning the test disk and measurement instrumentations between two bars by using bolts. Because of its simplicity, the support frame can be

broken down into individual pieces that are light and convenient to make transporting them easier.

4.1.3 The Pitot Probe

A pitot probe was fabricated in-house and was designed for the streamwise mean water velocity measurement based on the theory of pitot-static probes, which can be found in many textbooks on fluid measurement. The pitot probe was made of 20 mm diameter nylon rod bar, which has very low water absorption capability and can be easily machined. The total length of pitot probe was 210 mm.

A 6 mm diameter hole was mechanically drilled along the central axial line of rod bar and connected to one end of plastic tubing. The other end of tubing was inserted into a rectangular cavity that was cut on the top side of the pitot probe. Since this central hole faced the oncoming water, the stagnation pressure at that point can be measured and is called as stagnation port of the pitot probe. However, the stagnation pressure measurement can be influenced by the large local flow angles [114]. Thus, the tip of the pitot probe was also chamfered on the outside and resulted in an approximately 40-deg conical tip, in order to minimize this sensitivity, as guided by the literature [114]. Three 6 mm static pressure measurement ports were drilled 125 mm downstream from the stagnation port and were equally spaced at the right, left and bottom side of the pitot probe. Inside the probe body, the static pressure ports were connected to one continuous plastic tubing that extended into the rectangular cavity as well. Such design to connect multiple static pressure ports to a single pressure transmitting duct was expected to effectively reduce the effects of misalignment of the probe with the local flow direction on the measurements [115].

Inside the rectangular cavity, a miniature piezoresistive pressure transducer with an operating range from 0 to 0.5 psi was used to sense the differential pressure by connecting its two pressure inlet ports to the plastic tubings, one from the stagnation hole and the other from static holes respectively. Therefore, the pressure difference can be converted to a proportional electrical output that was transmitted by a 4-wire cable connected to the transducer, and be subsequently recorded through a data acquisition system. The performance of this differential pressure transducer was hardly influenced by the ambient temperature with a wide operating range of -40° to 85°C. Relevant information about the differential pressure transducer is also given in Table 4.1. Finally, the rectangular cavity was sealed with transparent silicone elastomer compound in order to protect and insulate the pressure transducer from the water. That the differential pressure transducer was enclosed inside the body of the pitot probe significantly minimized the length of the tubing between measured holes and transducer, giving the transducer a very fast response time. The dimensions of the pitot probe are shown in Figure 4.3 and one finished pitot probe is displayed in Figure 4.4.

Completed pitot probes were numbered from 1 to 5 and were assembled to form a pitot probe rake, which could measure the water velocity at five points simultaneously. The pitot probe rake also consisted of a pedestal and a vertical support, both of which were made of 19 × 19 mm square aluminium bars. Each pitot probe was mounted on the pedestal by a bolt going through the opposite end of the pitot probe from the measuring tip and a longer bolt, which was utilized for the center probe in the pitot rake, was also used to connect the pedestal and the base of the support together. Such a design allowed the pitot probes to be replaced

conveniently and made the pedestal able to be freely rotated at various angles around the vertical support. The spacing between the centres of the pitot probes was 100 mm in order to reduce the interaction between the individual probes [116]. The ratio of probe length to probe support thickness was designed to be large enough to minimize the interference effect of the support on the probe measurements, according to Gettelman and Krause [117]. The design of pitot probe rake was structurally rugged and was capable of use under harsh measurement conditions. The pitot probe rake is shown in Figure 4.5.

Each pitot probe was calibrated separately and the performance of the pitot probe rake was checked beforehand. The calibration process adopted is given in Appendix D as well as the calibration results for each pitot probe utilized in the experiment.

4.1.4 Load Cell

An "S" beam load cell with a load capacity from 0 to 2000 N was used for the measurement of force on the perforated disk in the experiments of this study. Its structure is shaped as a 'S' or 'Z', in which four strain gauges are electrically connected in the central sensing area to form a full Wheatstone bridge circuit. The mechanical force being exerted on the load cell caused the changes in the resistance of strain gauges which resulted in a voltage output proportional to the magnitude of the applied force. This analog signal was transmitted over a 6-wire cable that was connected to the load cell and was then recorded by the data acquisition system. Because of the full Wheatstone bridge being used, the force measurement in the present experiments was insensitive to temperature variations. The load cell was calibrated prior to the experiment by applying a series of known forces to it. The load

cell is illustrated in Figure 4.6 and its calibration curve, which showed the linear relationship between force acting on the load cell and voltage outputted by strain gauge, is displayed in Figure 4.7.

4.1.5 The Data Acquisition System

The differential pressure transducer and the load cell produced a voltage signal that was monitored through an analog-to-digital data acquisition system. The hardware for the analog-to-digital system in this experiment included an 8 channel datascan and a personal computer. Datascan is a measurement and data collection unit designed for the purpose of factory, industrial and scientific data acquisition applications and works as an interface between the computer and the electrical measurement devices. The heart of the datascan is a measurement processor, which performs the measurement and control of the datascan system. Measurement is conducted by an Analog to Digital converter being programmed to provide either 16 or 14 bits of resolution and is sensitive to 0.625 μV. The present datascan used in the experiment allowed up to 8 measurement devices to be connected through their cables to the plastic terminal strips mounted along the circumference. Therefore, the signals from all the connected devices could be measured synchronously. An isolated serial port provided on the datascan device enabled the user to communicate with the datascan using a computer by connecting them via a RS232 cable. The image of datascan is shown in Figure 4.8. An IBM laptop computer was utilized for the data acquisition in this experiment.

A windows-based software package called ‘Recorder’ supplied with the datascan was used to control the data acquisition process. It was broken down into two main

sections enabling the user to configure the datascan and record data to disk for later analysis by using a spreadsheet like Excel. A channel was assigned to each connected device automatically in the datascan and required to be configured, by using the selectable options that were provided in the 'Record' to determine the characteristics such as type of input signal, scanning speed, resolution, range and channel description. A completed configuration file needed to be loaded before the data acquisition process started. Real time data coming from all the channels could be monitored on the computer screen simultaneously when a red light was flashed on the panel of datascan to indicate that the data acquisition was in progress. At the same time, the data displayed on the screen could be logged to a disk and saved in Comma Separated Values (CSV) for easy import into the spreadsheet (Excel or Lotus 123) for analysis afterwards.

4.1.6 Power Source

A transducer needs a low voltage direct current (DC) input for operation, which is called its excitation voltage. Both pressure transducer and load cell required 10 V excitation voltage, while the datascan needed a 24 V DC power supply in this experiment. Because of the remote field conditions, batteries were found to be the only plausible power source for the whole system. Two 12 V sealed lead acid batteries of 10 Amp hour capacity, shown in Figure 4.9, were connected in series and were utilized to power up the datascan directly. A special circuit was made to reduce 24 V to 10 V, which could be applied to the pressure transducers and load cell. The batteries could last 24 hours and could be recharged overnight. The laptop computer

was powered by its battery, which could last at least one hour and another extra battery was prepared as a back-up power source.

Instrumentation	Suppliers	Model No.	Excitation Voltage Input
Differential pressure transducer	RS Components, UK	24PC series	10V
Load cell	Vishay Tedea-Huntleigh, USA	615	10V
Data scan	Measurement Systems Ltd., UK	7221	24V
12V lead acid battery	Rapid Electronics Ltd., UK	—	—
Laptop	IBM	—	—

Table 4.1: Information of experimental instrumentation employed

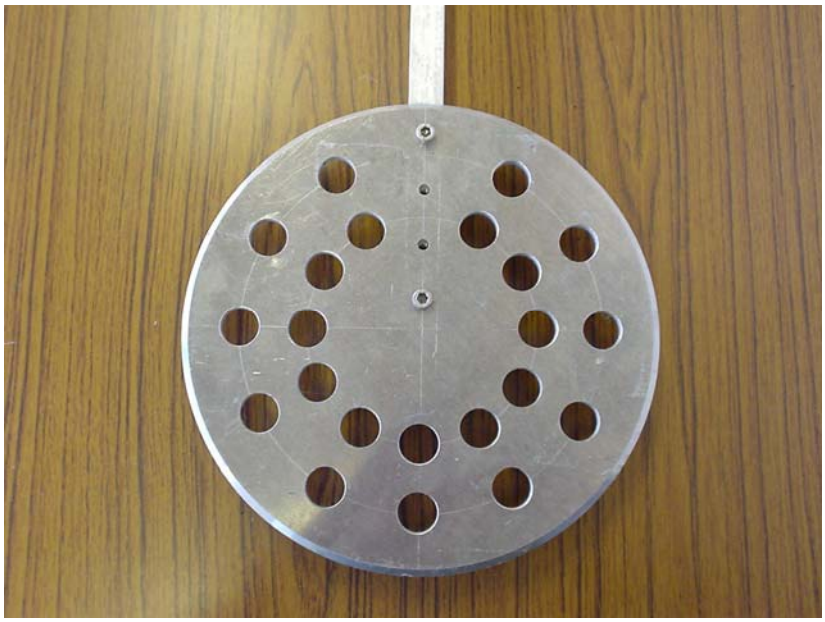

Figure 4.1: Perforated disk with 14% porosity

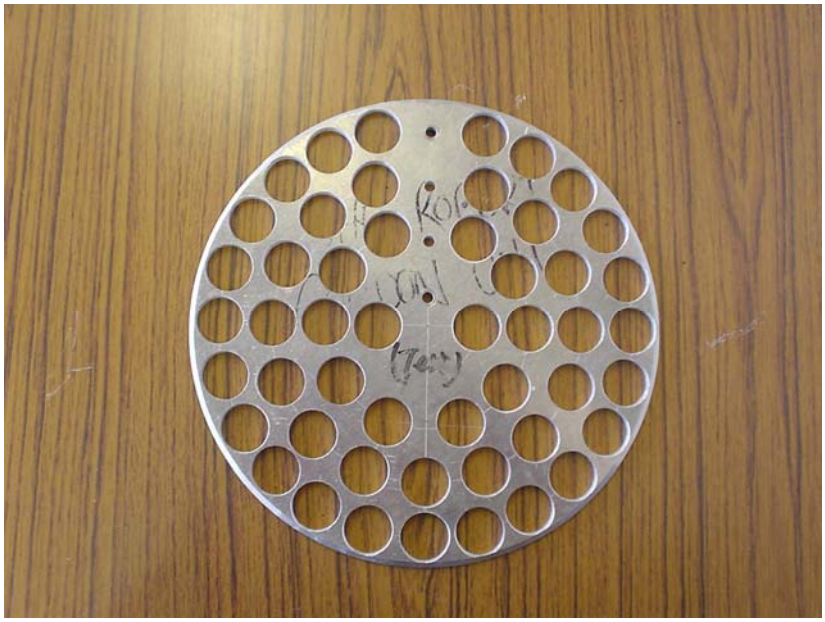

Figure 4.2: Perforated disk with 50% porosity

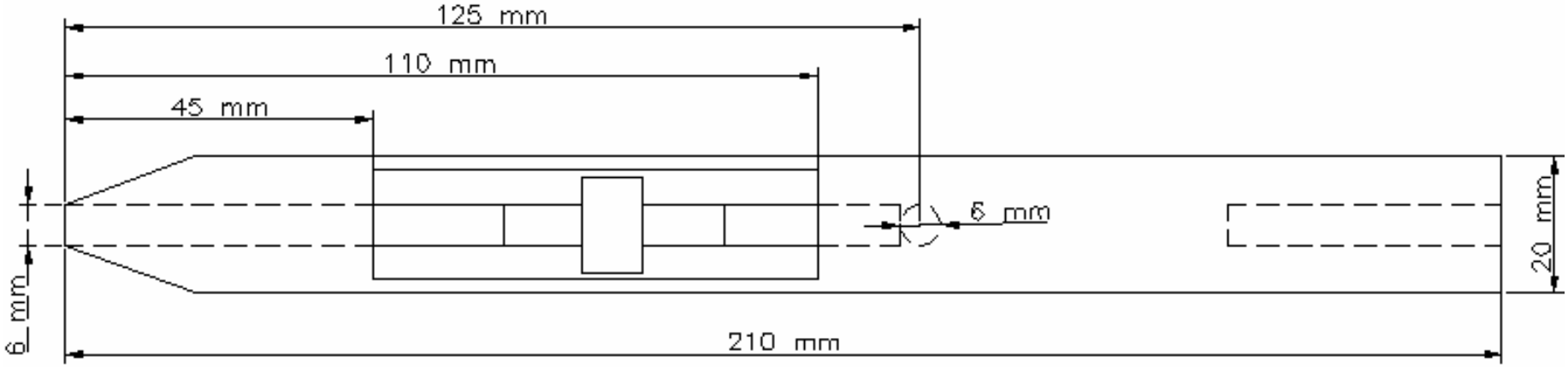

(a) Top view

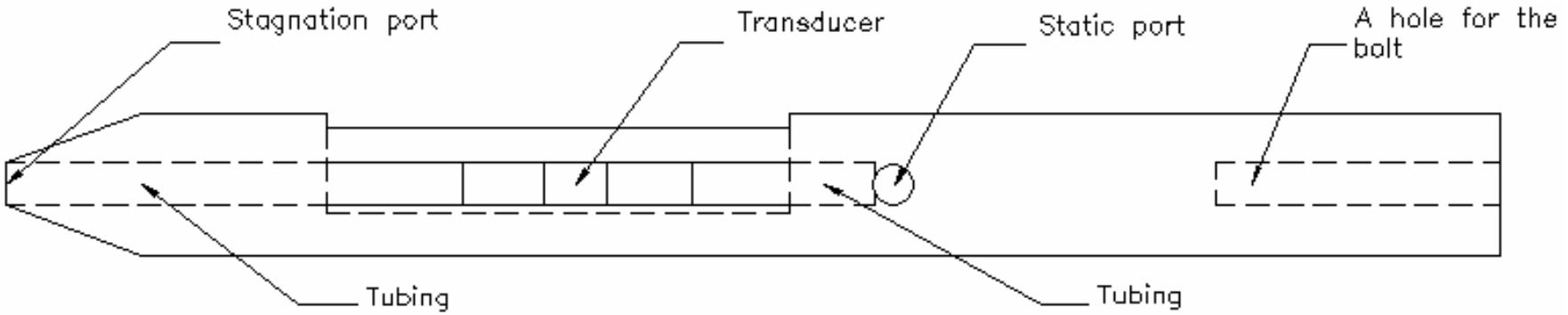

(b) Side view

Figure 4.3: Dimensions of pitot probe

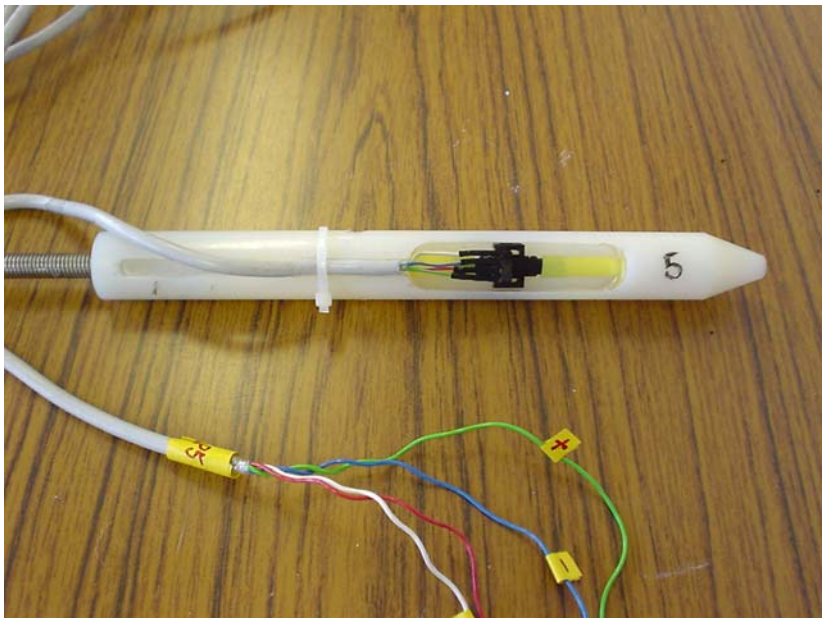

Figure 4.4: A pitot probe

Figure 4.5: The pitot probe rake

Figure 4.6: ‘S’ shaped load cell

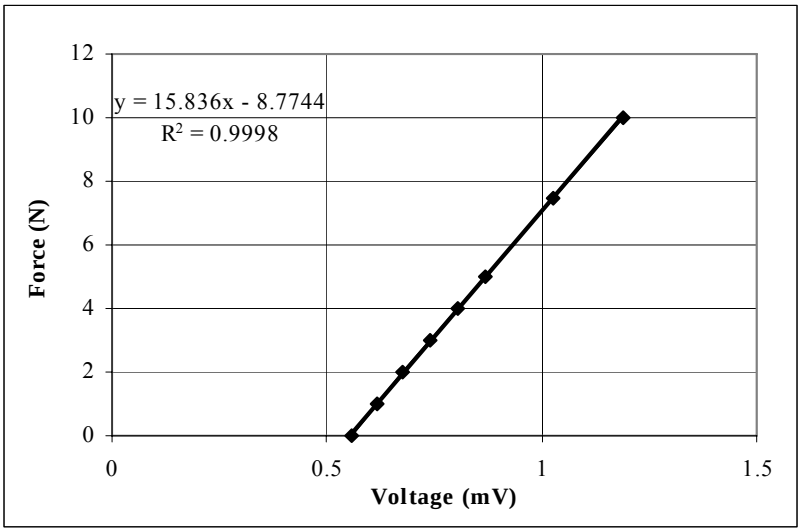

Figure 4.7: Calibration curve for the load cell

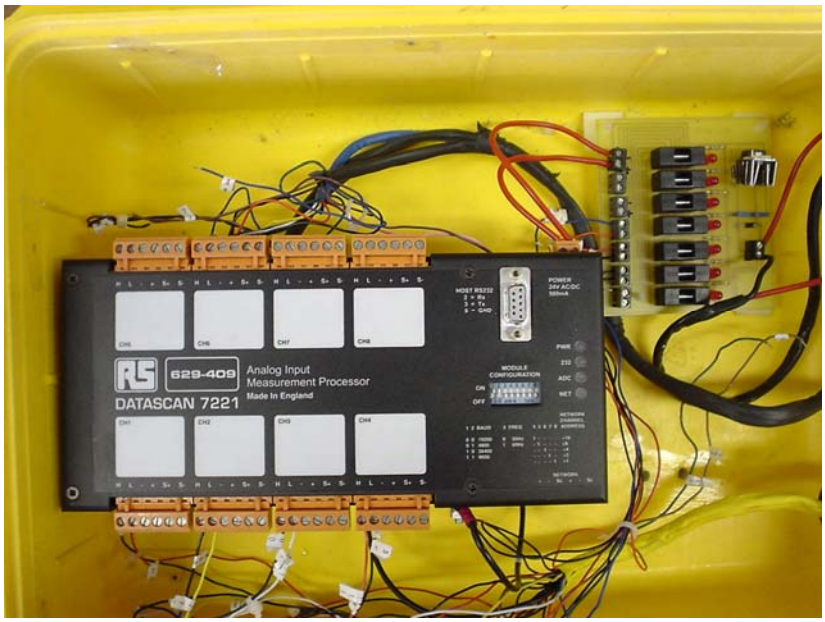

Figure 4.8: The datascan

Figure 4.9: The lead acid batteries

4.2 Test Facility

4.2.1 The Water Channel

In order to simulate the realistic operating environment of prototype tidal current energy conversion devices, the first experiments were carried out in moving water. The experiment was decided to be implemented in the field, because of the limitations of current water flumes in the laboratory as mentioned in section 1.3 of Chapter 1.

The test site selected was at Quoich Power Station on the River Garry near Invergarry. An artificial dam was established across the river for the production of electricity using hydro power, as shown in Figure 4.10. On one side of the dam, several large concrete structures were built and served as fish hecks, which were able to be safely accessed. Those structures enclose a concrete lined channel with a width of 3000 mm and a length of 3300 mm. A hoist was equipped inside one structure and was used to manually lift a horizontally configured bar screen that formed the bottom of channel above the water surface or adjust its depth in the water. The bar screen is illustrated in Figure 4.11. The mean water speed in the channel was approximately 0.76 m s^{-1}.

The Reynolds number based on the mean flow velocity and the hydraulic radius of the channel had 10^5 order and was much larger than 2000, the critical value of the Reynolds number at which transition to turbulence in an open channel occurred [118]. Therefore, the water within the channel was judged to be fully developed turbulent flow, as shown in Figure 4.12.

Figure 4.10: River Garry and dam

Figure 4.11: Bar screen raised above the water surface

Figure 4.12: A close up view of water within the channel

4.2.2 The Experimental Test Rig

An experimental test rig was designed and built for the purpose of collecting the data for the study of the wake developed behind perforated disk, as well as the thrust force acting on the disk, which simulated a tidal current turbine operating at a high rotor speed. The test disk was held by a strut made of a 19 mm×19 mm aluminium bar. A realistic design of support strut was adopted in order to ensure it reliable under challenging environmental conditions. The other end of strut can be inserted into the interval between the two middle bars on the top of support frame and could be attached tightly to the active end of the load cell using a bolt. The load cell was set on an L-shaped steel block with the other end tightened on it, as shown in Figure 4.13. The steel block was then mounted firmly on the middle bars of the frame. The force produced by water moving through the disk caused deformation of the load cell through the strut in a cantilever manner and thus the force can be measured. The wake velocity profile downstream disk was measured by the pitot tube rake. The support of the rake was inserted into the interval between the middle bars on the frame and was rigidly fixed on it. The height of pitot probe rake was adjusted to keep the tip of pitot probe, which was positioned in the middle of the rake, pointing towards the disk along the central axis of the disk. In this arrangement, the axes of the pitot probes were strictly parallel to the flow so as to allow accurate measurements. The pitot probe rake could also be moved easily along the middle bars of frame using the regular holes drilled on them and the distance between the measurement location and the disk could be determined in terms of the interval between holes, which was designed as 250 mm, one diameter of the disk. The datascan and batteries were put separately into two waterproof boxes for protection

and were secured to the rear frame support brackets. The laptop was connected to the datascan via a 1000 mm long cable and thus could be placed far away from the frame. The completed experimental test rig is illustrated in Figure 4.14.

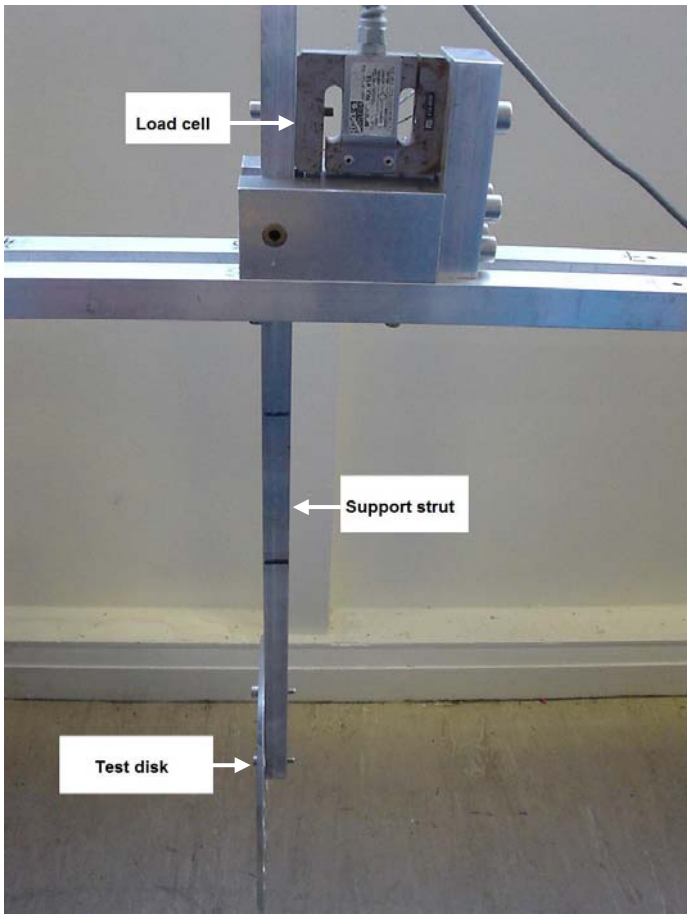

Figure 4.13: Drag measurement set-up

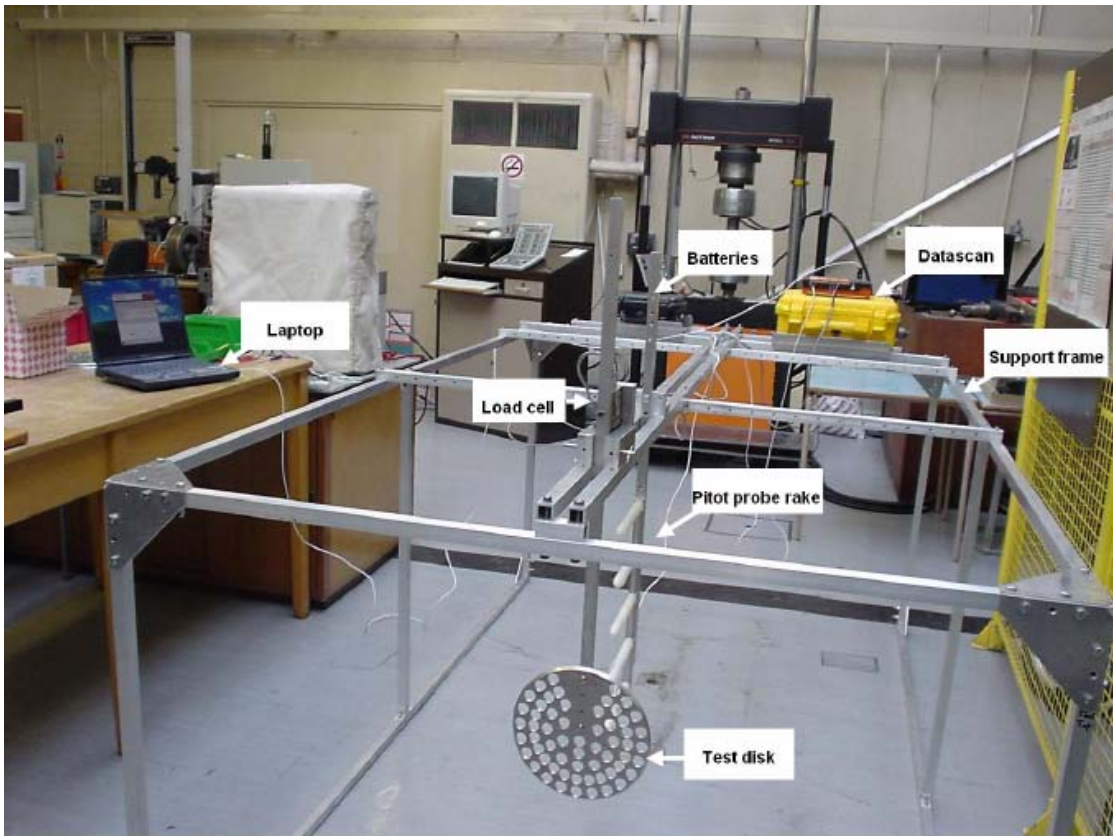

Figure 4.14: The experimental test rig

4.3 Procedures

The experiments were carried out in December 2005. All the instrumentation was transported to the field testing site by a van. The support frame was dismantled and then reconstructed on the site. On the day of the test, the frame was moved into the middle of the concrete water channel and was kept stable on the bar screen. The front of the frame was approximately 500 mm from the inlet region of channel. The test disk and measurement instrumentations were positioned on the frame in accordance with the experiment design. The laptop computer was put on a desk located on the nearby concrete platform. A wooden board was placed on the top of the frame and the operator could stand on it to perform the measurements. Perforated disks were tested in succession and the same experimental procedures were repeated for different disk testing. Every time the bar screen was raised above the water surface for changing the disk, the output of each pitot probe was recorded as its offset prior to the measurements. The bar screen was then slowly lowered into water until the water depth reached 950 mm. The initial flow velocities in the channel were measured at the start of the experiments. Afterwards, the test disk was set in place and its submerged depth h, the distance from the centre of the disk to the water surface, was adjusted to be 350 mm. When the measurement started close to the disk, an area of recirculating flow was identified as has been reported for a turbine operating at high tip speed ratio [108, 119]. Since the measurements by pitot probes would be affected by the reverse flow, the measurements were taken further behind the disk at 750 mm ($3d$), 1000 mm ($4d$) and 1500 mm ($6d$) downstream of the disk respectively. (d was the diameter of test disk). Measurements can not be

conducted at more positions downstream of disk because lengthen of the support frame was limited. During the measurements, the probe array was placed in a vertical position firstly and then rotated into a horizontal position, in order to measure the water velocity profiles in the vertical and horizontal planes of the wake. The data recordings were allowed to run for a period of approximately 60 seconds at each measurement position, with a sampling rate of 1 Hz. Six runs were conducted for each test disk. Efforts were made to minimize the time period needed for testing each disk in order to ensure the flow conditions in the channel keep stable for the duration of the experiment. Data were collected and saved on the laptop. A schematic diagram of the experimental setup was produced in Figure 4.15 and a flow chart was given in Figure 4.16 to clearly illustrate the steps taken during the experiment. In addition, a summary of all the perforated disks tested in the water channel and the total number of experimental runs conducted were given in Appendix E.

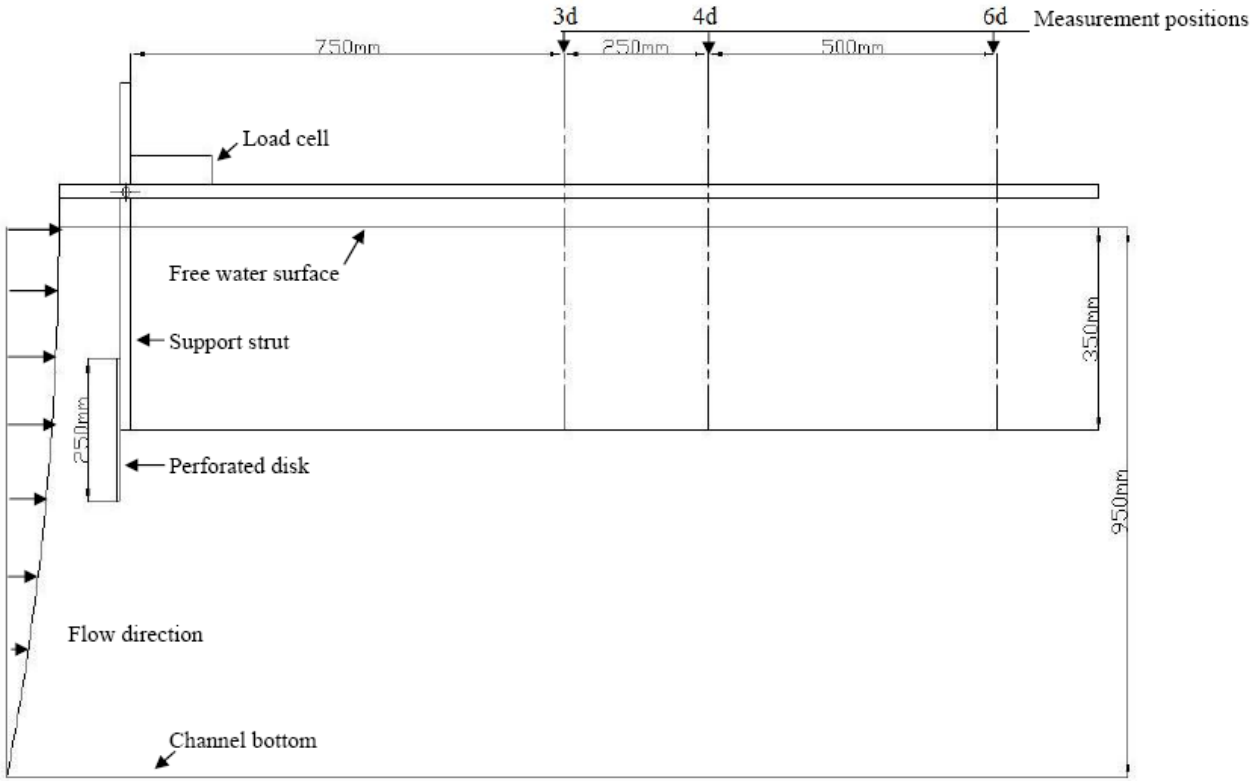

Figure 4.15: A schematic overview of the experimental setup in the water channel

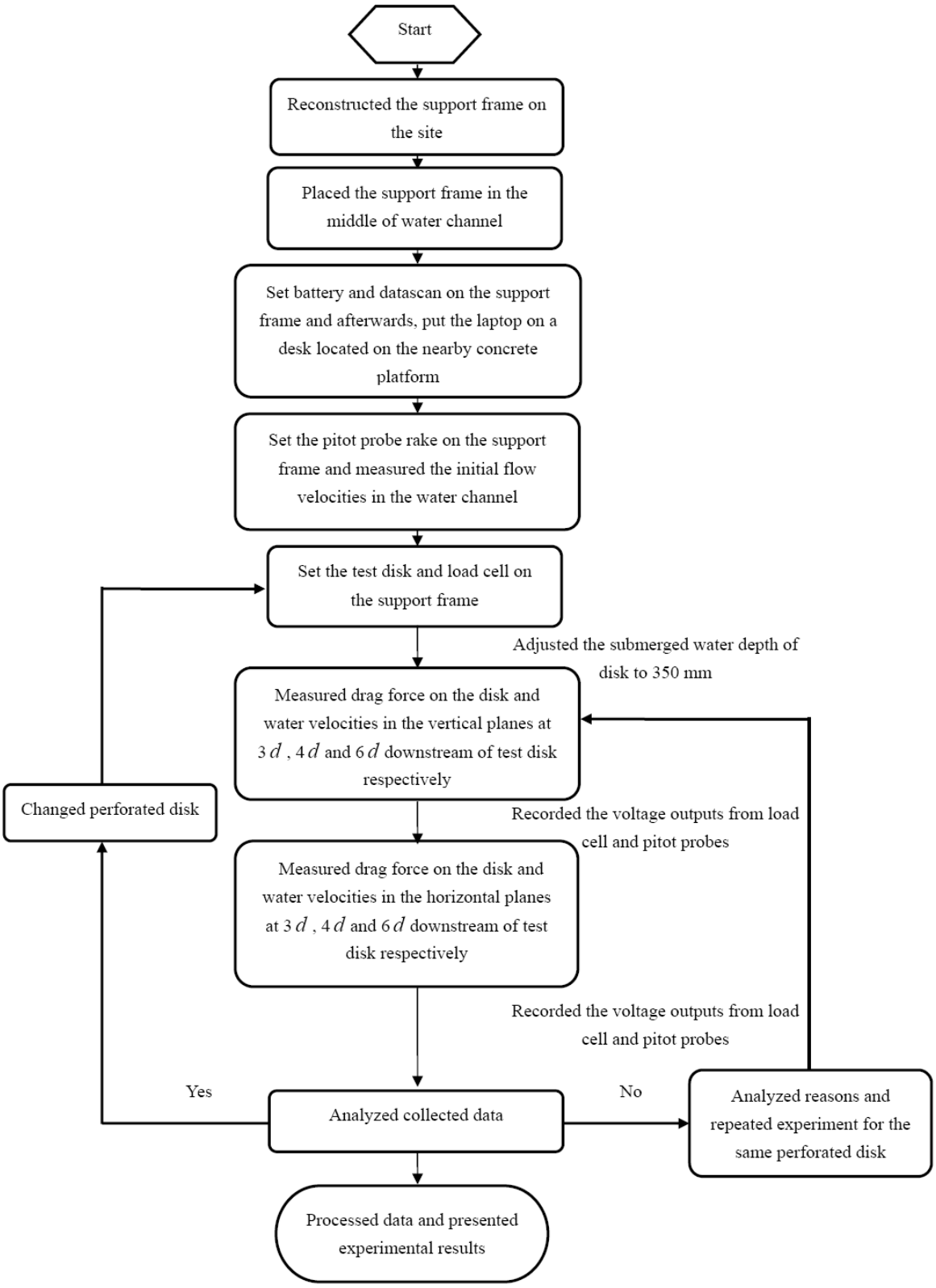

Figure 4.16: Flow chart of the experiment in the water channel

4.4 Results and Discussion

Raw data were processed for the force and water velocity calculations. Force on the test disk was obtained from the calibration curve of the load cell. The time fluctuations of the force were noticed, which were caused due to the turbulence in the water. The averaged drag force D on the disk was converted to drag (thrust) force coefficient using equation (4.1).

$$C_D = \frac{D}{\frac{1}{2}\rho U_\infty^2 A} \tag{4.1}$$

where U_∞ is the mean freestream velocity, A is the area of test disk and ρ is water density.

The water velocities were calculated using equation (4.2), in which the differential pressure Δp was measured by the pitot probe.

$$U_w = \sqrt{\frac{\Delta p}{\left(\frac{1}{2}\rho\right)}} \tag{4.2}$$

where U_w is the mean velocity in the wake.

For the tests, the ratio of the disk area to the channel section was 1.7%, which was relatively insignificant [95, 120]. Therefore, no correction was made to take account of the influence of blockage effect on the wake velocities measured. The distance from the bottom edge of the tested disk to the bar screen was nearly 500 mm, which was considered to be large enough to minimize the effects of the bar screen on the measurements.

A series of perforated disks were tested in the experiments. Only those results which could be replicated and which show the obvious wake characteristics of disk are presented.

The undisturbed freestream velocity profiles in the vertical and horizontal planes at different measurement positions are displayed in Figure 4.17 (a) and (b). It was found that the water velocities are greatest near the surface and are reduced with increasing measurement depth, which clearly illustrates the mean velocity gradient in an open channel flow. The water velocities are slightly reduced as the flow moved to the rear of the channel. But the water velocity profiles in the horizontal plane are almost constant. The readings measured at the hub height of disk ($h = 350$ mm) were averaged and used as the mean freestream velocity U_∞, according to the field measurements for wind turbines [121]. As expected, the force is reduced by increasing the porosity of the test disk and gives a typical drag force coefficient for an actual turbine running at high tip speed ratio. The averaged drag forces and drag force coefficients on the measured disks are given in Table 4.2. The velocity profiles behind the test disk, with 14% porosity are displayed in Figure 4.18. The velocity profiles behind the test disk with 50% porosity are shown in Figure 4.19. In those figures, the top line along the zero water depth represented the free surface. The wake, which is characterized by an area of reduced velocity behind the test disk and recovers to the free stream velocity with downstream distance, is clearly observed in the experimental results. The wake profile measured resembles a distinct Gaussian distribution and, as the wake recovers, it gradually loses its intensity. The results are encouraging in that these dominant features of velocity profiles are in qualitative agreement with the numerical predictions, as well as the development of the wake

behind an actual turbine [119]. Moreover, it is noted that the vertical velocity profiles show an asymmetry about the wake centreline and it is especially pronounced for the profiles behind the disk with 14% porosity. It is partly due to the influence of the strut behind the disk and also the high solidity of disk with low porosity. In addition, the velocity gradient of incoming flow could exaggerate this asymmetry further.

Test disk	Averaged velocity at hub height of disk ($m\ s^{-1}$)	Area of disk (m^2)	Averaged drag force (N)	Drag force coefficient C_D
Disk with 14% porosity	0.760	0.049	14.111	0.997
Disk with 50% porosity	0.760	0.049	10.199	0.721

Table 4.2: Results of drag force and drag force coefficient from the first experiment

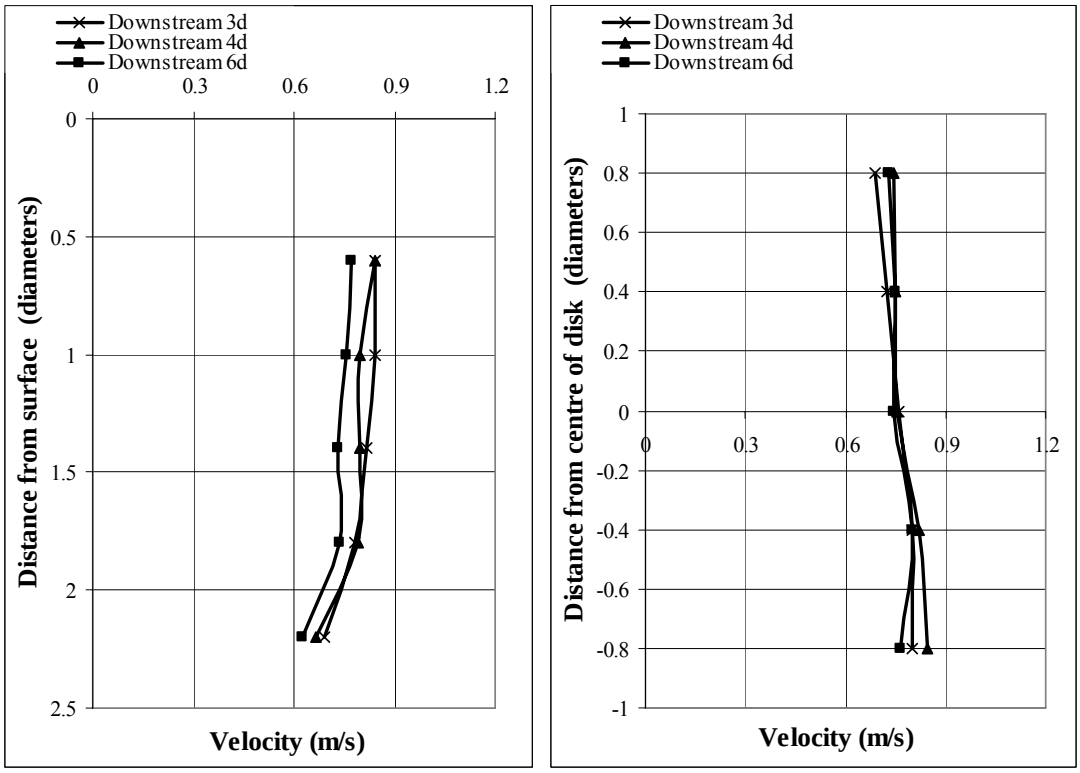

(a) (b)

Figure 4.17: Free water velocity profiles in the vertical planes (a) and the horizontal planes (b) at downstream distances 3, 4 and 6 disk diameters

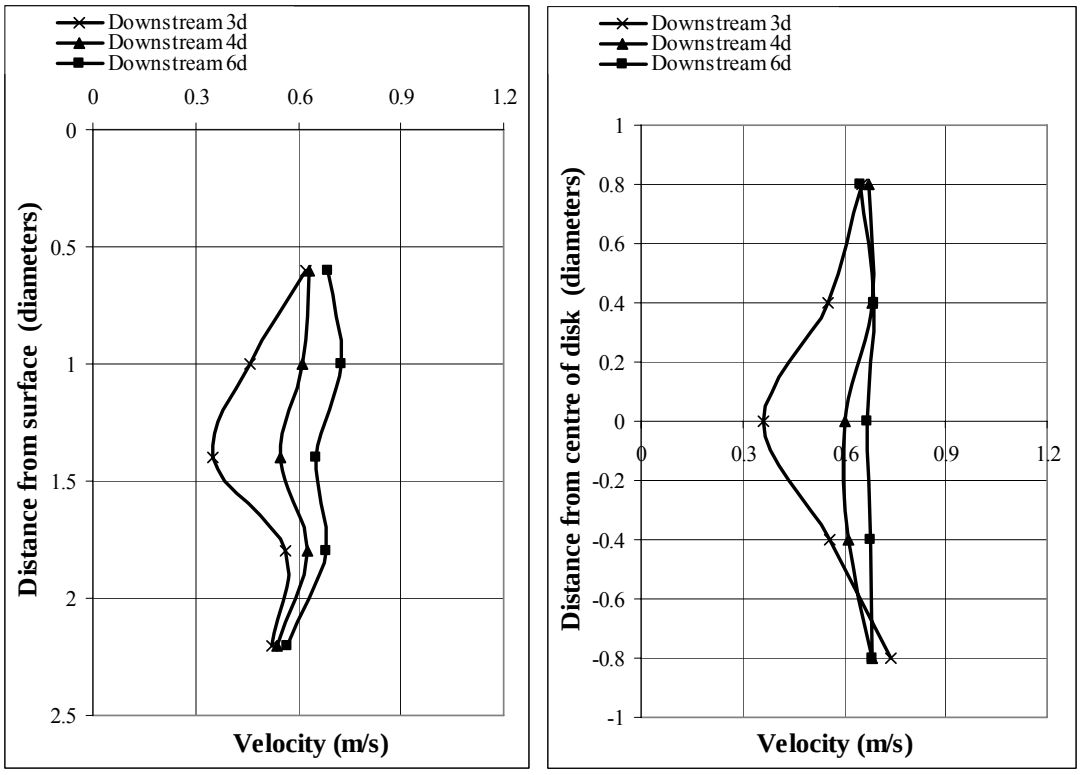

(a) (b)

Figure 4.18: Water velocity profiles behind the disk with 14% porosity in the vertical planes (a) and the horizontal planes (b) at downstream distances 3, 4 and 6 disk diameters

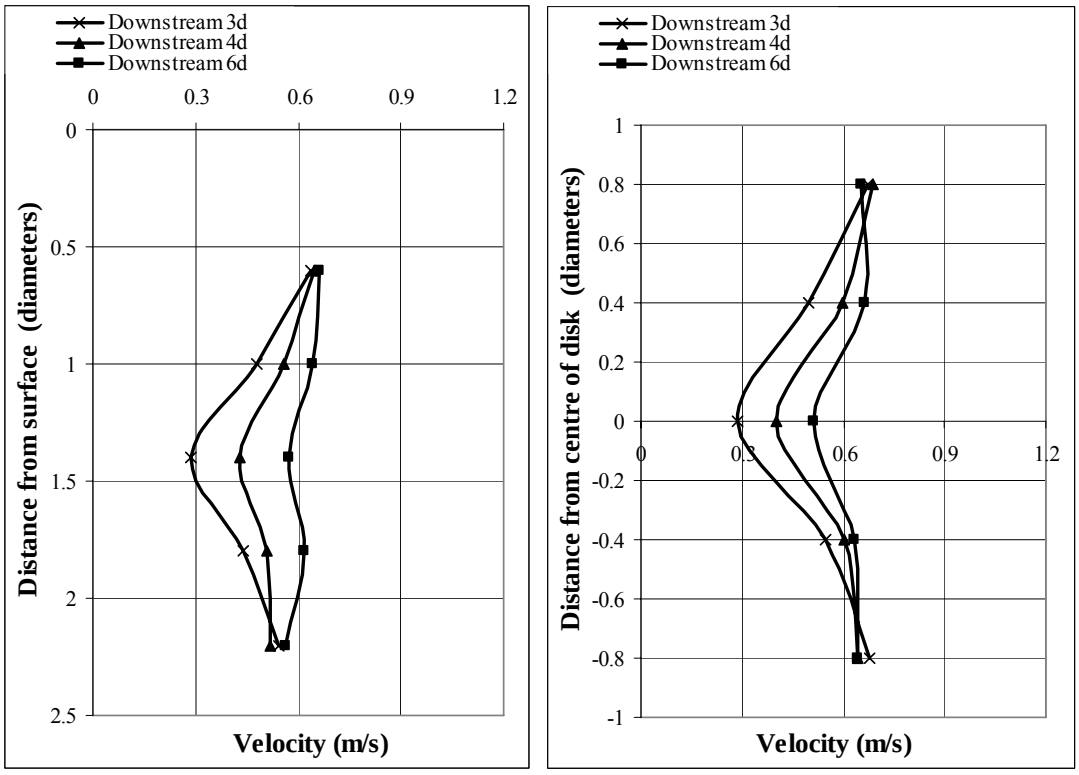

(a) (b)

Figure 4.19: Water velocity profiles behind the disk with 50% porosity in the vertical planes (a) and the horizontal planes (b) at downstream distances 3, 4 and 6 disk diameters

4.5 Conclusions

The first experimental study of energy extraction from tidal currents was carried out in moving water. Perforated disks were used to simulate the tidal current turbine operating at high tip speed ratios. The drag force acting on the disk and the velocity field in the wake were measured. The velocity profiles in the vertical and horizontal planes downstream the perforate disk show a Gaussian like distribution and the velocity behind the disk recovers gradually to the initial flow velocity. The variation in velocity profile shape with respect to downstream distance provides information about the development of the wake, which exhibits a similar tendency to the previous numerical results. On the other hand, the similarity between tidal turbine wakes and wind turbine wakes suggests that it is valid to consider, at least partially, the wakes behind tidal turbines as having similarities with those behind wind turbines. But it is important to keep in mind that the properties of water differ from air and the different operating environment for tidal current turbines and wind turbines. Turbulence in the wake is not measured in the experiment since more complicated instrumentation is difficult to apply under the present field conditions and will be in future work. Nonetheless, such an experimental study is the first attempt to examining simulated tidal current turbine performance in a natural water environment and provides a comparison to the numerical model and also to the second experiment, which was carried out under laboratory conditions.

Chapter 5

EXPERIMENTAL STUDY OF ENERGY EXTRACTION FROM TIDAL CURRENTS IN A TOWING TANK

Overview

The second experimental round was carried out in a towing tank under laboratory conditions and is described in this chapter. The experimental instrumentation employed in the first experiment were also used in the second experiment with a minor change, which is explained in section 5.1. The description of the towing tank is presented in section 5.2. The experimental procedures undertaken are stated in section 5.3. The experimental results and discussion are presented in section 5.4. Conclusions are given in section 5.5.

5.1 Experimental Instrumentation

A revised version of datascan software was adopted for data acquisition. It is more user-friendly and convenient to operate compared to the 'Recorder' used in the first programme of test, for example, the number of data that has been recorded can be

monitored on the computer screen directly. All other experimental instrumentation applied in the first experiment was also used in the second experiment.

5.2 Test Facility

The second experiment was carried out in a towing tank in order to compare the effects of flowing and still water on the performance of a tidal current turbine. Towing tanks are extensively utilized for scale model tests such as ships and submarines under controlled conditions. During the test, the model and measurement devices are towed through a large body of stagnant water. Therefore, it has the advantage of requiring much less power to achieve the desired test flow speed by moving the model rather than driving a large volume of water. In addition, towing tanks provide an ideal experimental condition, since the incoming flow has an extremely low turbulence level [122]. The second experimental programme in the present study was conducted in a towing tank located at the Acre Road Hydrodynamics Laboratory of the University of Glasgow and Strathclyde and is shown in Figure 5.1. It has a total lengthen of 70 m with a rectangular cross section of 4.6 m (width) × 2.4 m (depth) and a wavemaker is installed at one end of the tank. A self propelled towing carriage is mounted across the tank, mounted on rails at the side of the towing tank, and is used to pull the test disk and measurement instrumentation through the water at steady speeds. The tow carriage is displayed in Figure 5.2. The height of tow carriage above water could be effectively adjusted. The carriage speed can be measured as part of the control system of the drive, using encoders on the motors. A pulse counter converts the signal to an analogue voltage,

which can be logged by the carriage-based data acquisition system. The accuracy of towing speed is estimated to be within 1%. The maximum towing speed is 5 m s^{-1}.

Figure 5.1: The water towing tank

Figure 5.2: The towing carriage on the tank [123]

5.3 Procedures

The second experimental programme was performed during December, 2006. In the experiment, two U-shaped brackets were tightly clamped on the towing carriage and were used to carry the two middle aluminium bars detached from the support frame. Care was taken to ensure that the perforated disk and the pitot probe rake were perpendicular to the incoming flow so as to obtain symmetric inflow conditions. They were fixed on the middle bars, which were in exactly the same arrangement for the first experiment. The nearest distance from the centre of the test disk to the side walls of tank was 1600 mm. The blockage ratio was 0.4% in the experiment so that the blockage effect was ignored. At the start of experiment, water in the tank was quiet and the freestream turbulence was effectively zero.

The pitot probe rake was attached on the middle bars first and was towed through the undisturbed water at predetermined velocities to simulate a uniform current. The velocities measured by the pitot probe rake were used to verify the accuracy of the pitot probes and agreement was found to within 0.03 m s^{-1} at an average speed equal to the towing speed of 0.76 m s^{-1}. Then the perforated disk was placed in position on the middle bars. Each disk was tested at two different speeds: 0.76 and 1.26 m s^{-1}. Because of time constraints, only the velocity fields at $3d$ and $4d$ downstream from the disk were measured (d is the diameter of test disk). During each run, the datascan recorded the outputs from the pitot probes approximately 30 seconds in advance of the towing carriage starting to move. The data continued to be logged to the laptop until a few seconds after the towing carriage was braked and completely stopped. The towing carriage was then driven back to the starting point and prepared for the

next experimental run. A 3-5 minute break between two consecutive runs was taken, allowing the water to calm down.

In order to improve comparison with the experimental results gained in the water channel, turbulence was introduced into the towing tank by means of a wooden grid attached to the front of the carriage [124]. The turbulence-generating grid consisted of an array of 19 mm square bars, which were arranged in a checkerboard pattern with a mesh size of 163 mm centre to centre spacing. The mesh area was 5 times the test disk area with a 250 mm diameter, and the solidity, calculated as the ratio of solid area of the wooden bars to total area of the grid, was 0.25. Although a low solidity was used, the grid still showed the resistance to incoming flow. A towing speed of 0.76 m s^{-1} was used firstly, which is the same as the water speed in the water channel, and however the water speed behind the wooden grid was found being significantly reduced. Thus, the towing speed was increased gradually until 1.26 m s^{-1}. The water speed obtained behind the wooden grid and at the hub height of test disk was 0.8 m s^{-1}, which was close to 0.76 m s^{-1}. Therefore, the grid Reynolds number $R_{eM} = \frac{MU_\infty}{\nu}$, based on the mesh size M and the freestream velocity U_∞, was 1.35×10^5, which was relatively large to ensure a fully developed turbulence initial state [125]. The measurement positions were located at 2410 mm ($\approx 15M$) and 2660 mm ($\approx 16M$) downstream from the grid, where the grid turbulence became homogeneous [126]. Figure 5.3 showed the overall experimental setup for the measurements with the turbulence-generating grid attached. Total experimental runs that had been carried out were given in Appendix E.

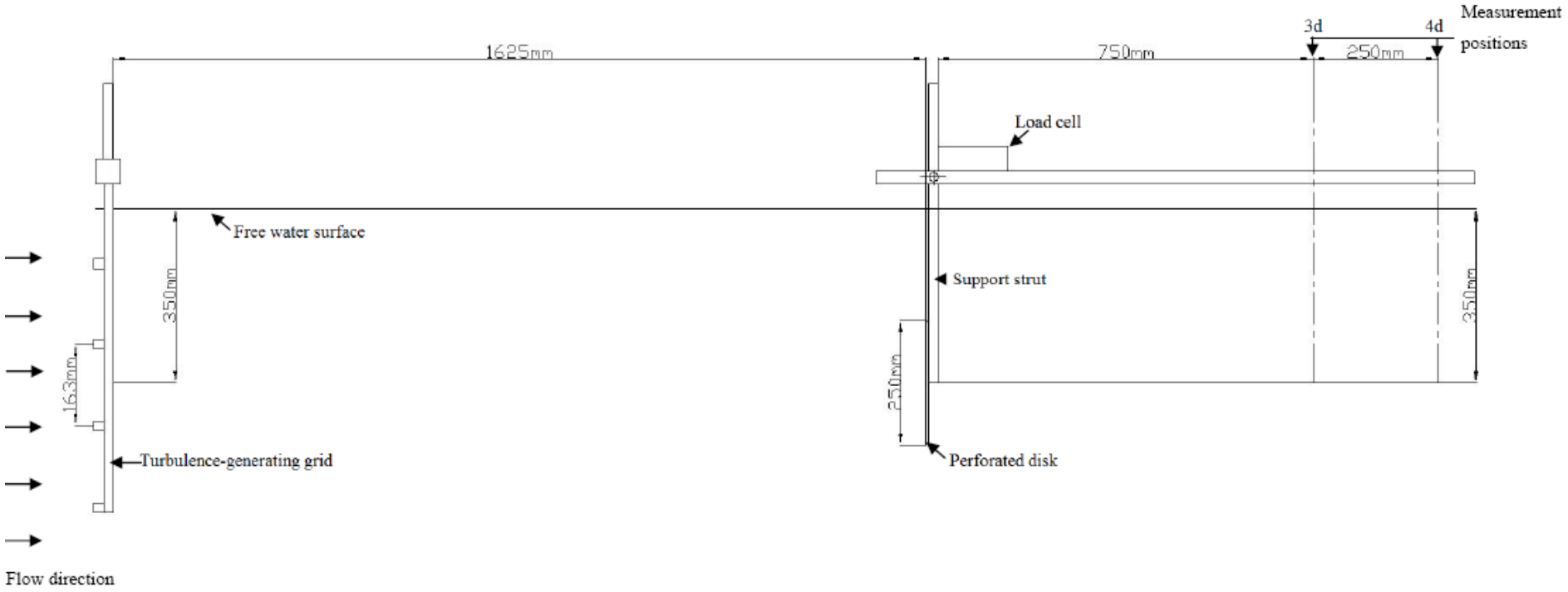

Figure 5.3: A schematic overview of the experimental setup in the towing tank

5.4 Results and Discussion

A typical "velocity time history" of towing carriage during a test run included three phases: acceleration from rest, constant velocity and deceleration to rest. Therefore, the offsets for each pressure transducer and load cell were obtained by averaging the data that were acquired a few seconds before the towing carriage moved. The data, which were recorded after the steady state motion was reached (after about 4 seconds in each run), were averaged and used for the water velocity and the drag force calculations.

The drag force and the drag force coefficient for the test disk are shown in Table 5.1. As expected, it is found that the larger drag force acts on the disk with the less porosity and results in a higher drag force coefficient. This result suggests that increasing the solidity of tidal current turbine blade or the number of turbine blades may lead to a higher turbine power production, especially as the turbine is running at lower tip speed ratios. This is not too surprising as low speed, high solidity turbines have traditionally been used for mechanical drive purposes, such as cereal grinding and water pumping. Also, it is noticed that the drag force increases with incoming flow speed. At a freestream velocity of 1.26 m s^{-1}, the drag force is about 2.8 times the force achieved at a freestream velocity of 0.76 m s^{-1} for both test disks in this experiment, because more energy can be lost as the water moving through the test disk at a faster speed. The velocity profiles measured downstream of the test disk have shown the same pattern observed in the results from water channel experiment except that an area of recirculating flow is identified at $3d$ downstream of the disk with 14% porosity, but this area disappears when the ambient turbulence level is

increased. The asymmetry of velocity profile in the vertical plane is still visible in the experimental results. More specifically, the recovery of velocity measured at the point close to the free surface is significantly delayed, which may be caused by that measuring point being located in the wake of the strut behind the test disk. This outcome confirms the influence of the presence of the strut on the measurements. In addition, there is a portion of a bulk solid material at the top edge of the perforated disk with 14% porosity, due to the distribution of holes in the disk. Therefore, the asymmetry of wake velocity profiles in the vertical planes downstream of the disk with 14% porosity is more apparent. The velocity profiles are displayed in Figure 5.4-5.7. Figure 5.8-5.9 displayed the wake velocity profiles measured behind the test disks with the grid-generated freestream turbulence. In order to identify the effect of ambient turbulence on the wake recovery, the results of the normalised mean velocity deficit profiles downstream of test disk are compared between two experimental conditions that have been defined: (1) zero freestream turbulence and a velocity of 0.76 m s^{-1}; (2) nonzero freestream turbulence and a velocity of 0.80 m s^{-1}. It was found that there is a general tendency, for both test disks, that the decay of the velocity deficit within the wake is accelerated by increasing the freestream turbulence level (See Figure 5.10-5.11), although the drag force, in the case where the turbulence-generating grid is attached, is more than 30% larger than that measured in the flow with zero freestream turbulence.

Test disk	Averaged velocity at hub height of disk (m s^{-1})	Area of disk (m^2)	Averaged drag force (N)	Drag force coefficient C_D
Without the turbulence generating grid upstream from the test disk				
(a) Towing speed $U_\infty = 0.76$ m s^{-1}				
Disk with 14% porosity	0.730	0.049	12.558	1.000
Disk with 50% porosity	0.730	0.049	8.550	0.700
(b) Towing speed $U_\infty = 1.26$ m s^{-1}				
Disk with 14% porosity	1.210	0.049	36.160	1.000
Disk with 50% porosity	1.210	0.049	24.000	0.700
With the turbulence generating grid upstream from the test disk				
Towing speed $U_\infty = 1.26$ m s^{-1}				
Disk with 14% porosity	0.800	0.049	17.464	1.114
Disk with 50% porosity	0.800	0.049	11.408	0.728

Table 5.1: Results of drag force and drag force coefficient from the second experiment

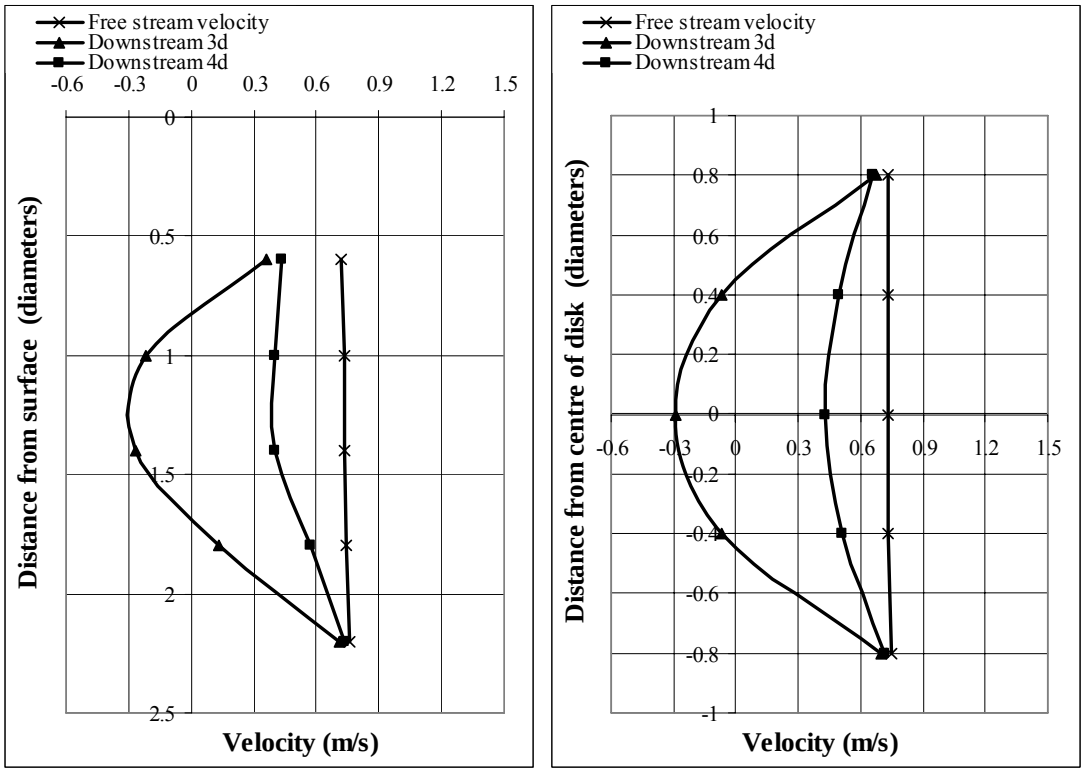

(a) (b)

Figure 5.4: Water velocity profiles behind the disk with 14% porosity in the vertical planes (a) and the horizontal planes (b) at downstream distances 3 and 4 disk diameters
(zero freestream turbulence and a freestream velocity of 0.76 m s^{-1})

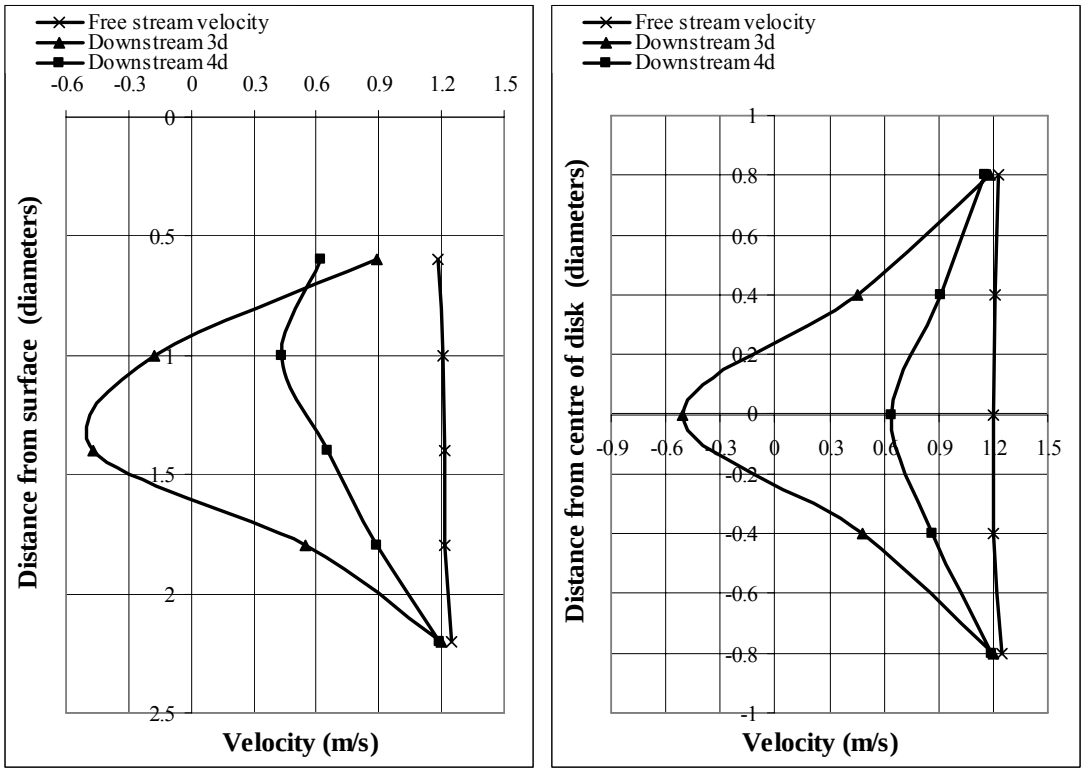

(a) (b)

Figure 5.5: Water velocity profiles behind the disk with 14% porosity in the vertical planes and the horizontal planes (b) at downstream distances 3 and 4 disk diameters
(zero freestream turbulence and a freestream velocity of 1.26 m s^{-1})

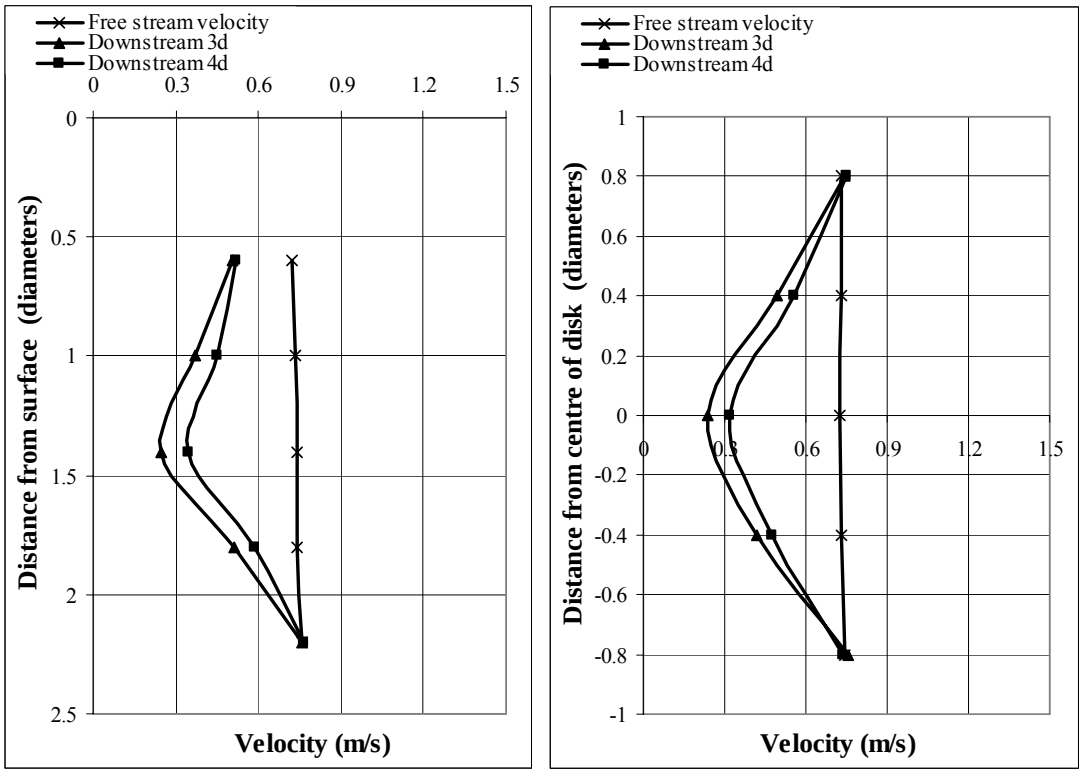

(a) (b)

Figure 5.6: Water velocity profiles behind the disk with 50% porosity in the vertical planes (a) and the horizontal planes (b) at downstream distances 3 and 4 disk diameters
(zero freestream turbulence and a freestream velocity of 0.76 m s^{-1})

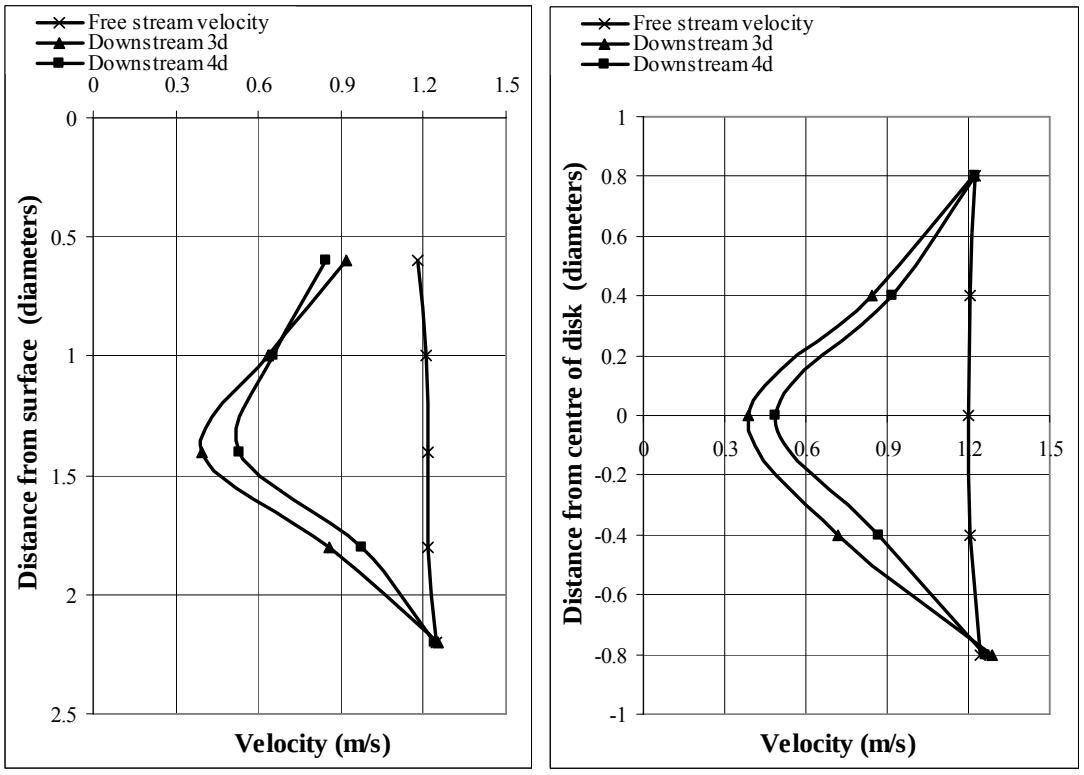

(a) (b)

Figure 5.7: Water velocity profiles behind the disk with 50% porosity in the vertical planes (a) and the horizontal planes (b) at downstream distances 3 and 4 disk diameters
(zero freestream turbulence and a freestream velocity of 1.26 m s^{-1})

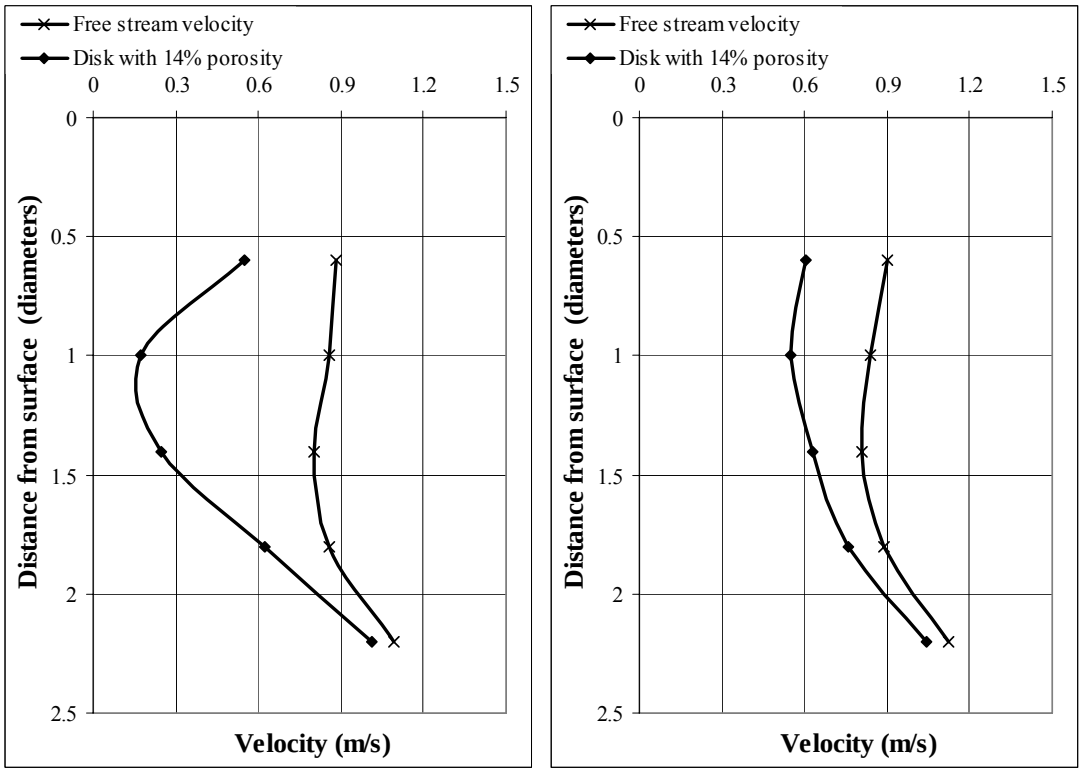

Figure 5.8 (i): Water velocity profiles behind disk with 14% porosity in the vertical plane at downstream distances 3 (a) and 4 (b) disk diameters (nonzero freestream turbulence and a freestream velocity of 0.8 m s^{-1})

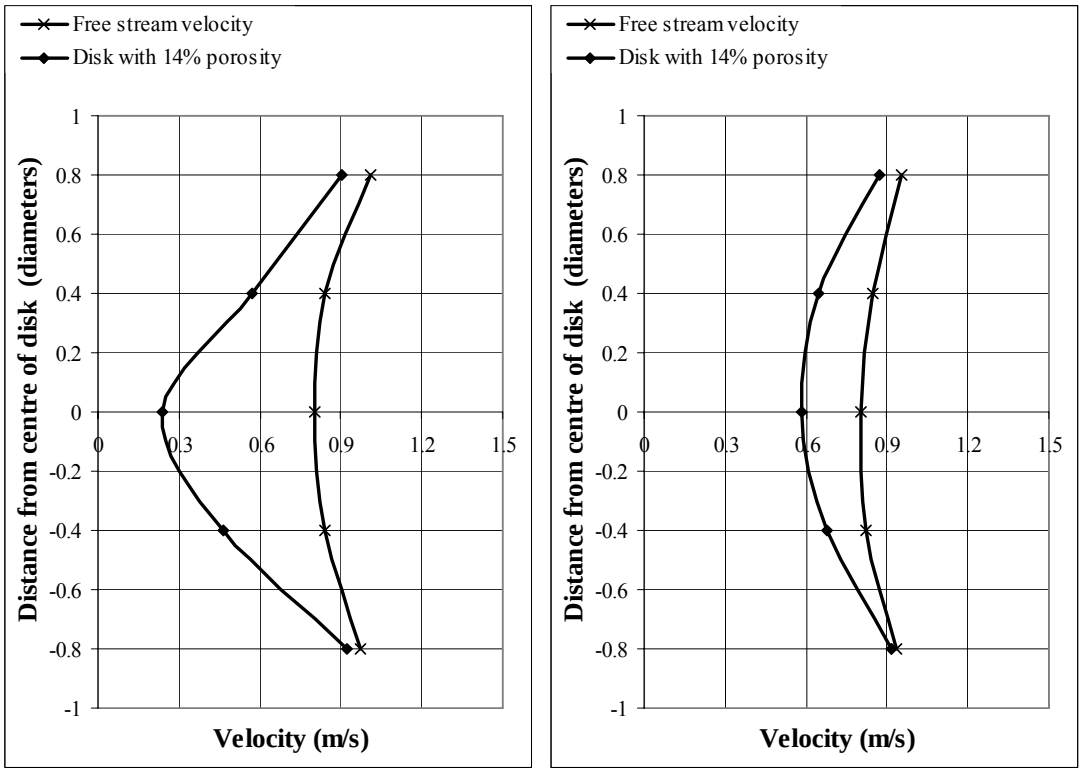

(a) (b)

Figure 5.8 (ii): Water velocity profiles behind the disk with 14% porosity in the horizontal plane at downstream distances 3 (a) and 4 (b) disk diameters
(nonzero freestream turbulence and a freestream velocity of 0.8 m s^{-1})

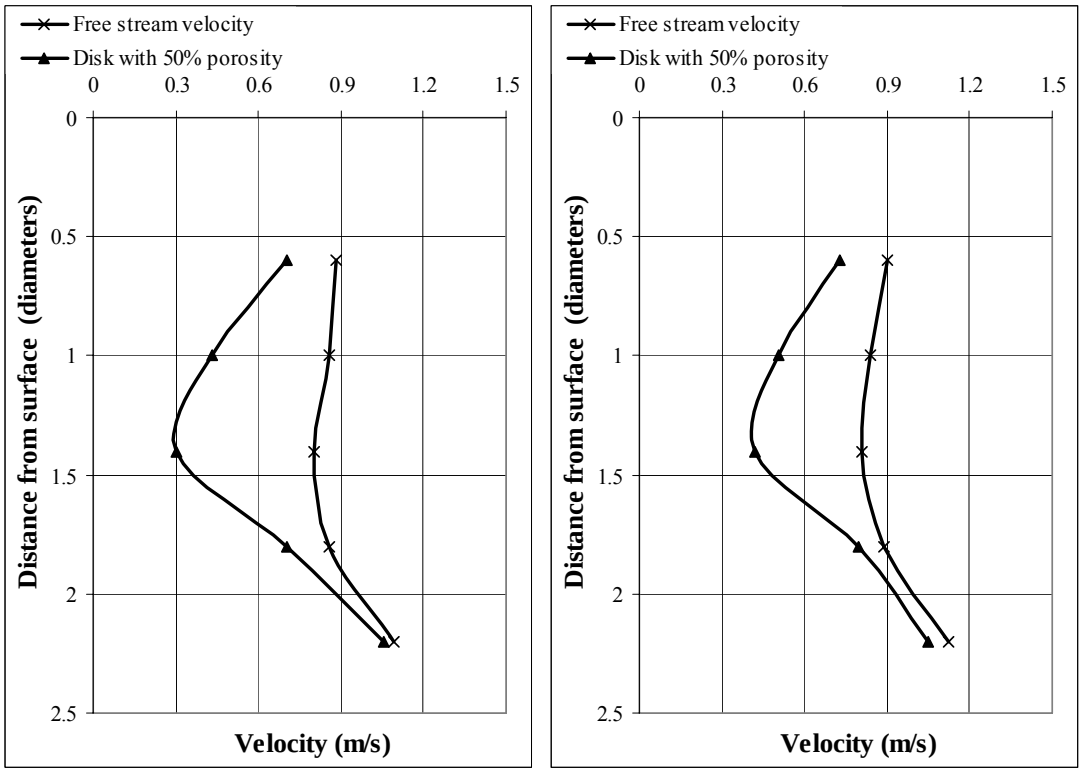

Figure 5.9 (i): Water velocity profiles behind the disk with 50% porosity in the vertical plane at downstream distances 3 (a) and 4 (b) disk diameters (nonzero freestream turbulence and a freestream velocity of 0.8 m s^{-1})

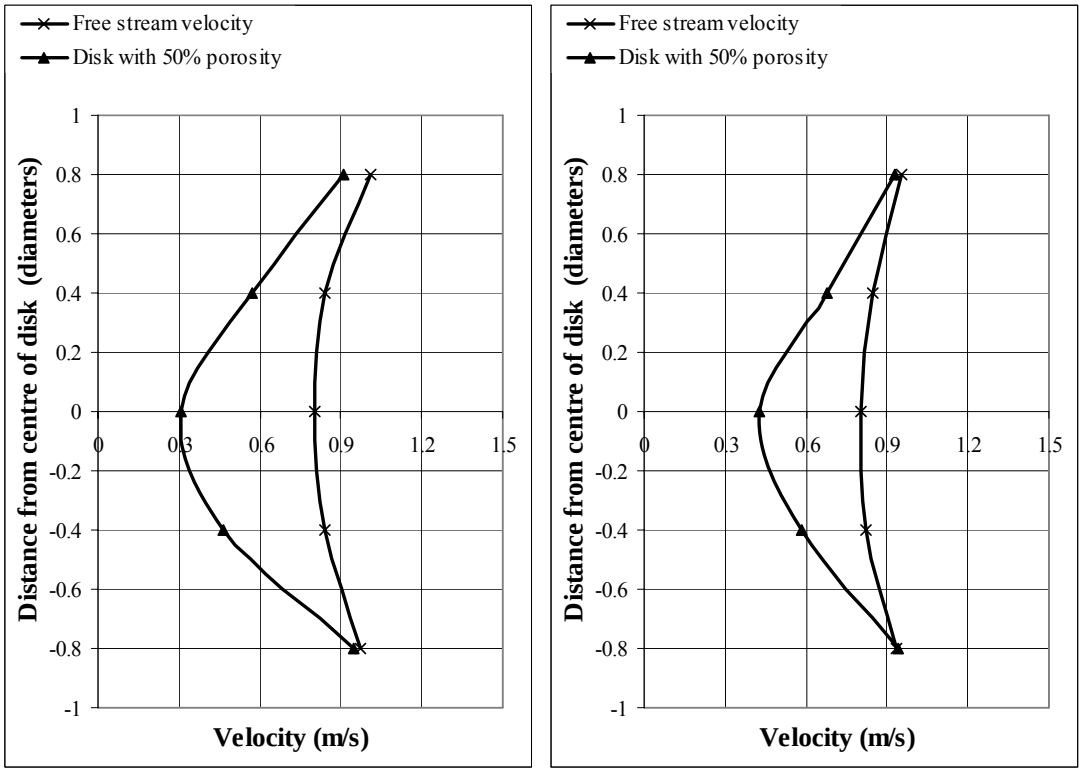

Figure 5.9 (ii): Water velocity profiles behind the disk with 50% porosity in the horizontal plane at downstream distances 3 (a) and 4 (b) disk diameters
(nonzero freestream turbulence and a freestream velocity 0.8 m s^{-1})

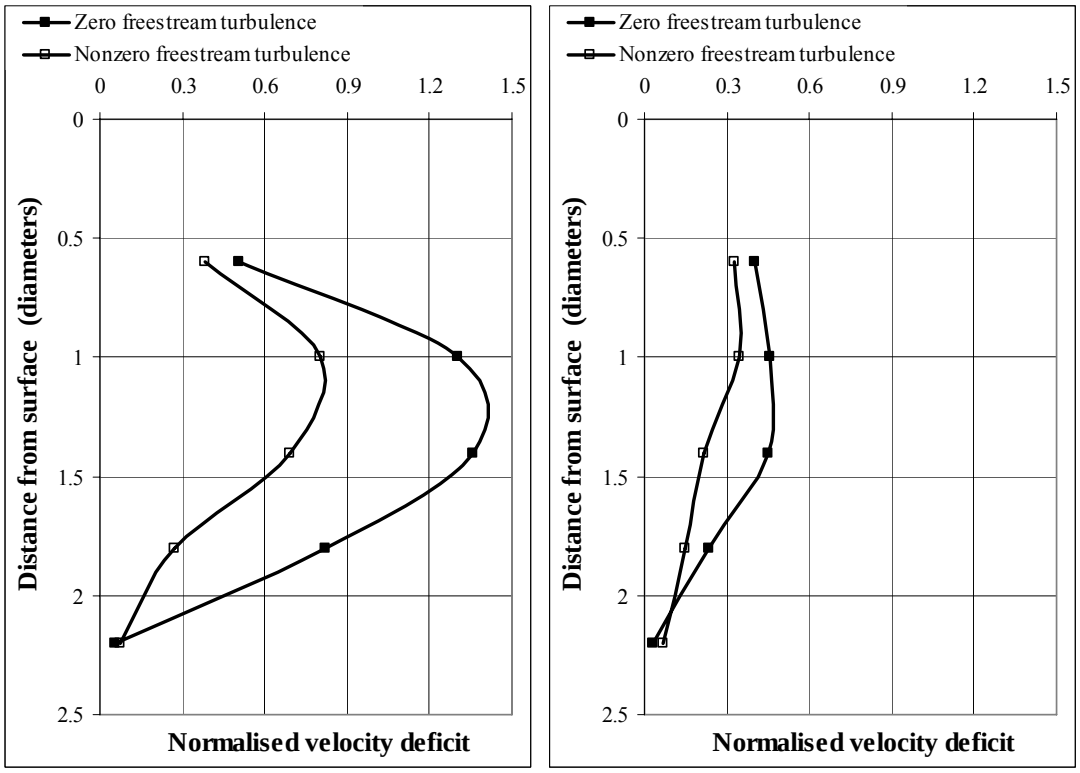

Figure 5.10 (i): Comparison of normalised mean velocity deficit profiles behind the disk with 14% porosity in the vertical plane at downstream distances 3(a) and 4 (b) disk diameters for different freestream turbulence levels

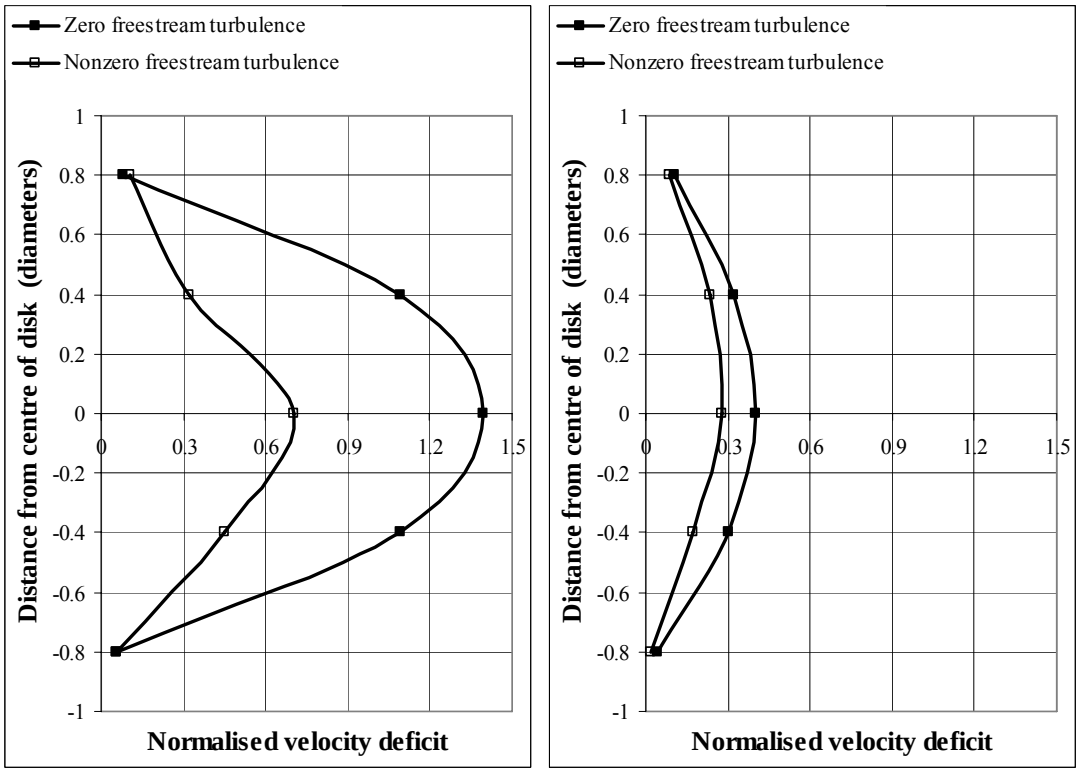

Figure 5.10 (ii): Comparison of normalised mean velocity deficit profiles behind the disk with 14% porosity in the horizontal plane at downstream distances 3 (a) and 4 (b) disk diameters for different freestream turbulence levels

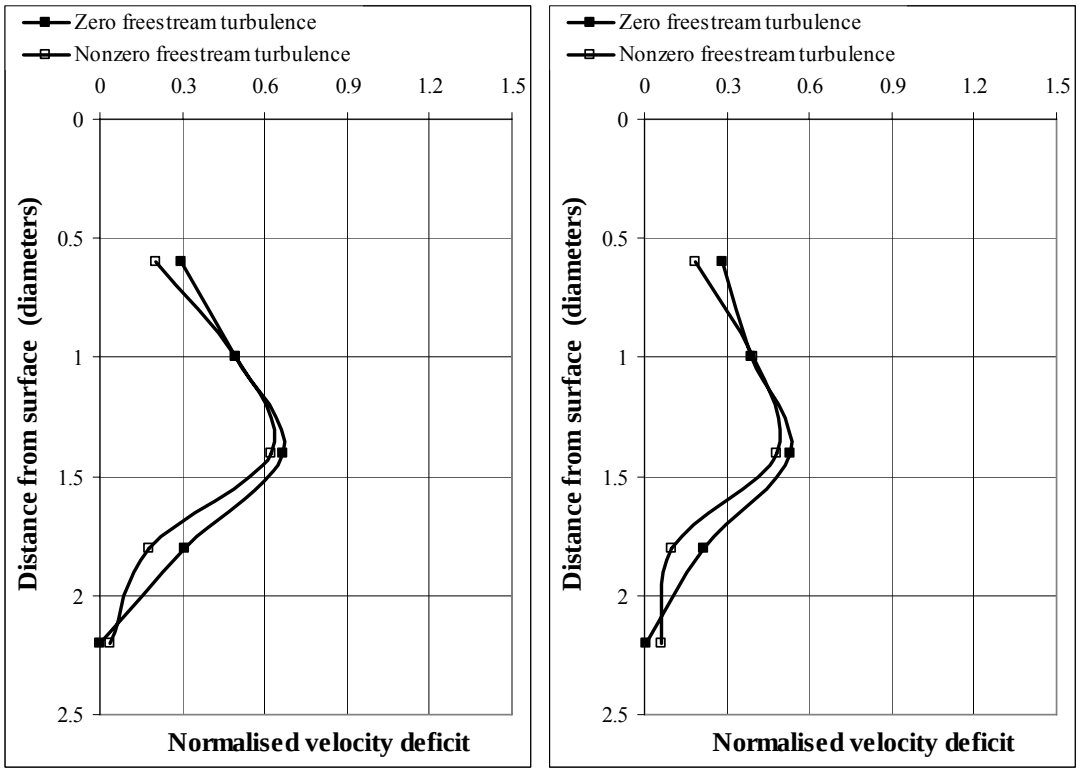

(a) (b)

Figure 5.11 (i): Comparison of normalised mean velocity deficit profiles behind the disk with 50% porosity in the vertical plane at downstream distances 3(a) and 4 (b) disk diameters for different freestream turbulence levels

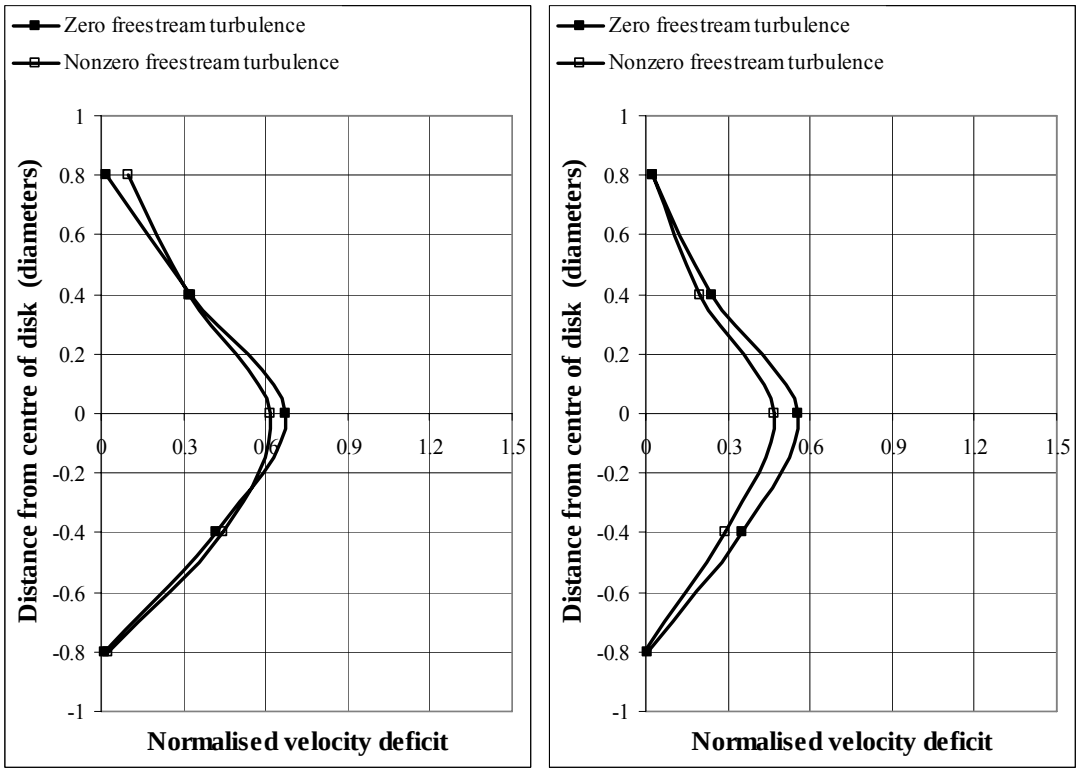

Figure 5.11 (ii): Comparison of normalised mean velocity deficit profiles behind the disk with 50% porosity in the horizontal plane at downstream distances 3 (a) and 4 (b) disk diameters for different freestream turbulence levels

5.5 Conclusions

The second experimental study of energy extraction from tidal currents by using a simulated tidal current turbine was conducted in still water under laboratory conditions. It is possible to investigate the influence of varying experimental parameters such as water speed and freestream turbulence level on the energy extraction from water, because of a closely specified test environment in a towing tank. In all of the experimental results, the velocity profile in the wake behind the test disk were generally consistent with a Gaussian-like shape and the velocity defect recovered with downstream distance, but the velocity profile in the vertical plane is highly asymmetric. The freestream turbulence level was found to have effects on the wake development and the experimental findings qualitatively coincide with the numerical predictions. Nevertheless, turbulence intensity at measurement positions was not known and thus the effect of free stream turbulence on wake growth was difficult to be quantified, although the CFD method had been used at the beginning of the experiment with an attempt to simulate the turbulence behind the turbulence-generating grid and was not completed at the end of this study due to the heavy computation load involved.

Chapter 6

COMPARISONS

Overview

Energy extraction from tidal currents has been investigated numerically and experimentally in the previous chapters. In this chapter, comparisons are made among the results gained. The experimental results obtained under different testing conditions are compared in section 6.1. Numerical results are compared with experimental data in section 6.2. An uncertainty analysis is provided in section 6.3.

6.1 Comparisons between Experimental Results

The experimental study of energy extraction from tidal currents was carried out in a flowing water channel and in a towing tank, using a simulated tidal current turbine. The normalised mean velocity deficit profiles measured in the two experiments were compared with each other in order to identify the influence of different testing conditions on the laboratory study of wake development behind a model tidal current

turbine. The wake profiles measured in the horizontal planes at downstream 3 d and 4 d are chosen for comparison in preference to vertical profiles to avoid effects of the mean velocity gradient in the turbulent channel flow. The results obtained with a turbulence-generating grid attached in the towing tank tests were used for the comparison, since they are considered to be measured under freestream turbulence conditions. Table 6.1 shows the experimental conditions for the two experiments being compared. The comparison results for the disk with 14% porosity are displayed in Figure 6.1. In the figure, the profiles compare well in terms of profile shape. The normalised centreline velocity deficit (given by the mean centreline velocity defect in the wake normalized by the freestream velocity), in the flowing water tank test at 3 d downstream is 75%, and at 4 d downstream is 73%, of that in the towing tank test. This is reasonable, since the drag force of 17.5 N acting on the disk in the towing tank test is greater than the force of 14.1 N measured in the water channel test and thus indicates more energy loss. For the disk with 50% porosity, the comparisons are more favourabe because of the similar drag force values: 10.2 N in the water channel and 11.4 N in the towing tank. Therefore, the distribution of the forms of the wake profiles shows the closest agreement with each other, as presented in Figure 6.2. The difference between the turbulence in the natural channel and in the towing tank may be a factor in explaining the discrepancy between the two wake profiles compared. For both test disks, the profiles obtained in the towing tank tests are more symmetric around the wake centreline and this result is likely due to the more symmetric inflow conditions achieved in the towing tank under controllable conditions.

Experiment	Perforated disk	Drag force (N)	Diameter of disk (mm)	Submerged water depth (mm)	Free stream velocity ($m\ s^{-1}$)
Experiment in the water channel (nonzero free stream turbulence)	Disk with 14% porosity Disk with 50% porosity	14.111 10.199	250	350	0.76
Experiment in the towing tank (nonzero free stream turbulence)	Disk with 14% porosity Disk with 50% porosity	17.464 11.408	250	350	0.8

Table 6.1: Two experimental conditions

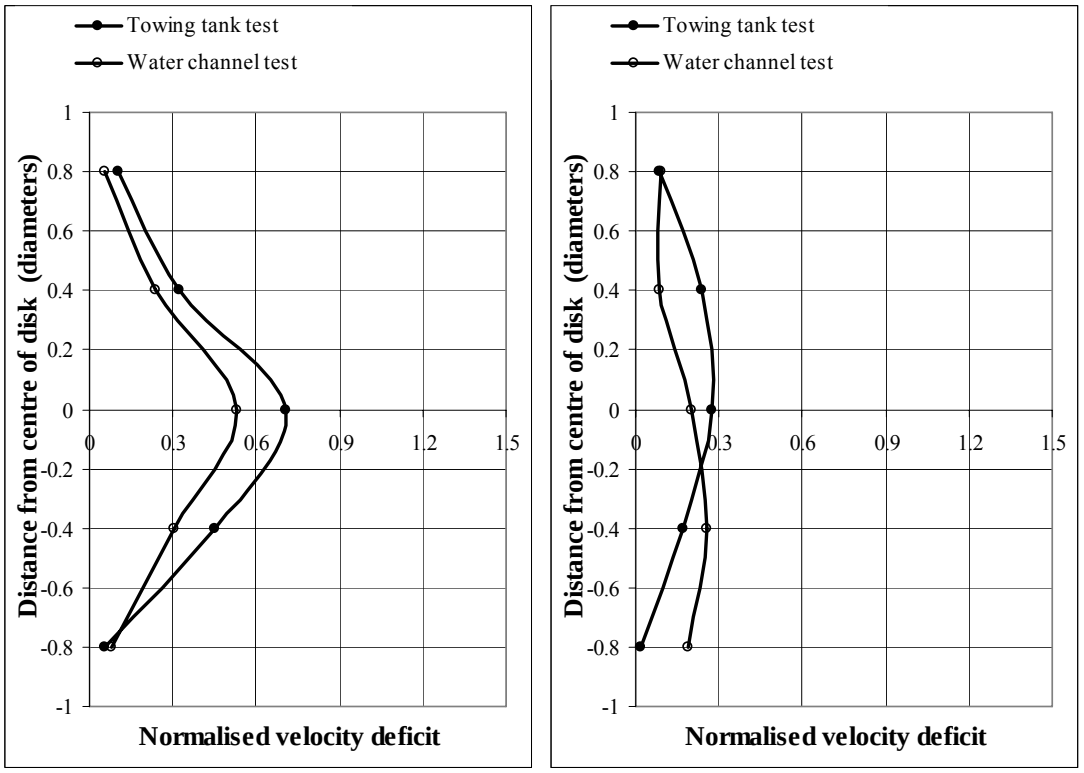

Figure 6.1: Comparisons of the normalised mean velocity deficit profiles measured in the water channel test and the towing tank test at downstream distances 3(a) and 4 (b) disk diameters for the disk with 14% porosity

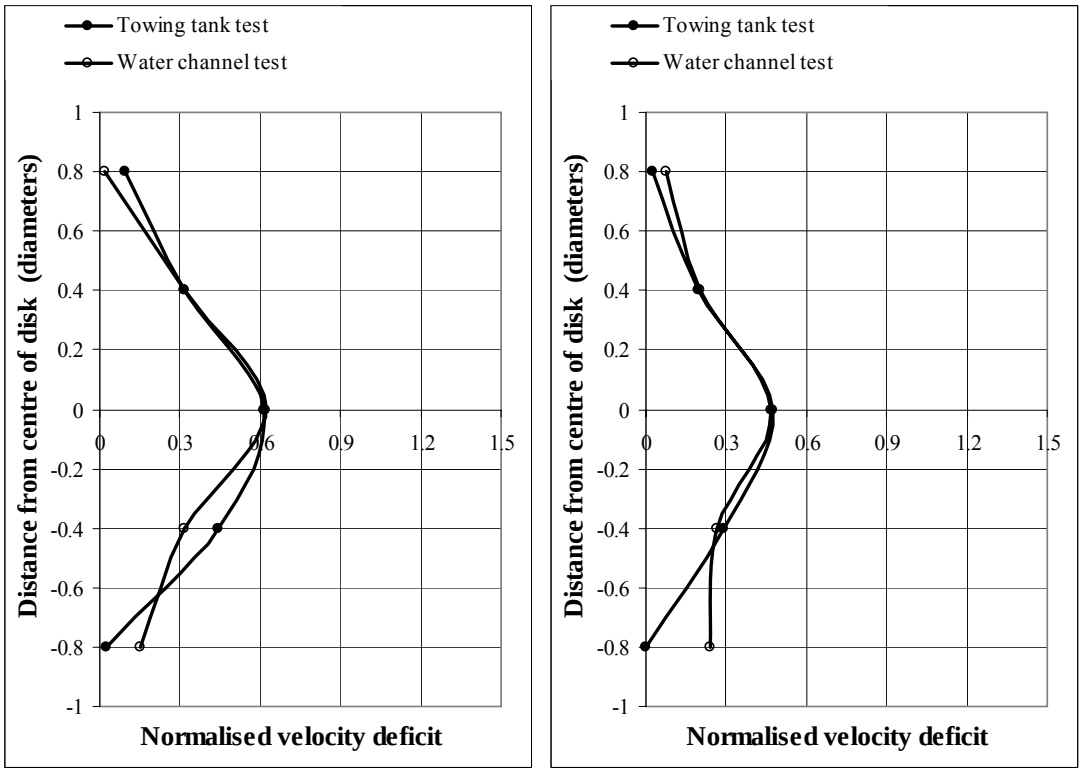

Figure 6.2: Comparisons of the normalised mean velocity deficit profiles measured in the water channel test and the towing tank test at downstream distances 3 (a) and 4 (b) disk diameters for the disk with 50% porosity

6.2 Comparisons between Experimental and Numerical Results

The experimental data was also used for the validation of the numerical model that was established, with the aim of providing predictions of tidal turbine wake development. For the purpose of precise comparison, a new three-dimensional numerical model was set up to match the experimental conditions in the towing tank. A 250 mm × 250 mm square region was defined as a porous media zone in FLUENT to simulate the perforated disk and the distance from the centre of the porous media to the water surface was 350 mm. The support strut for perforate disk which was used in the experiments was simulated in the numerical model at first, but it was found that significant computing resources and large computational time were required. Finally, the support strut was omitted from the numerical model. In contrast to the previous numerical model described in Chapter 2, in which a large inertial resistance coefficient $C_{2i,j}$ for the actuator disk was intentionally defined in order to identify the effects of large-scale energy extraction from moving water, the inertial resistance coefficient was modified using the drag force coefficients divided by the thickness of the test disks, since the inertial resistance coefficient was a loss coefficient per unit length along the flow direction in the porous medium model. Thus, they were 200 m^{-1} for the perforated disk with 14% porosity and 140 m^{-1} for the perforated disk with 50% porosity respectively. All other settings in the numerical model remained unchanged. In addition, the main inlet boundary condition in FLUENT needs the input parameters turbulence intensity and turbulent viscosity ratio to be explicitly defined. However, free stream turbulence was not able to be measured during experiments in the water flow channel, because of the present

instruments applied. Therefore, the values of input parameters needed for the numerical simulation were set according to the experimental test carried out under uniform incoming flow condition in the towing tank with a freestream velocity of 0.76 m s^{-1} and 1.26 m s^{-1}, but approximately zero freestream turbulence. Simulation conditions for the simulation of experiments in the towing tank were given in Table 6.2.

The normalised velocity deficit profiles in the central horizontal plane at downstream 3 d and 4 d of disk are compared with numerical and experimental results in Figure 6.3 - 6.6, to avoid the influence of the strut on the velocity profiles in the vertical plane during the experimental measurements. The comparisons show that qualitative agreement in the development of wake profiles is generally good between the experimental results and numerical predictions. However, a significant discrepancy exists at a distance of 3 d downstream of disk with 14% porosity, where a recirculating flow region behind the disk was identified in the experiment but was not captured in the numerical model. This may be due to the fact that the porous media model in FLUENT is an added momentum sink and has ignored the physical geometry of the disk. Therefore, it is only an approximation to a real porous disk and it is not able to resolve the flow pattern at positions relatively close to the disk, where the flow is considerably influenced by the fluid-structure interactions, according to the FLUENT help line [127]. This is especially true for the disk with high solidity, which can generate more complex turbulent flow in the near wake region behind the disk. However, the comparisons do become more promising at 4 d downstream of the disk with 14% porosity and for the disk with 50% porosity. Generally, the centreline

velocity deficit in the wake is underestimated and the width of wake is much wider in the numerical results compared with the experimental data.

While the comparisons are qualitative, they help confirm the generic features of the wake downstream of a tidal current turbine and thus verify the validity of the proposed numerical model as a valuable tool for predicting wake development, which is a significant factor in determining the optimum distance between turbines in a tidal 'farm', thus improving the efficiency of energy production. Further improvements of the present numerical approach may be made by modifying the turbulence model applied. For instance, changing the constant value of C_μ used in the standard $k-\varepsilon$ model to a function of the average production to dissipation rate of turbulence kinetic energy, $C_\mu = f\left(\frac{\overline{P}}{\varepsilon}\right)$, for weak shear flows, as recommended by Rodi [70]. In addition, different turbulence models could be tested against more precise experimental data measured by using more sophisticated experimental devices like hot-wire anemometry and laser doppler anemometry, which can also investigate the turbulence characteristics in the wake.

Experiment	Perforated disk	Drag force coefficient	Diameter of disk (mm)	Submerged water depth (mm)	Tow carriage speed ($m\ s^{-1}$)
Experiment in the towing tank (zero free stream turbulence)	Disk with 14% porosity Disk with 50% porosity	1.00 0.7	250	350	0.76 1.26
Numerical model	Actuator disk	Inertial resistance coefficient ($1\ m^{-1}$)	Characteristic length of actuator disk (mm)	Submerged water depth (mm)	Free stream velocity ($m\ s^{-1}$)
3D model	Disk with 14% porosity Disk with 50% porosity	200 140	250	350	0.76 1.26

Table 6.2: Simulation conditions for the simulation of experiment in the towing tank

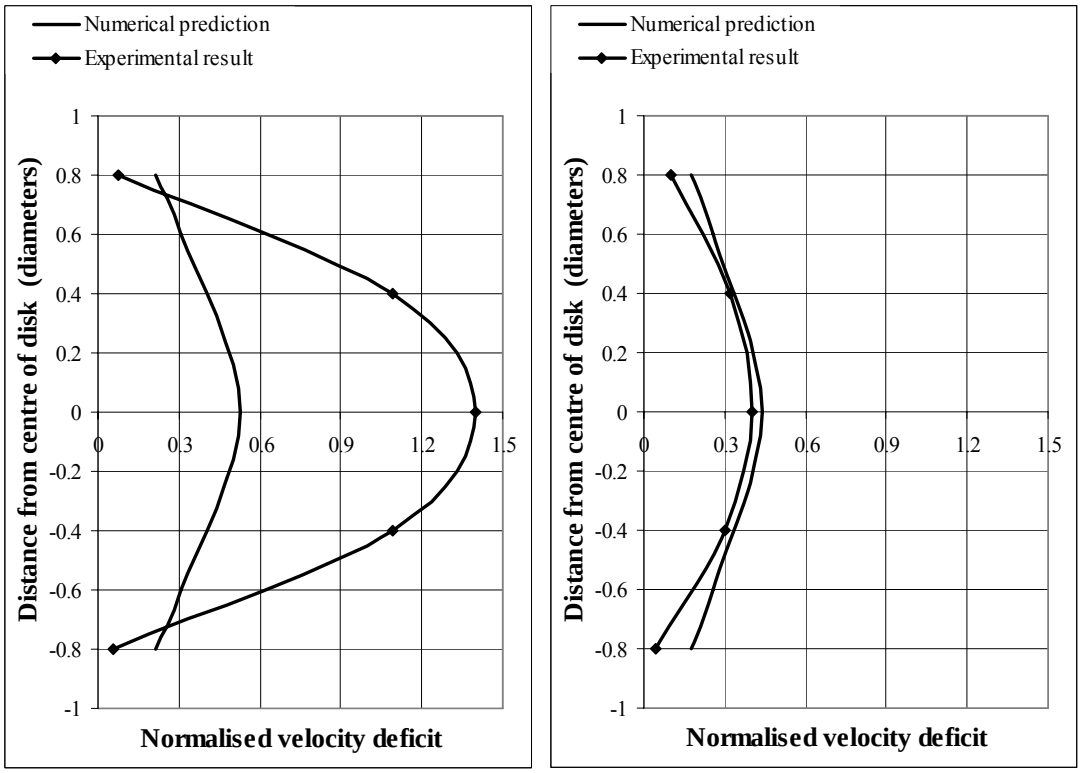

Figure 6.3: Comparisons of the normalised mean velocity deficit profiles measured in the towing tank test with the numerical prediction at downstream distances 3 (a) and 4 (b) disk diameters for the disk with 14% porosity (zero freestream turbulence and a freestream velocity of 0.76 m s^{-1})

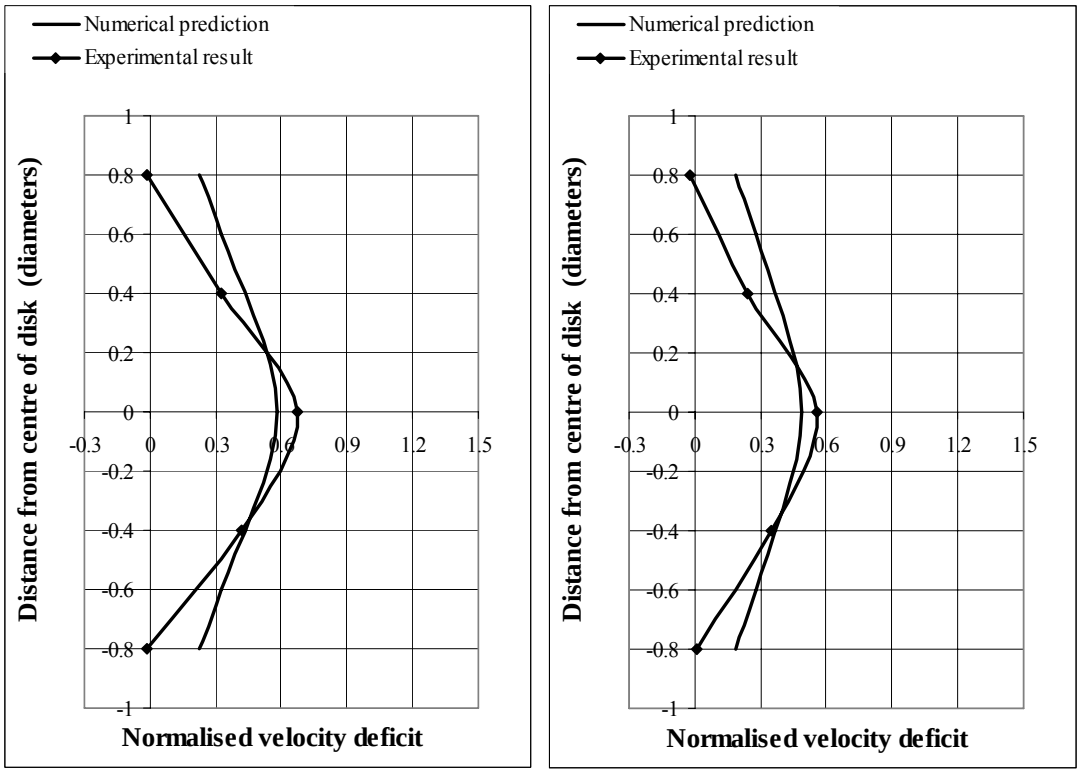

Figure 6.4: Comparisons of the normalised mean velocity deficit profiles measured in the towing tank test with numerical prediction at downstream distances 3(a) and 4 (b) disk diameters for the disk with 50% porosity (zero freestream turbulence and a freestream velocity of 0.76 m s^{-1})

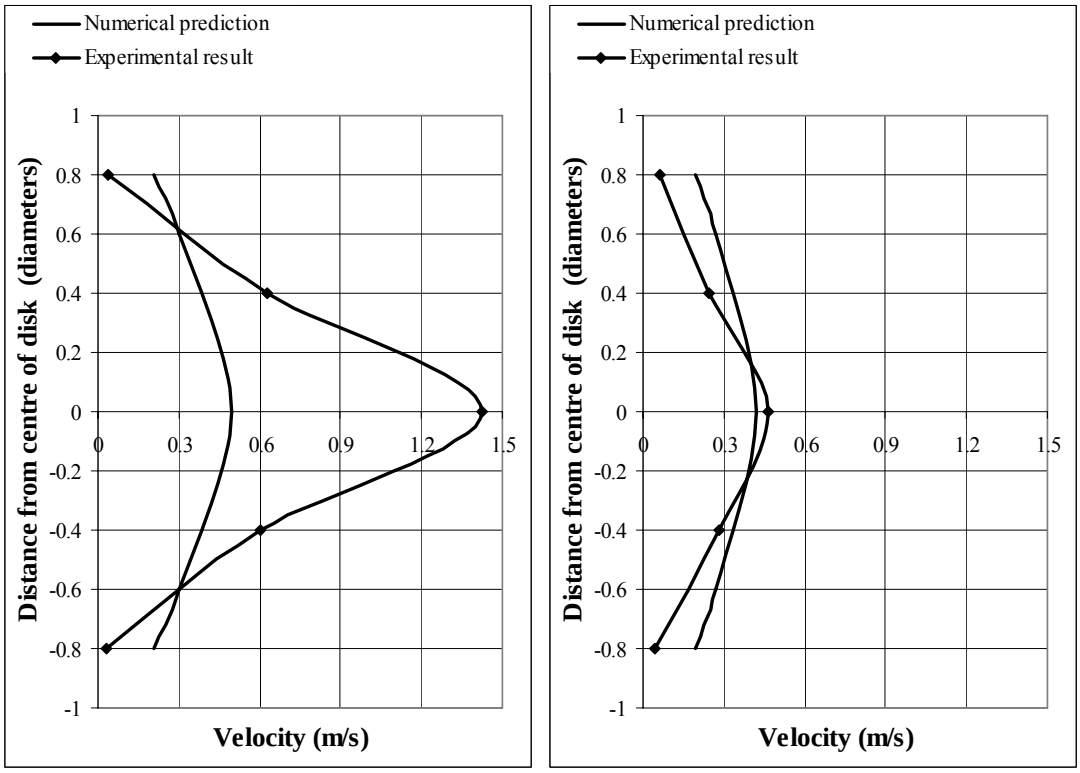

(a) (b)

Figure 6.5: Comparisons of the normalised mean velocity deficit profiles measured in the towing tank test with the numerical prediction at downstream distances 3 (a) and 4 (b) disk diameters for the disk with 14% porosity (zero freestream turbulence and a freestream velocity of 1.26 m s^{-1})

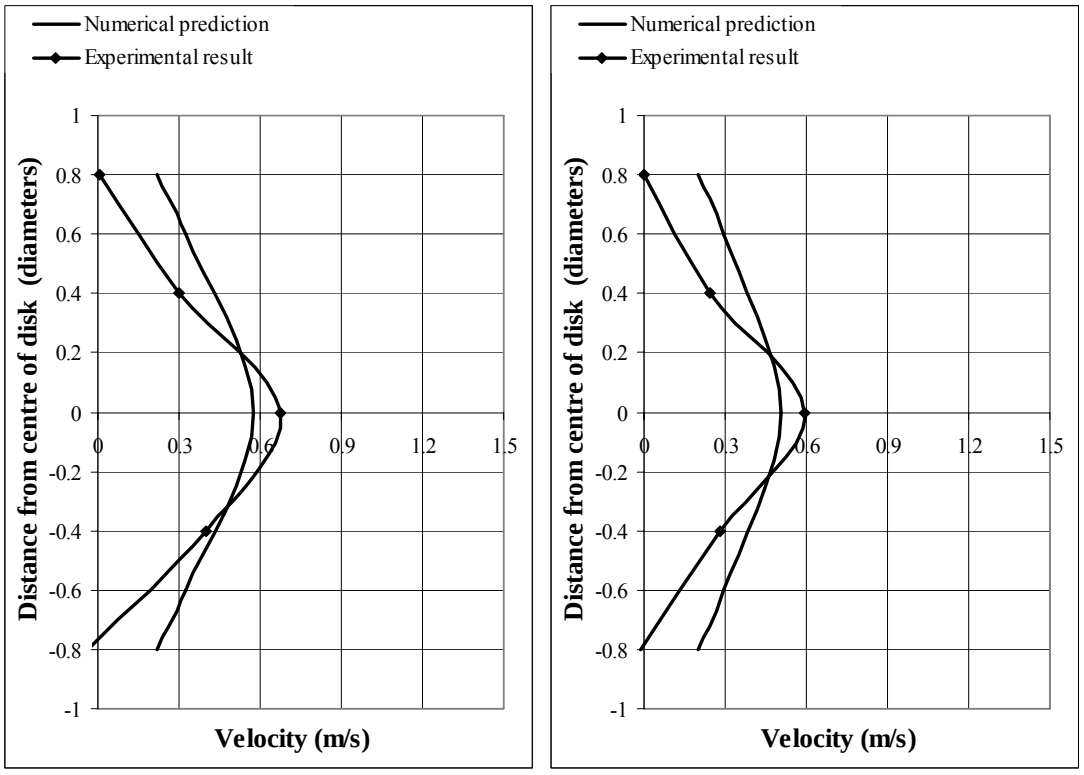

(a) (b)

Figure 6.6: Comparisons of the normalised mean velocity deficit profiles measured in the towing tank test with the numerical prediction at downstream distances 3 (a) and 4 (b) disk diameters for the disk with 50% porosity (zero freestream turbulence and a freestream velocity of 1.26 m s^{-1})

6.3 Uncertainty Analysis

In order to assess the confidence level for the experimental results obtained in the current study, uncertainty analysis is conducted using the methods suggested by Coleman [128]. The total error includes bias error and precision error. The bias error for the drag force D measurement (B_D) is estimated according to the manufacturer's specification for the load cell at 0.005 % of the applied load. The bias error (B_U) for the mean velocity measured by the pitot probe is decided by comparing the probe output with the known calibrated towing speed in the tow tank and is shown in Table 6.1.

Precision error occurs in repeated measurements, in which the measured results are not able to be exactly replicated. In all the experiments, a single measurement of the mean velocity was conducted at each position behind the disk, therefore the precision error for the measurement of wake velocity is not taken into account. However, since the drag force acting on the test disk was measured simultaneously with the velocity at each downstream position, multiple measurements of the drag force were regarded to have been made. Thus, the precision error (P_D) of measured drag force is evaluated by using equation (6.1) based on the Student's t-distribution [129].

$$P = \frac{tS}{\sqrt{N}} \tag{6.1}$$

where t is the student value and is affected by the number of measurements taken, S is the standard deviation of measured values and N is the number of measurements.

The drag force coefficient C_D of a test disk is calculated through the data reduction equation (6.2), in which D is the drag force, U_∞ is the freesteam velocity, ρ is the water density and d is the diameter of test disk.

$$C_D = \frac{D}{\frac{1}{8}\rho U_\infty^2 \left(\pi d^2\right)} \tag{6.2}$$

Therefore, the bias error $\left(B_{C_D}\right)$ and precision error $\left(P_{C_D}\right)$ of C_D are calculated separately using the error propagation equations (6.3) and (6.4).

$$B_{c_D} = \sqrt{\left(\frac{\partial C_D}{\partial D} B_D\right)^2 + \left(\frac{\partial C_D}{\partial U_\infty} B_{U_\infty}\right)^2} \tag{6.3}$$

$$P_{c_D} = \sqrt{\left(\frac{\partial C_D}{\partial D} P_D\right)^2 + \left(\frac{\partial C_D}{\partial U_\infty} P_{U_\infty}\right)^2} \tag{6.4}$$

where B_D and B_{U_∞} are the bias limits of the drag force D and the freestream velocity U_∞ respectively. P_D and P_{U_∞} are the precision limits of D and U_∞ respectively. The error limits of ρ and d are neglected in the equations because they are considered to be relatively small compared to the errors in the force and velocity measurement.

The overall uncertainty of the measured variable is determined by using equation (6.5) to combine the bias error limit and precision limit.

$$R = \sqrt{(B)^2 + (P)^2} \tag{6.5}$$

Therefore, the uncertainties estimated for the drag force and the drag force coefficient at 95 % confidence level are shown in Table 6.2 and Table 6.3.

Instrument	Bias limit (B_U) % of the measured velocity
Pitot probe no. 1	- 4%
Pitot probe no. 2	- 1%
Pitot probe no. 3	- 4%
Pitot probe no. 4	- 4%
Pitot probe no. 5	- 4%

Table 6.3: The bias limit of pitot probes

Experimental test		Averaged drag force D	Uncertainty (R_D)
Experiment in the moving water channel	Disk with 14% porosity	14.111 N	0.549 N 3.9% of D
	Disk with 50% porosity	10.199 N	0.783 N 7.7% of D
Experiment in the towing tank with zero freestream turbulence	Disk with 14% porosity	12.558 N	0.254 N 2% of D
	Disk with 50% porosity	8.550 N	0.123 N 1.4% of D
Experiment in the towing tank with nonzero freestream turbulence	Disk with 14% porosity	17.464 N	0.391 N 2.2% of D
	Disk with 50% porosity	11.408 N	0.204 N 1.8% of D

Table 6.4: Uncertainties for the drag force D

Experimental test		Drag force coefficient C_D	Uncertainty (R_{C_D})
Experiment in the moving water channel	Disk with 14% porosity	0.997	0.139 14% of C_D
	Disk with 50% porosity	0.721	0.111 15.4% of C_D
Experiment in the towing tank with zero freestream turbulence	Disk with 14% porosity	1.000	0.190 19% of C_D
	Disk with 50% porosity	0.700	0.133 19% of C_D
Experiment in the towing tank with nonzero freestream turbulence	Disk with 14% porosity	1.114	0.089 8% of C_D
	Disk with 50% porosity	0.728	0.057 7.8% of C_D

Table 6.5: Uncertainties for the drag force coefficient C_D

Chapter 7

CONCLUSIONS AND FUTURE WORK

Overview

In this chapter, the principal conclusions of this study are drawn in section 7.1 and some suggestions for further work in this area are presented in section 7.2.

7.1 Principal Conclusions

The principal conclusions of this thesis are stated below.

1. A laboratory-scale CFD model has been established to provide an important insight into the influence of energy extraction from tidal currents on the underlying hydraulic nature of flow field in an open channel. In the model described in Chapter 2, the tidal current turbine was simulated by the porous medium model based on actuator disc theory for wind turbines and the free water surface was allowed to evolve freely, instead of being defined as a 'solid' boundary.

2. Massive energy extraction can cause a free surface drop immediately downstream of the tidal current turbine. 2D and 3D CFD simulations of this head drop have been completed. In the numerical model presented in Chapter 2, porous medium model in FLUENT was used to simulate the energy extraction from moving water and the large inertial resistance coefficient of porous medium was intentionally defined as 2667 1 m^{-1} in order to consider the effects of a tidal farm. Incoming flow speed was 1.27 m s^{-1} and a low turbulence intensity of 1% was applied in the proposed numerical model. Numerical results obtained suggest that the change of free surface needs to be considered in numerical models developed for energy extraction from tidal currents, in particular for the prediction of the effect of a tidal farm, in which large extractions can cause severe free surface deformation.
3. Unlike wind turbines, tidal current turbines operate in a confined space between sea surface and seabed. As a consequence, the blockage effect is a crucial factor to be considered for the development of a large-scale tidal farm, since the blockage effect can drastically alter the flow within the channel. As the numerical results demonstrated in Chapter 2, the incoming flow velocity can be reduced and thus the power production is decreased due to the blockage effect. Meanwhile, flow around the extraction device, as well as along the downstream wake, can be appreciably accelerated.
4. A wake region is formed downstream of the tidal turbine, in which the flow velocity is considerably reduced due to the energy loss. However, the decay of wake velocity defect is a function of distance behind the turbine. This

conclusion has been clearly shown in both numerical and experimental results presented in Chapter 2, Chapter 3, Chapter 4, Chapter 5 and Chapter 6.

5. Free stream turbulence has a marked effect on the wake recovery. That the recovery of the wake is accelerated as the ambient turbulence level increases has been confirmed in the numerical sensitivity study of free stream turbulence in Chapter 3, as well as in experimental investigations of near wake at $3\,d$ and $4\,d$ downstream of a simulated tidal current turbine in Chapter 5. The trend would be more apparent if more positions could be measured in the experiment.
6. Energy extraction from tidal currents is shown to be very sensitive to the freestream flow velocity. The evidence, which was presented in the numerical sensitivity study of incoming flow velocity in Chapter 3 and the experimental measurements of near wake behind a simulated tidal current turbine in Chapter 5, shows that faster flow leads to much more of energy extracted by the turbine rotor and at the same time produces greater force on the turbine. Hence, the wake recovery distance becomes longer. This conclusion was validated only in the near wake region in the present work as the experimental measurement was not conducted beyond 4 diameters downstream of the test disk.
7. As far as the author is aware, it was the first time that the velocity profile in the tidal turbine wake was investigated experimentally in both still and moving water, using simulated tidal current turbines. Experimental results in Chapter 4 and Chapter 5 showed that the wake profile exhibited a symmetric, Gaussian-like shape in the horizontal plane. The non-symmetric velocity

profile in the vertical plane is considered to be caused by the presence of strut but is most likely to be magnified by the shear in the incident open channel flow, as shown in Chapter 4.

8. The similarity between the wake of a wind turbine and a tidal turbine has been observed in the experimental results and verified that it is an acceptable approach to getting a basic understanding of the wake development for tidal current turbines by referring to the knowledge of wind turbine wakes. Nonetheless, relying totally on theoretical methods appropriate for wind turbines would cause fundamental errors because their operating environments are substantially different. A tidal turbine wake is a more complicated three dimensional problem because the existence of a free surface and seabed will restrict and interact with the wake. In addition, the distortion of the free water surface will distort the tidal turbine wake and may further influence the performance of a tidal turbine.
9. That both towing tanks and open channels can be used for a laboratory scale experimental investigation of a model tidal current turbine, has been confirmed in this study, through comparison of wake profiles obtained under different test conditions, which were described and discussed in Chapter 4, Chapter 5 and Chapter 6. A towing tank is recommended by the author because it provides an ideal testing environment where the accurate measurement results and thus the comprehensive analysis can be achieved by controlling the important experimental parameters. In addition, testing of the tidal current device at different scales can be realized in a towing tank. However, the incoming shear flow needs to be simulated in a towing tank in

order to identify its influence on the energy production as well as the wake development, which is important for a tidal current turbine to be installed in a relatively shallow channel, where a large velocity difference can be created between the bottom of turbine and the top due to the seabed boundary layer.

10. Qualitative validation, by comparison between the numerical model predictions and measured experimental data for the near wake region behind a simulated tidal current turbine in Chapter 6, confirms that the present model can be used to provide valuable information on the downstream wake from a tidal current turbine, and also shows the need for further improvement of the predictive capacity of numerical models.
11. This study has further proved that tidal current energy extraction has substantial impacts on the local flow fields. Therefore, the available energy from a tidal current is environmentally constrained. For a given channel, the estimation of maximum extractable energy needs to take into account of its effect on the local environment, which should be studied through both numerical and experimental methods, according to the real characteristics of that channel.

7.2 Further Work

The performance of the numerical model proposed for the simulation of energy extraction from tidal currents can be further enhanced. Since the tidal current turbine is simplified to a semi-permeable disk in the current study, the numerical model would be more promising for the prediction of far wake development. That is the flow field beyond five rotor diameters downstream of the tidal current turbine, where

the flow details particularly linked to the properties of turbine blades can be negligible and thus modelling the actual rotor is not imperative. Different turbulence models may be tested in the numerical model and compared against the experimental data in order to improve the accuracy of the model predictions of the mean flow and also turbulence in the wake. That the flow is accelerated around the turbine due to the blockage effect could increase the energy to be captured by the downstream turbines in a tidal farm, if the turbines are conventionally arranged in parallel rows with appropriate spacing. The optimal spacing between turbines could be examined and investigated by defining multiple disks in the present numerical model.

The influence of the strut behind the test disk on the experimental results is evident. In subsequent experiments, the support strut could be streamlined in order to minimize its disturbance to the main flow. The perforated disk is a simple simulator but can be used very effectively to study the far-wake features of a tidal current turbine. Experimental measurements were only able to be conducted in the near wake region in this study. However, the far wake region is more important in evaluating a tidal farm's power generation. Therefore, detailed measurements of velocity and turbulence in the far wake region behind the perforated disk, using more sophisticated experimental equipment, are needed to be implemented and are also critical to provide an accurate comparison with the numerical predictions. A group of perforated disks could be tested to simulate a tidal farm in order to identify the optimum turbine numbers as well as the spacing between turbines in a farm. An actual tidal turbine model needs be experimentally investigated, which would give a valuable insight into the interaction between the flow and the turbine rotor and thus improve better understanding of physical behaviour of both near and far wake. In

addition, the effects of freesurface drop, the ambient turbulence and the water depth on the performance of tidal turbine as well as the wake development can be further quantified and should be studied further.

Appendix A

Second-order Upwind Scheme

This description of second-order upwind scheme that is employed in the commercial CFD software: FLUENT, is taken from FLUENT User's Guide 6.2.

When the second-order upwind scheme is applied, quantities at cell faces are computed using a multidimensional linear reconstruction approach. In this approach, higher-order accuracy is achieved at cell faces through a Taylor series expansion of the cell-centered solution about the cell centroid. Thus when second-order upwinding is selected, the face value ϕ_f is computed using the expression in equation (A.1):

$$\phi_f = \phi + \nabla\phi \cdot \Delta\vec{s} \tag{A.1}$$

where ϕ and $\nabla\phi$ are the cell-centered value and its gradient in the upstream cell, and $\Delta\vec{s}$ is the displacement vector from the upstream cell centroid to the face centroid. This formulation requires the determination of the gradient $\nabla\phi$ in each cell. This gradient is computed using the divergence theorem, which in discrete form is written as equation (A.2)

$$\nabla\phi = \frac{1}{V}\sum_{f}^{N_{faces}} \tilde{\phi}_f \vec{A} \tag{A.2}$$

where V is the cell volume, N_{faces} is the number of faces enclosing cell, $\vec{A}$ is surface area vector and $\tilde{\phi}_f$ is the face values computed by averaging ϕ from the two cells adjacent to the face. Finally the gradient $\nabla\phi$ is limited so that no new maxima or minima are introduced.

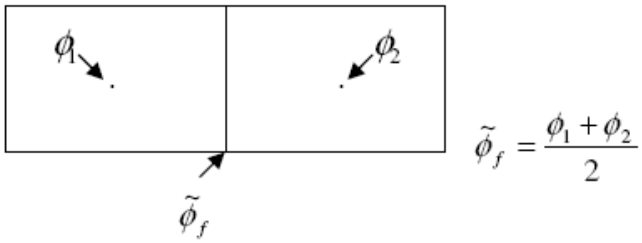

Figure A.1: Example of the computation of the face value $\tilde{\phi}_f$ in the second-order interpolation scheme

Appendix B

Pressure Outlet Condition

Users-Defined functions (UDF) are written in the C programming language. It can enhance the standard features of FLUENT in many ways. For instance, it can be used to customize the boundary condition to a specific problem.

In this study, the UDF function was used to define the pressure outlet boundary condition for the numerical simulation of energy extraction from moving water and the program used in the present models is given below.

```
#include "udf.h"
DEFINE_PROFILE(outlet_pressure,thread,nv)
{
 face_t  f;
 real x[ND_ND];
 Thread *t0=THREAD_T0(thread);
 begin_f_loop(f, thread);
 {
  cell_t c0=F_C0(f, thread);
  F_CENTROID(x, f, thread);
  F_PROFILE(f, thread, nv)=-(C_R(c0,t0)-1.225)*9.81*x[2];
 }
 end_f_loop(f, thread)
}
```

Appendix C

Porous Media Model in FLUENT

Porous media model used in the FLUENT is described in this Appendix.

Porous medial model can be employed for dealing with the problems such as flows through packed beds, filter papers, perforated plates, flow distributors and tube banks. A cell zone needs to be defined beforehand in which the porous media model is applied. The pressure loss in the flow is determined via the user's input parameters for the porous media. In essence, the porous media model is nothing more than an added momentum sink in the governing momentum equations.

Porous media is modelled by the addition of a momentum source term: equation (C.1) to the standard fluid flow equations. Basically, the source term includes two parts: a viscous loss term (the first term on the right-hand side of equation (C.1)) and an inertial loss term (the second term on the right-hand side of equation (C.1)).

$$S_i = -\left(\sum_{j=1}^{3} D_{ij} u_j \mu + \sum_{j=1}^{3} C_{ij} \frac{1}{2} \rho |u_j| u_j \right) \tag{C.1}$$

where S_i is the source term for the i th (x , y , or z) momentum equation, and D and C are prescribed matrices. ρ and μ are the density and dynamic viscosity of the fluid respectively. u_j are velocity components in the x , y and z directions. This

momentum sink contributes to the pressure gradient in the porous cell, creating a pressure drop that is proportional to the fluid velocity (or velocity square) in the cell. For a simple homogeneous porous media, the equation (C.1) can be rewritten as equation (C.2) below.

$$S_i = -\left(\frac{\mu}{\alpha} u_j + C_2 \frac{1}{2} \rho |u_j| u_j \right) \tag{C.2}$$

where α is the permeability and C_2 is the inertial resistance factor, simply specified D and C as diagonal matrices with $\frac{1}{\alpha}$ and C_2, respectively, on the diagonals (and zero for the other elements).

At high flow velocities, the constant C_2 in equation (C.1) provides a correction for inertial losses in the porous media. This constant can be viewed as a loss coefficient per unit length along the flow direction, thereby allowing the pressure drop to be specified as a function of dynamic head.

If a perforated plate or tube bank is simulated, the permeability tem in equation (C.1) can be eliminated and the inertial loss term is used alone. Thus, the equation (C.1) can be simplified as equation (C.3).

$$\nabla p = -\sum_{j=1}^{3} C_{2ij} \left(\frac{1}{2} \rho |u_j| u_j \right) \tag{C.3}$$

When the porous media model is utilized, the input parameters required in FLUENT are the viscous resistance coefficients $\frac{1}{\alpha_{ij}}$ and the inertial resistance coefficients C_{2ij} as well as the direction vectors for which they apply.

Appendix D

Calibration of the Pitot Probe

To obtain a functional form for a differential pressure versus voltage plot for data collected from the pressure transducer, a calibration was conducted for the finished pitot probes individually according to the measurement principle of the pitot probe. The calibration procedures were briefly introduced as follows.

The tip of the pitot probe was press fitted into an approximately 400 mm transparent plastic tube at one end and the joint portion between them was kept watertight. The other end of tube was opened to the atmosphere. The main body tube remained in a straight line with the pitot probe. A 1000 mm ruler was held accurately against tube and the 'zero' of the ruler was set in the middle of the length of the pressure transducer where the sensing area of transducer was located. The entire system was placed perpendicular to the ground. The power leads of the transducer were connected to a 10 V DC power supply and the transducer output lead were connected to the datascan. The data can be read from the computer screen.

At the start of calibration, the stagnation and static ports of the pitot probe were all opened to the atmosphere and the reading from the transducer was recorded as its offset. Then, a small amount of water was poured slowly into the tube until it reached a certain definite level. The height of the column of water (pressure) in centimetres

inside the tube was measured by the ruler and was recorded. The corresponding voltage output from pressure transducer was also recorded. Afterwards, a bit more water was added in the tube in order to take another reading of the height of the water column as well as the voltage output. In total, six pairs of readings were collected during the calibration process. The calibration setup is illustrated in Figure D.1. Same process was repeated several times for each pitot probe in order to exclude errors and test the repeatability of transducer.

Since the pressure measured by the stagnation port was p_{stag} ($p_{atm} + \rho gh$) and the static pressure was p_{atm} , the differential pressure $p_{stag} - p_{atm}$ was then calculated as ρgh . The results were plotted to show the linear relationship between the differential pressure and voltage output from the transducer. The calibration was not conducted under vacuum conditions. Thus, a correction to the calibration line was done to eliminate the influence of the air that was remained in the tubings of pitot probe during the calibration process. The final calibration curve for each pitot probe used in the present experiment is shown in Figure D.2-D.6 respectively.

Figure D.1: Calibration setup for the pitot probe

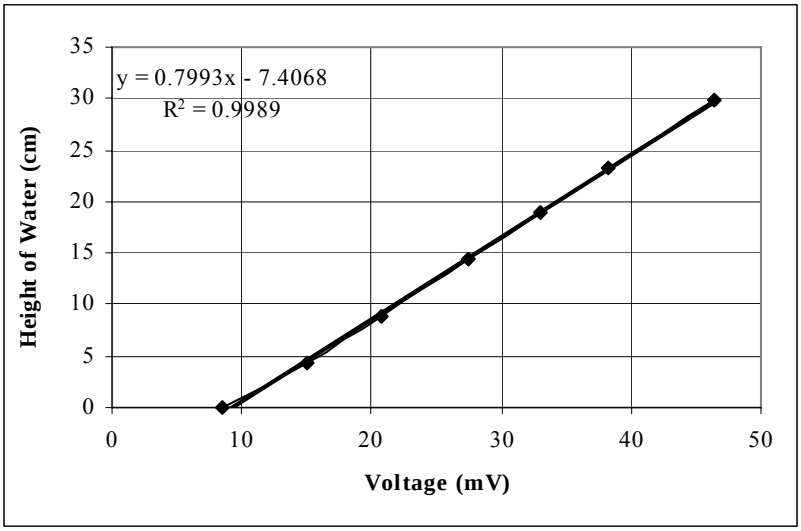

Figure D.2: Calibration line for pitot probe no. 1

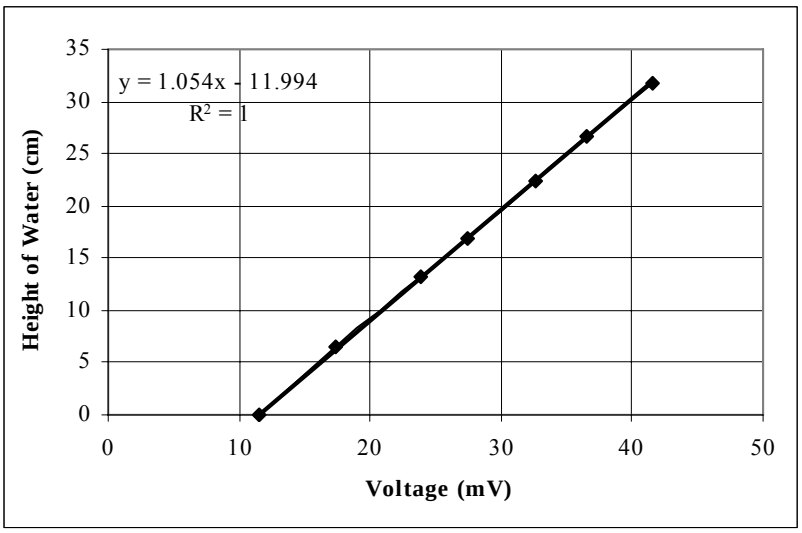

Figure D.3: Calibration line for pitot probe no. 2

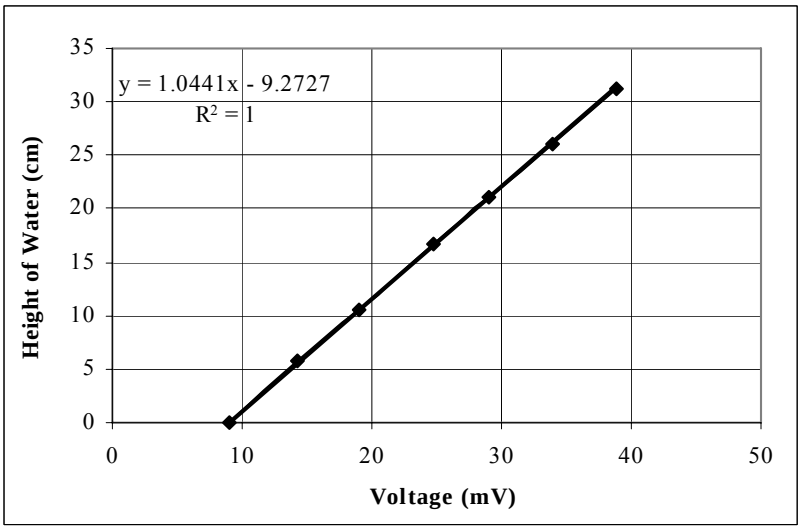

Figure D.4: Calibration line for pitot probe no. 3

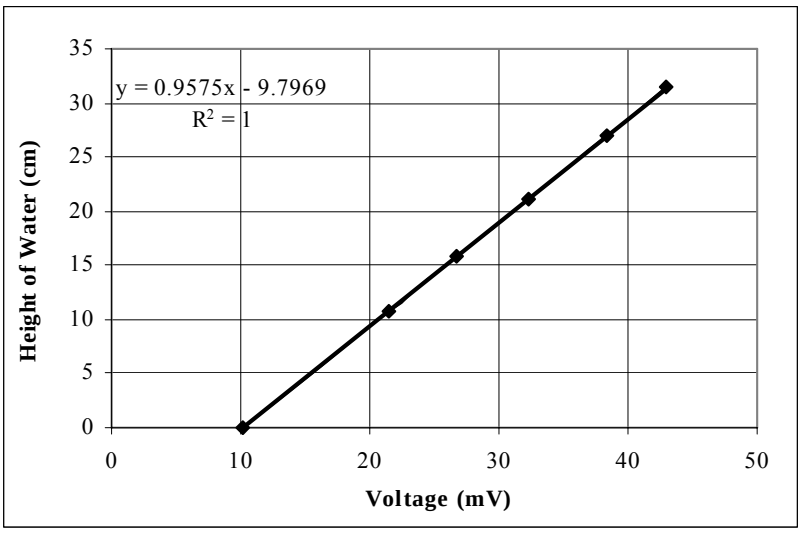

Figure D.5: Calibration line for pitot probe no. 4

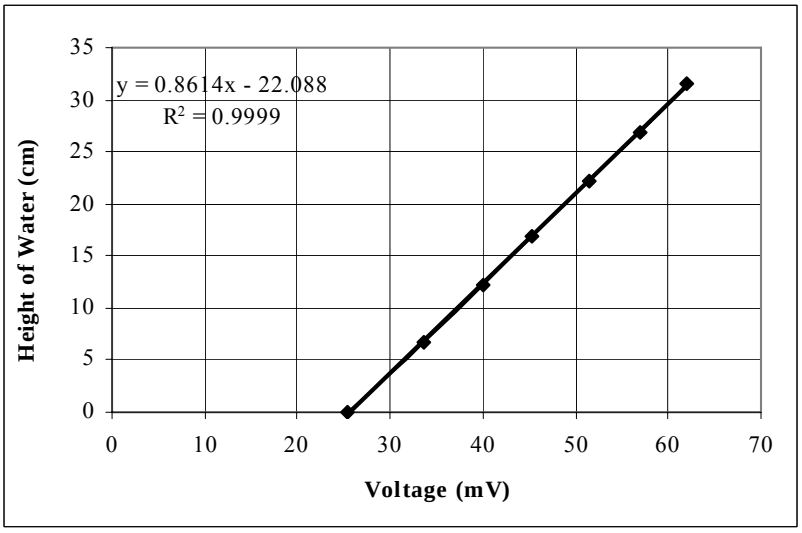

Figure D.6: Calibration line for pitot probe no. 5

Appendix E

A Summary of the Experimental Runs

I.

Experiments conducted in the water flow channel	
Measurement	Total number of experimental runs
Perforated disk with 0% porosity	6
Perforated disk with 14% porosity	6
Perforated disk with 50% porosity	6

Table E.1: Total experimental runs in the water flow channel test

II.

Experiments conducted in the towing tank	
Without the turbulence generating grid upstream from the test disk	
(a) Towing speed U_∞ =0.76 m s^{-1}	
Measurement	Total number of experimental runs
Perforated disk with 14% porosity	4
Perforated disk with 50% porosity	4
(b) Towing speed U_∞ =1.26 m s^{-1}	
Measurement	Total number of experimental runs
Perforated disk with 14% porosity	4
Perforated disk with 50% porosity	4
With the turbulence generating grid upstream from the test disk	
Towing speed U_∞ = 1.26 m s^{-1}	
Measurement	Total number of experimental runs
Perforated disk with 14% porosity	4
Perforated disk with 50% porosity	4

Table E.2: Total experimental runs in the towing tank test

Appendix F

Published Papers during the PhD Study

Journal paper

X. Sun, J.P. Chick, I.G. Bryden, Laboratory-scale simulation of energy extraction from tidal currents. Journal of Renewable Energy, Volume 33, Issue 6, June 2008, Pages 1267-1274.
URL: www.sciencedirect.com

Conference paper

S.J. Couch, X. Sun, I.G. Bryden, Modelling of energy extraction from tidal currents. In: Proceedings of the sixth EWTEC European wave and tidal energy conference, 2005

References

[1] IPCC, "Climate Change 2001: Impacts, Adaptation, and Vulnerability," Contribution of Working Group II to the Third Assessment Report of the Intergovernmental Panel on Climate Change. Cambridge University Press, Cambridge, UK, 2001.

[2] NOAA, "Climate Impact of Quadrupling Atmospheric CO2: an Overview of GFDL Climate Model Results," Geophysical Fluid Dynamics Laboratory. National Oceanic and Atmospheric Administration of the US Department of Commerce., 2004.

[3] USA Environment Protection Agency, "Greenhouse gases and global warming, potential values April 2002," 2002.

[4] S. J. Taylor, "Sustainable development in the use of energy for electricity generation," Proc. Instn. Civil Engineering pp. 126-132, 1998.

[5] D. Elliot, "Green power and liberalisation of the UK electricity market," International journal of Ambient Energy, vol. 20, pp. 3-13, 1999.

[6] G. Boyle, "Renewable Energy: power for a sustainable future," Oxford Express, vol. Chapter 2, pp. 27-37, 1996.

[7] DTI, "Status and Research and Development Priorities: Wave and Marine Current Energy," Department of Trade & Industry, 2003.

[8] J. A. Clarke, G. Connor, A. D. Grant, and C. M. Johnstone, "Regulating the output characteristics of tidal current power stations to facilitate better base load matching over the lunar cycle," Renewable Energy, vol. 31, pp. 173-180, 2006.

[9] D. A. Ross, "Understanding Tides," Saltwater Fly Fishing, vol. 2, 1996.

[10] I. G. Bryden, "The marine energy resource, constraints and opportunities," Maritime Engineering, vol. 159, pp. 55-65, 2006.

[11] The Eling Tide Mill, available online: http://www.elingtidemill.wanadoo.co.uk/gall.html.

[12] J. P. Frau, "Tidal Energy: promising projects: La Rance, a successfuly industrial-scale experiment," IEEE Transactions on ENergy Conversion, vol. 8, pp. 552-558, 1993.

[13] The tial barrage, available online: http://www.sciencemuseum.org.uk/exhibitions/energy/site/EIZCaseStudy7Item3.asp.

[14] I. Ball, "Turning the tide: Power from the sea and protection for nature." World wide fund for nature report, Cardiff University, 2002.

[15] P. L. Fraenkel, "Marine Current Turbines: an emerging technology," Paper for Scottish Hydraulic Study Group Seminar in Glasgow: Renewable Energy-Hydraulic Applications-Theory and Practice, 2004.

[16] P. L. Fraenkel, "Power from marine currents," Proceedings of the Institution of Mechanical Engineers, Part A: Journal of Power and Energy, vol. 216, pp. 1-14, 2002.

[17] I. G. Bryden, S. Naik, P. Fraenkel, and C. R. Bullen, "Matching tidal current plants to local flow conditions," Energy (Oxford), vol. 23, pp. 699-709, 1998.

[18] E. Tecnomare, IT Power, Ponte Di Archimede. University of Patras, "Marine currents energy extraction: resource assessment," Final Report, EU-JOULE contract JOU2-CT93-0355, 1995.

[19] ETSU, "Tidal stream energy review," UK DTI. Prepared by Engineering & Power Development Consultants Ltd, Binnie & Parterners, Sir Robt. McAlpine & Sons Ltd and IT Power Ltd, for the ETSU, UK Department of Energy. Report no. ETSUT/05/00155/REP, Crown Copyright 1993., 1993.

[20] Black & Veatch, "Europe and Global Tidal Stream Energy Resource Assessment," Report to Carbon Trust 2004.

[21] ICIT, "Feasibility study of tidal current power generation for coastal waters: Orkney Shetland " Final Report, EU Contract XVII/4: 1040/92-1040/41 1995.

[22] I. G. Bryden, B. C., B. M., and P. O., "Generating electricity from tidal currents in Orkney and Shetland," Underwater Technology, vol. 21, 1995.

[23] Promising tide sites in the UK, available online: www.scottishrenewables.com/data/reports/0612_MarineBriefing.doc.

[24] J. Thake, "DTI Renewables: development, installation and testing of a large scale tidal current turbine," 2005.

[25] The Kobold turbine, available online: http://www.dpa.unina.it/adag/eng/renewable_energy.html.

[26] K. F. Mason, "Composite Tidal Turbine to Harness Ocean Energy," Composites Technology, 2005.

[27] DTI, "Variable Pitch Foill Vertical Axis Tidal Turbine," Department of Trade & Industry, 2006.

[28] A. Fiorentino, "Tidal Stream Plant at the Straits of Messina," Ponte di Archimede SpA, Italy, 1998.

[29] DTI, "The Engineering Business: Research and Development of a 150kw Tidal Stream Generator-Phase 1," ETSU T/06/00211/REP; URN No. 02/1400, 2002.

[30] DTI, "The Engineering Business: Research and Development of a 150kw Tidal Stream Generator-Phase 2," ETSU T/06/00211/REP; URN No. 02/1400, 2003.

[31] DTI, "The Engineering Business: Stingray Tidal Stream Energy Device-Phase 3," ETSU T/06/00230/00/00; URN No. 05/864, 2005.

[32] Hydroventuri Ltd., available online: http://www.hydroventuri.com/page.php?7.

[33] H. A. Mackay, "GENTEC Venturi," Enterprise and Culture Committee-Renewable Energy in Scotland Inquiry, 2004.

[34] P. L. Fraenkel, "Tidal current energy technologies," Ibis, vol. 148, pp. 145-151(7), 2006.

[35] E. Joule, "Marine Current Energy Extraction - Final Report," JOU2-CT93-0355, 1995.

[36] DTI, "The Commercial Prospects for Tidal Power," ETSU report T/06/00209/REP, URN No. 01/1011, 2001.

[37] Marine current Ltd., available online: http://www.marineturbines.com/projects.htm.

[38] A. S. Bahaj and L. E. Myers, "Fundamentals applicable to the utilisation of marine current turbines for energy production," Renewable Energy, vol. 28, pp. 2205-2211, 2003.

[39] I. G. Bryden, S. J. Couch, A. Owen, and G. Melville, "Tidal current resource assessment," Proceeding of the I MECH E Part A Journal of Power and Energy, vol. 221, pp. 125-135, 2007.

[40] G. Sutherland, M. Foreman, and C. Garrett, "Tidal current energy assessment for Jonstone Strait, Vancouver Island," Proceeding of the I MECH E Part A Journal of Power and Energy, vol. 1221, pp. 147-157, 2007.

[41] S. J. Couch and I. G. Bryden, "Tidal current energy extraction: hydrodynamic resource characteristics," Proceeding of the I MECH E Part M Engineering for the Maritime Environment, vol. 220, 2006.

[42] P. R. Cave and E. M. Evans, "Tidal streams and energy supply in the Channel Islands," in Energy for Rural and Island Communities IV, in Proceedings of the Fourth International Conference, Inverness, UK, 1985, pp. 159-164.

[43] P. R. Cave, E. M. Evans, and K. J. George, "Assessment of tidal stream as an energy resource," in Fifth International Conference on Energy Options- the role of alternatives in the world energy scene, University of Reading, UK, 1987, pp. 153-156.

[44] G. I. Gretton and T. Bruce, "Aspects of matematical modeling of a prototype scale vertical-axis turbine," in Proceedings of the 7th European Wave and Tidal Energy Conference Porto, Portugal, 2007.

[45] W. M. J. Batten, A. S. Bahaj, A. F. Molland, and J. R. Chaplin, "The prediction of the hydrodynamic performance of marine current turbines," Renewable Energy, vol. 33, pp. 1085-1096, 2008.

[46] J. A. Clarke, G. Connor, A. D. Grant, and C. M. Johnstone, "Design and testing of a contra-rotating tidal current turbine," Proceedings of the I MECH E Part A Journal of Power and Energy, vol. 221, pp. 171-179, 2007.

[47] R. F. Nicholls-Lee and S. R. Turnock, "The use of computational fluid dynamics in the optimization of marine current turbines," in 10th Numerical Towing Tank Symposium (NuTTS'07), Hamburg, Germany, 2007, p. 6.

[48] I. G. Bryden and S. J. Couch, "ME1-Marine energy extraction: Tidal resource analysis," Renewable Energy, vol. 31, pp. 133-139, 2006.

[49] I. G. Bryden, T. Grinsted, and G. T. Melville, "Assessing the potential of a simple tidal channel to deliver useful energy," Applied Ocean Research, vol. 26, pp. 200-206, 2005.

[50] S. J. Couch, X. Sun, and I. G. Bryden, "Modelling of energy extraction from tidal currents," in 6th EWTEC European Wave and Tidal Energy Conference Glasgow, UK, 2005.

[51] W. M. J. Batten, A. S. Bahaj, A. F. Molland, and J. R. Chaplin, "Experimentally validated numerical method for the hydrodynamic design of horizontal axis tidal turbines," Oceaning Engineering, vol. 34, pp. 1013-1020, 2007.

[52] A. S. Bahaj, A. F. Molland, J. R. Chaplin, and W. M. J. Batten, "Power and thrust coefficients of marine current turbines operating under various hydrodynamic conditions of flow in cavitation tunnels and towing tanks," Renewable Energy, vol. 32, pp. 407-426, 2007.

[53] L. E. Myers and A. S. Bahaj, "Power Output Performance Chararcteristics of a Horizontal Axis Marine Current Turbine," Renewable Energy, vol. 31, pp. 197-208, 2006.

[54] V. R. Klaptocz, G. W. Rawlings, Y. Nabavi, M. Alidadi, Y. Li, and S. M. Calisal, "Numerical and experimental investigation of a ducted vertical axis tidal current turbine," in present at the 7th European Wave and Tidal Energy Conference Porto, Portugal, 2007.

[55] G. Germain, A. s. Bahaj, C. Huxley-Reynard, and P. Roberts, "Facilities for marine current energy converter characterization," in present at the 7th European Wave adn Tidal Energy Conference Porto, Portugal, 2007.

[56] A. S. Bahaj, L. E. Myers, M. D. Thomson, and N. Jorge, "Characterising the wake of horizontal axis marine current turbiens," in presented at Proceedings of the 7th European Wave and Tidal Energy Conference Porto, Portugal, 2007.

[57] J. D. Anderson, Computational Fluid Dynamics: the basics with applications, McGraw-Hill, Inc. New York, 1995.

[58] H. K. Versteeg and W. Malalasekera, An Introduction to Computational Fluid Dynamics: The Finite Volume Method Approach, Prentice Hall, 1996.

[59] X. Tao and F. Stern, "Numerical methods in computational fluid dynamics (CFD)," 2006.

[60] A. Saxena and B. Sahay, Computer Aided Engineering Design, Kluwer Academic Publishers, 2005.

[61] M. W. Frank, Fluid Mechanics, 5th ed., Higher Education, 2002.

[62] Y. Nakayama and R. Boucher, Introduction to Fluid Mechanics, Butterworth-Heinemann, 1998.

[63] Laminar and turbulent flow, available online: http://history.nasa.gov/SP-367/chapt3.htm."

[64] J. O. Hinze, Turbulence: An Introduction to its Mechanism and Theory, McGraw Hill: New York, 1959.

[65] R. J. Garde, Turbulent Flow, John Willey and Sons: New York, 1994.

[66] Turbulent flow in a pipe, available online: http://www.flometrics.com/services/hydbub/.

[67] Turbulent jet, available online: http://www.ltu.se/polopoly_fs/1.4033!27cb4722.jpg.

[68] Velocity at a point in a turbulent flow, available online: http://www.princeton.edu/~asmits/Bicycle_web/transition.html.

[69] L. Prandtl, "Report on investigation into development turbulence," Zeitschrift angewandten Math Mech., vol. 5, pp. 136-139, 1925.

[70] W. Rodi, "Turbulence models and their application in hydraulics-A state of the Art Review," IAHR, Delft, 1984.

[71] D. C. Wilcox, "Turbulence Modelling for CFD," DCW Industries, Inc., La Canada, California, 1998.

[72] S. K. Aliabadi, A. J., and B. Zellars, "Parallel finite element simulation of mooring forces on floating objects," International Journal for Numerical Methods in Fluids, vol. 41, pp. 809-822, 2003.

[73] W. Yue, C. Lin, and V. C. Patel, "Numerical simulation of unsteady multidimensional free surface motions by level set method," International Journal for Numerical Methods in Fluids, vol. 42, pp. 853-884, 2003.

[74] Unverdi SO and T. G., "A front-tracking method for viscous, incompressible, multi-fluid flows," Journal of Computational Physics, vol. 100, pp. 25-37, 1992.

[75] F. H. Harlow and W. J.E., "Numerical study of large-amplitude free surface motion," Physics of Fluids, vol. 8, pp. 2182-2189, 1965.

[76] C. W. Hirt and B. D. Nichols, "Volume of fluid (VOF) method for the dynamics of free boundaries," Journal of Computational Physics, vol. 39, pp. 201-225, 1981.

[77] F. J. Kelecy and P. R.H., "The development of a free surface capturing approach for multidimensional free surface flows in closed containers," Journal of Computational Physics, vol. 138, pp. 939-980, 1997.

[78] J. M. Floryan and H. Rasmussen, "Numerical Methods for Viscous Flow with Moving Boundaries," Applied Mechanics Review, vol. 42, pp. 323-341, 1989.

[79] Fluent, Fluent 6.2 User's Guide Fluent Inc., NH: USA, 2005.

[80] R. E. Froude, "On the part played in propulsion by difference in pressure," Transaction of the Institute of Naval Architects, vol. 30, pp. 390-423, 1889.

[81] T. Burton, D. Sharpe, N. Jenkins, and E. Bossanyi, Wind Energy Handbook, John Wiley and Sons, 2001.

[82] D. J. Sharpe, "A general momentum theory applied to an energy-extracting actuator disc," Wind Energy, vol. 7, pp. 177-188, 2004

[83] R. Mikkelsen, "Actuator Disc Methods Applied to Wind Turbines," in Department of Mechanical Engineering. Thesis (Ph.D.), the Technical University of Denmark 2003, p. 121.

[84] L. J. Vermeer, J. N. Sorensen, and A. Crespo, "Wind turbine wake aerodynamics," Progress in Aerospace Science, vol. 39, pp. 467-510, 2003.

[85] H. Glauert, "Airplane propellers," In: Durand WF, editor. Aerodynamic Theory. Dover, New York, pp. 169-269, 1963.

[86] D. Medici, "Experimental studies of wind turbine wakes-power optimisation and meandering," in KTH Mechanics, Sweden, 2005.

[87] M. Vysohlid and K. Mahesh, "Understanding crashback in marine propeller using an unsteady actuator disk model," in 45th AIAA Aerospace Sciences Meeting and Exhibit, Reno, Nevada, 2007.

[88] A. J. MacLeod, S. Barnes, K. G. Rados, and I. G. Bryden, "Wake effects in tidal current turbine farms," in International Conference on Marine Renewable Energy-Conference Proceedings, 2002, pp. 49-53.

[89] J. H. Ferziger and M. Peric, Computational Methods for Fluid Dynamics, Springer, 1996.

[90] S. V. Patankar, Numerical Heat Transfer and Fluid Flow, Hemisphere, Washington, D.C., 1980.

[91] European Commission, "The exploitation of tidal marine currents," Report EUR16683EN, 1996.

[92] L. E. Myers and A. S. Bahaj, "Wake Studies of a 1/30th scale Horizontal Axis Marine Current Turbine," Ocean Engineering, vol. 34, pp. 758-762, 2007.

[93] L. E. Myers and A. S. Bahaj, "Flow effects in marine current turbine arrays," in Proceedings World Renewable Energy Congress (WREC-IX), Florence, 2006.

[94] D. L. Elliot, "Status of wake and array loss research," in Proceedings of the Wind Power Conference, 1991, pp. 244-261.

[95] P. M. Sforza, P. Sheerin, and M. Smorto, "Three-dimensional wakes of simulated wind turbines," AIAA Journal, vol. 19, pp. 1101-1107, 1981.

[96] K. G. Rados, "Optimisation of tidal farms", Individual Grant Review Report-GR/N04805/01, 2003.

[97] P. E. J. Vermeulen, "An experimental analysis of wind turbine wakes," In: Proceedings of the 3rd International Symposium on Wind Energy Systems. BHRA Fluid Engineering, Lyngby, Denmark, pp. 431-450, 1980.

[98] M. B. Anderson, D. J. Milborrow, and J. N. Ross, "Performance and wake measurements on a 3m diameter HAWT: comparison of theory, wind tunnel and field test data," ETSU contract E/5A/CON/1090/177/020 Cavendish, 1982.

[99] D. Medici and P. H. Alfredsson, "Measurements on a wind turbine wake: 3D effects and bluff body vortex shedding," Wind Energy, vol. 9, pp. 219-236, 2006.

[100] C. Sicot, P. Devinant, T. Laverne, S. Loyer, and J. Hureau, "Experimental study of the effect of turbulence on horizontal axis wind turbine aerodynamics," Wind Energy, vol. 9, pp. 361-370, 2006.

[101] P. H. Alfredsson, J. A. Dahlberg, and F. H. Bark, "Some properties of the wake behind horizontal axis wind turbines," Precision Engineering, pp. 469-484, 1980.

[102] R. W. Baker, S. N. Walker, and P. C. Katen, "Wake measurements around operating wind turbines," Journal of Solar Energy Engineering, vol. 107, pp. 183-185, 1985.

[103] Takao Maeda, Takeshi Yokota, Yukimaru Shimizu, and K. Adachi, "Wind tunnel study of the interaction between two horizontal axis wind turbines," Wind Engineering, vol. 28, pp. 197-212, 2004.

[104] L. M. Logory, A. Hirsa, and D. G. Anthony, "Interaction of wake turbulence with a free surface," Physics of Fluids, vol. 8, pp. 805-815, 1996.

[105] PaikBuGeun, LeeChoungMook, and LeeSangJoon, "Comparative measurements on the flow structure of a marine propeller wake between an open free surface and closed surface flows," Journal of Marine Science and Technology, vol. 10, pp. 123-130, 2005.

[106] D. Medici and P. H. Alfredsson, "Wind turbine near wakes and comparisons to the wake behind a disc," 43rd AIAA Aerospace Sciences Meeting and Exhibit-Meeting Papers, pp. 15593-15604, 2005.

[107] P. B. S. Lissaman and E. R. Bate, "Energy effectiveness of arrays of wind energy conversion systems", Aero Vironment Report No. AV FR 7058, 1977.

[108] W. Wentz, C. Ostowari, D. Manor, and M. Snyder, "Horizontal axis wind turbine wake and blade flow studies from model tests," ASME, pp. 235-244, 1985.

[109] P. B. S. Lissaman, "Energy effectiveness of arbitary arrays of wind turbines," AIAA paper, 17th Aerospace Sciences Meeting, 1979.

[110] P. J. H. Builtjes, "Interaction of windmill wakes," IERE Conference Proceedings, pp. B5.49-B5.58, 1978.

[111] U. Hassan, "A wind tunnel investigation of the wake structure within small wind farms," ETSU WN 5113, 1992.

[112] P.M.Sforza, W. Stasi, M.Smorto, and P.Sheerin, "Wind turbine generator wakes," 17th AIAA Aerospace Science Meeting, pp. 70-0113, 1979.

[113] P. E. J. Vermeulen and P. J. H. Builtjes, "Turbulence measurements in simulated wind turbine clusters," Report 82-03003, TNO Division of Technology for Society, 1982.

[114] W. Gracey, "Measurement of aircraft speed and altitude," NASA PR-1046, 1980.

[115] Laboratory Manual for EAS 361 Engineering Fluid Mechanics
available online: www.cee.pdx.edu/eas361/LabManual.pdf

[116] M. P. Miller, T. A. Nennstiel, J. H. Duncan, A. A. Dimas, and S. Proestler, "Incipent breaking of steady waves in the presence of surface wakes," Journal of Fluid Mechanics, vol. 383, pp. 285-305, 1999.

[117] C. C. Gettelman and L. N. Krause, "Considerations entering into the selection of probes for pressure measurement in jet engines," Proceedings of the Instrument Society of America, vol. 17, pp. 134-137, 1952.

[118] H. Schlichting, Boundary-layer theory: 7th ed. McGraw-Hill, New York, 1979.

[119] J. Whale, "A study of the near wake of a model wind turbine using particle image velocimetry ". Thesis (Ph.D.), University of Edinburgh, 1996.

[120] R. N. Meroney and R. T. Yang, "Wind tunnel study on gaseous mixing due to various stack heights and injection rates above an isolated structure," A report of the Fluid Dynamics and Diffusion Laboratory, Colorado State University, Fort Collins, Colo, 1971.

[121] America-Wind-Energy-Association, "Standard Performance Testing of Wind Energy Conversion Systems," AWEA Standard, vol. AWEA 1.1, 1988.

[122] M. Gad-el-Hak, "Water towing tank as an experimental facility," Experiments in Fluids, vol. 5, pp. 289-297, 1987.

[123] Glasgow towing tank, available online: http://www.na-me.ac.uk/index_2.htm.

[124] E. M. Laws and J. L. Livesey, "Flow through screens," Ann. Rev. Fluid Mech., vol. 10, pp. 247-266, 1978.

[125] C. Morize and F. Moisy, "Energy decay of rotating turbulence with confinement effects," Physics of Fluids, vol. 18, p. 065107, 2006.

[126] J. O. Hinze, Turbulence, McGraw-Hill Book Co., New York, 1975.

[127] Fluent forum, available online: http://university.fluent.com/forum/.

[128] H. W. Coleman, Experimentation and uncertainty analysis for engineers, Wiley, New York, 1989.

[129] J. S. Bendat and A. G. Piersol, Random data: analysis and measurement procedures, 1971.